



Provided by the author(s) and University of Galway in accordance with publisher policies. Please cite the published version when available.

Title	A computational investigation of the laser bonding of balloon catheters
Author(s)	Ryan, Enda
Publication Date	2015-09-28
Item record	<a href="http://hdl.handle.net/10379/5310">http://hdl.handle.net/10379/5310</a>

Downloaded 2024-04-24T21:20:59Z

Some rights reserved. For more information, please see the item record link above.



# **A Computational Investigation of the Laser Bonding of Balloon Catheters**

**By**

**Enda Ryan**

A thesis submitted to the National University of Ireland as fulfilment  
of the requirements for the Degree of Doctor of Philosophy



Department of Mechanical and Biomedical Engineering

National University of Ireland, Galway

November 2014

Supervisors of Research: Dr. Mark Bruzzi and Dr. Nathan Quinlan

Industrial Partner: Boston Scientific

## Abstract

The balloon catheters produced by Boston Scientific are manufactured using a laser bonding process. The behaviour of the materials during this laser welding process is not very well understood. In this work a computational model of this process was created which will help predict the behaviour of the materials during bonding and will increase understanding of the laser bonding process.

The two parts being bonded are cylindrical and are both made of a thermoplastic polymer called PEBA<sup>X</sup>®. During the bonding process, these cylindrical parts are surrounded by a heat-shrink tubing which applies a pressure to the PEBA<sup>X</sup>® parts when heated. The heat and pressure cause the PEBA<sup>X</sup>® to melt and flow. Modelling the heat-shrink tubing and the melt flow during the laser welding process are key aims of this work.

A thermal model of the process was created by modelling the laser absorption and heat transfer through the assembly. This was compared with previous work and validated with experimental data. The PEBA<sup>X</sup>® was modelled as a viscoelastic material which transitions from relatively rigid to very compliant as it passes its melting temperature.

Extensive experimental testing was performed to characterise the heat-shrink tubing. The heat-shrink tubing was modelled using two shape memory models from the literature. These two models were implemented into Abaqus FEA using two user defined material subroutines (UMATs).

A thermo-mechanical finite element model of the bonding process was then created in Abaqus FEA and the results were compared with experimental data. This model captures the overall behaviour of the materials during the bonding process, providing predictions of melt flow. The results are compared with the experimentally observed melt flow providing new knowledge on the thermo-mechanical behaviour during the laser bonding process of balloon catheters.

## TABLE OF CONTENTS

<b>1</b>	<b>INTRODUCTION .....</b>	<b>1</b>
1.1	BACKGROUND AND MOTIVATION .....	1
1.1.1	<i>Atherosclerosis</i> .....	2
1.1.2	<i>Angioplasty</i> .....	3
1.1.3	<i>Modern balloon catheters</i> .....	3
1.2	LASER WELDING.....	4
1.3	PROXIMAL BOND .....	5
1.4	SHAPE MEMORY POLYMERS .....	7
1.5	OBJECTIVES .....	8
1.6	THESIS OVERVIEW .....	9
<b>2</b>	<b>LITERATURE REVIEW .....</b>	<b>10</b>
2.1	LASER WELDING OF POLYMERS.....	10
2.2	MODELLING OF LASER WELDING OF POLYMERS .....	11
2.3	SHAPE MEMORY POLYMERS .....	14
2.3.1	<i>Applications and interest</i> .....	15
2.3.2	<i>Materials and categorization</i> .....	16
2.3.3	<i>Characterization</i> .....	17
2.4	MODELLING OF SMPs.....	17
2.4.1	<i>Thermo-viscoelastic modelling approaches</i> .....	18
2.4.2	<i>Phase transition modelling approaches</i> .....	20
2.4.3	<i>Applications of SMP models</i> .....	23
2.5	<i>Summary and contribution</i> .....	23
<b>3</b>	<b>EXPERIMENTAL METHODS .....</b>	<b>25</b>
3.1	DYNAMIC MECHANICAL THERMAL ANALYSIS .....	26
3.2	HEAT-SHRINK TESTS PERFORMED ON DMTA.....	27
3.2.1	<i>Frequency sweep</i> .....	27
3.2.2	<i>Temperature dependence of elastic modulus</i> .....	28
3.2.3	<i>Thermal expansion coefficient <math>\alpha</math></i> .....	29
3.2.4	<i>Plasticity</i> .....	29
3.2.5	<i>Anisotropy</i> .....	29
3.2.6	<i>Frozen fraction</i> .....	29
3.2.7	<i>Recovery force tests</i> .....	30
3.2.8	<i>Stress relaxation tests</i> .....	30
3.3	DIFFERENTIAL SCANNING CALORIMETRY.....	30
3.4	MICROSCOPY .....	32
3.4.1	<i>Polarized microscopy</i> .....	32
3.4.2	<i>Optical coherence tomography</i> .....	33
3.5	SHRINK FORCE TEST .....	34
3.6	PRESSURE TEST.....	35
<b>4</b>	<b>RESULTS OF MATERIAL CHARACTERISATION .....</b>	<b>38</b>
4.1	MEASUREMENT OF ELASTIC MODULUS OF LARGE HEAT-SHRINK TUBE.....	38
4.1.1	<i>Elastic properties under dynamic loading</i> .....	38
4.1.2	<i>Effect of frequency</i> .....	39

4.1.3	Static tests .....	41
4.1.5	Axial tests .....	49
4.1.5	Anisotropy .....	49
4.2	RECOVERY FORCE.....	50
4.3	VISCOELASTIC PROPERTIES .....	52
4.3.1	Stress relaxation .....	52
4.3.2	Creep .....	53
4.4	THERMAL EXPANSION COEFFICIENT.....	54
4.5	HANGER TEST.....	55
4.6	PRESSURE TEST.....	56
4.7	DETERMINATION OF MODULUS OF SMALL HEAT-SHRINK TUBES .....	59
4.8	DETERMINATION OF THE FROZEN FRACTION .....	60
4.9	DISCUSSION.....	60
<b>5</b>	<b>THERMAL MODELLING OF THE LASER WELDING OF BALLOON CATHETERS.....</b>	<b>62</b>
5.1	LASER THERMAL ABSORPTION.....	62
5.2	HEAT TRANSFER MODEL .....	64
5.3	MODELLING OF THE STERLING™ BALLOON CATHETER JOINT ASSEMBLY.....	68
5.4	COMPARISON OF COMPUTATIONAL MODEL WITH EXPERIMENTAL DATA .....	75
5.5	DISCUSSION.....	79
<b>6</b>	<b>IMPLEMENTATION OF THERMO-MECHANICAL MODEL OF SHAPE MEMORY POLYMER .....</b>	<b>81</b>
6.1	INTRODUCTION .....	81
6.2	REVIEW OF STORED STRAIN MODEL OF LIU <i>ET AL.</i> .....	81
6.3	THE MULTIPLE NATURAL CONFIGURATIONS MODEL OF BAROT <i>ET AL.</i> .....	83
6.4	IMPLEMENTATION OF SMP MODELS.....	85
6.4.1	Implementation of stored strain model.....	85
6.4.2	Implementation of multiple natural configurations model .....	86
6.5	VERIFICATION .....	88
6.5.1	Verification of implementation of stored strain model .....	88
6.5.2	Verification of implementation of multiple natural configurations model.....	89
6.6	COMPARISON OF UMATs WITH EXPERIMENT.....	94
6.6.1	Stored strain model .....	95
6.6.2	Multiple natural configurations model.....	96
6.7	MATERIAL MODEL FOR PEBAX® .....	98
6.7.1	Prony series .....	98
6.7.2	Time-temperature superposition.....	99
6.7.3	PEBAX® data.....	101
6.8	DISCUSSION.....	106
<b>7</b>	<b>THERMO-MECHANICAL MODELLING OF BALLOON CATHETER LASER WELDING PROCESS...108</b>	
7.1	INTRODUCTION .....	108
7.2	THERMO-MECHANICAL MODEL DEVELOPMENT .....	109
7.2.1	Laser weld assembly geometry .....	109
7.2.2	Mesh.....	111
7.2.3	Boundary conditions.....	111
7.2.4	Thermomechanical loading .....	112
7.2.5	Contact .....	112
7.2.6	Materials .....	113
7.3	RESULTS.....	113

7.3.1	<i>Melt flow results</i> .....	113
7.3.2	<i>Effect of friction</i> .....	118
7.3.3	<i>Effect of initial geometry</i> .....	121
7.3.4	<i>Effect of heat-shrink modulus</i> .....	125
7.4	EXPERIMENTAL RESULTS.....	125
7.5	DISCUSSION.....	130
<b>CHAPTER 8</b>	<b>CONCLUDING REMARKS</b> .....	<b>133</b>
8.1	CONCLUSIONS.....	133
8.2	LIMITATIONS OF THIS WORK.....	135
8.3	DISCUSSION.....	136
8.4	FUTURE WORK.....	137
<b>REFERENCES</b>	.....	<b>139</b>

# 1 Introduction

The aim of the work in this thesis is to create a computational model of a laser bonding process used in the manufacture of balloon catheters. The laser bonding process is used to weld two thermoplastic polymer parts together. During the process, the laser heats the polymer parts above their melting temperature and a heat-shrink tubing, which is placed over the parts, applies a pressure which causes the polymers to flow. The heat-shrink tubing is a type of shape memory polymer (SMP) and modelling this material accurately is a major goal of this work. The model is used to predict the transient temperature distribution as well as the stresses and strains which occur during the bonding procedure. The model uses the commercial finite element analysis package Abaqus FEA.

This work:

1. Provides a better understanding of the effect of different material and experimental parameters (such as heat transfer coefficients, laser power, etc.) on the temperature distribution throughout the assembly.
2. Provides a better understanding of the effects of different material and experimental parameters (such as modulus, viscosity, maximum temperature etc.) on the deformation that occurs in the bond area.
3. Identify the most important parameters with regard to bond shape and strength.

This project will focus on one bond called the Proximal bond on one particular product (the Sterling™ catheter). However, it is envisaged that this model can be easily adapted to other bonds and other products.

## 1.1 Background and motivation

A catheter is a flexible tube that can be inserted into a body cavity or blood vessel. Catheters are regularly used to drain or administer fluids or for the delivery of surgical instruments to a specific location. In 1963 Thomas Fogarty invented a balloon catheter for removing blood clots. The deflated balloon was inserted past the clot then inflated and pulled back dragging the clot out of the body through the incision made for the catheter. Prior to this the only treatment for clots was surgery which was a very risky procedure with up to 50% of patients

dying [1]. Fogarty's catheter was the first successful example of "less invasive" surgery and quickly became the standard way to remove clots.

Less invasive, and minimally invasive, surgery are terms used to describe procedures performed using only a small incision or no incision at all. These procedures often have many benefits such as less operative trauma, less pain and a quicker recovery [2]. These methods are now being used to treat a range of diseases. One very common disease that is now regularly treated using minimally invasive methods is atherosclerosis.

### 1.1.1 Atherosclerosis

Atherosclerosis is the build-up of fatty materials such as cholesterol on the artery walls. It is a very common and very serious condition which can affect arteries throughout the body. The build-up of the fatty material, called plaques, causes the artery wall to thicken and become stiffer. This reduces blood flow through the artery which can cause various problems. The plaques can build so much that they eventually block the artery completely or pieces of plaque can break off and travel to smaller blood vessels causing blockages.

It is a chronic disease that can exist for decades without any symptoms and leads to heart disease which is the leading cause of death in the western world [3]. The main cause of atherosclerosis not yet known but it is thought to be due to inflammatory processes caused by the body's immune system responding to damage of the artery wall.

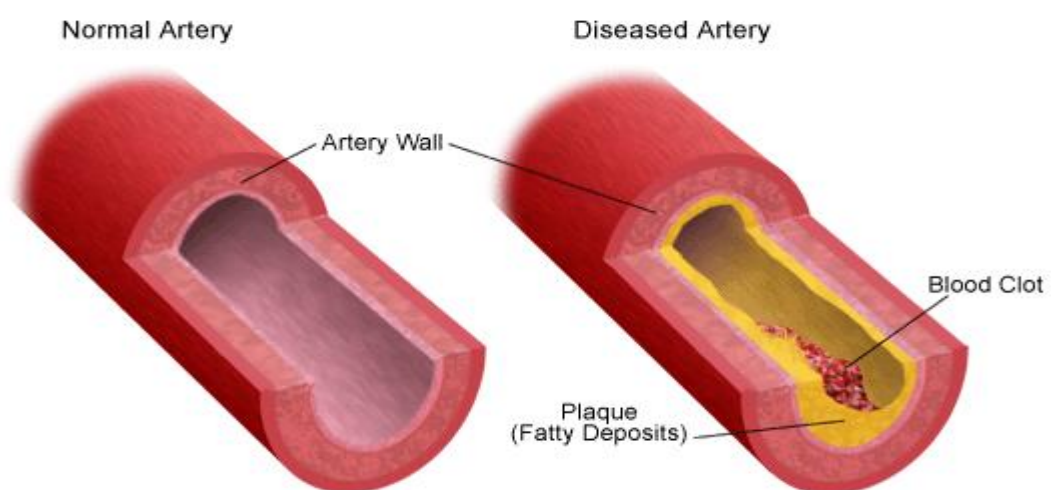


Figure 1.1 Schematic diagram showing build up of plaque in artery. Reproduced from [4].

### 1.1.2 Angioplasty

When a blood vessel has narrowed due to a build-up of plaque a procedure called an angioplasty can be used to mechanically widen the obstructed blood vessel. The device used for this procedure consists of a balloon on a guide wire and is called a balloon catheter. The deflated balloon is inserted into the artery and positioned at the location of the blockage. The balloon is then inflated and it compresses the plaque and widens the blood vessel allowing blood flow to return to normal.

The first angioplasty was performed by Charles Dotter in the U.S. in 1964 [5]. However the procedure did not become popular immediately in the U.S. due in part to difficulties in reproducing the techniques and the occurrence of complications. In 1975 Andreas Gruentzig used Dotter techniques to develop a balloon catheter and in 1977 conduct the first coronary angioplasty on an awake human.

Prior to this, atherosclerosis had only been treatable by invasive surgery. Angioplasty is now one of the most commonly performed surgical procedures and is an excellent example of the success and advantages of minimally invasive surgical techniques.

### 1.1.3 Modern balloon catheters

There is now a large market [7] for balloon catheters with a wide range of different designs available for different uses. They are typically mass-produced from thermoplastics and are inserted into the body along a guide-wire.

The diagram below shows the catheter studied in this work. It is a rapid exchange balloon catheter called the Sterling™ balloon catheter and it is produced by Boston Scientific. This catheter is made of a thermoplastic elastomer called PEBAX® 7033. PEBAX® is a registered trade name for a group of polyether block amides produced by Arkema. The properties that

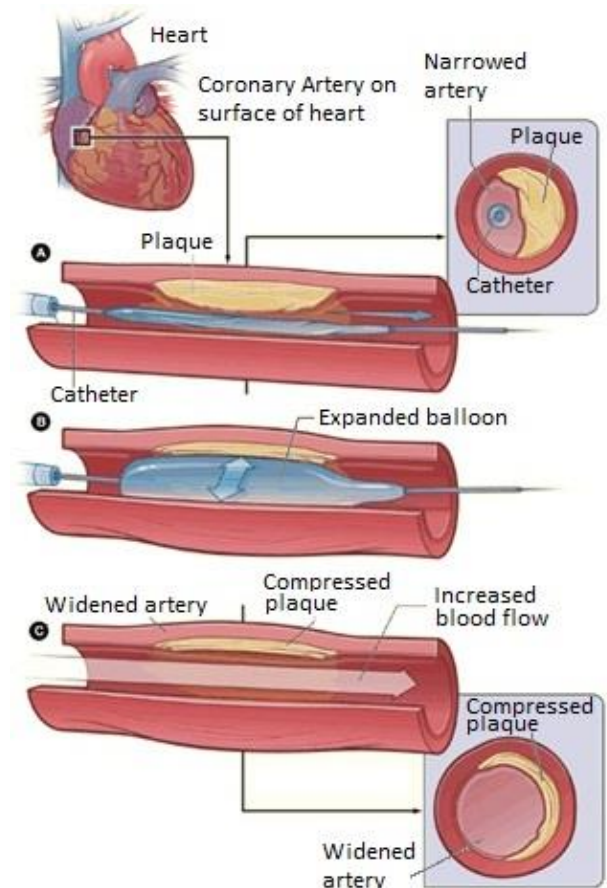


Figure 1.2 Angioplasty procedure. Reproduced from [6]

make PEBAX® a good choice for catheters are: its flexibility; its chemical resistance; its biocompatibility; it is easily sterilized; its compliance with UPS class VI; its ability to be extruded into very thin wall tubes; it is kink resistant; its smooth surface finish and it can be compounded with radiopaque fillers [96][97]. The different parts for the catheters (such as the balloon, the tip, the outer tubing) are produced separately and then they are welded together with lasers. Figure 1.3 shows a schematic drawing of the balloon catheter construction and a photograph (enlarged) of the proximal bond which will be the focus of this work.

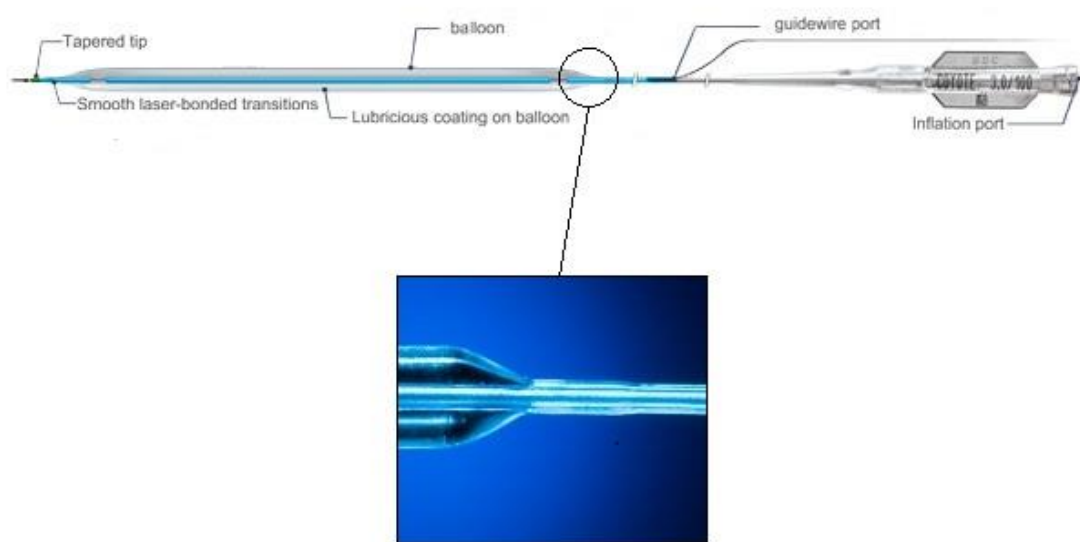


Figure 1.3 Sterling™ balloon catheter currently produced by Boston Scientific. [8].

## 1.2 Laser welding

There are many different techniques for bonding plastics but Boston Scientific has chosen to use lasers as they provide a precise and easily controllable heat source. A common method of laser welding is to use a laser which can travel through the first layer without being absorbed (i.e. the material is transparent to this wavelength) but then gets absorbed at the interface between the materials. It is absorbed either because the second layer is opaque or an opaque dye is placed between the layers. This method is called Laser Transmission Welding (LTW) and it produces a very localized heat field. However, the welding process used by Boston Scientific employs heat and pressure and therefore the function of the laser is to heat both the heat-shrink tubing and the PEBAX® layers. To do this Boston Scientific uses CO<sub>2</sub> lasers which produce an infra-red beam with a wavelength of 10.6  $\mu\text{m}$  and radiation at this

wavelength is absorbed readily by both the heat-shrink and the PEBAX<sup>®</sup>. Boston Scientific have measured the absorption coefficients of the heat-shrink and the PEBAX<sup>®</sup> by measuring the intensity of a CO<sub>2</sub> laser after it had passed through PEBAX<sup>®</sup> and heat-shrink layers of different thicknesses [94]. The absorption coefficient of the PEBAX<sup>®</sup> was measured as 18898 m<sup>-1</sup>, which means that the intensity of the light passing through the PEBAX<sup>®</sup> halves every 37 μm. The absorption coefficient of the heat-shrink was measured as 3543 m<sup>-1</sup>, which means that the intensity of the light passing through the heat-shrink halves every 196 μm.

To achieve a circumferential joint, the joint assembly is rotated at high speed during the laser welding process. This method ensures that the heat-shrink is heated thoroughly and that enough PEBAX<sup>®</sup> is melted to produce the desired melt flow. The interaction of the laser beam with the assembly produces a spatially-varying volumetric heat source. Modelling this heat source is the first step in creating a thermal model of the bonding process.

### 1.3 Proximal bond

Figure 1.4 below shows a cross-sectional sketch of a balloon catheter at the point where the balloon is joined to the main shaft of the catheter, called the outer tube. This area is called the proximal bond as it is closer to the surgeon during use. The bond at the other end of the balloon is known as the distal bond. The work described in this thesis focuses on the proximal bond because there is more data available on the proximal bond and because this bond is axisymmetric. The fact that this bond is axisymmetric makes it less computationally expensive than modelling other bonds such as the port bond which would require a full 3D model.

To form the proximal bond the balloon is placed over the outer tube. Heat-shrink is then placed over the balloon. The purpose of the heat-shrink is to apply a pressure to the assembly to help the balloon bond to the outer tube. An infra-red (IR) laser is used to heat up the assembly. As the assembly heats up the heat-shrink tubing shrinks and applies a pressure to the two layers of PEBAX<sup>®</sup> (the balloon and the outer tube). The main purpose of the heating is to cause intermolecular diffusion from one part to the other. This mixing process is what forms the bond when cooled.

The heating also causes the PEBAX<sup>®</sup> to melt and flow under the pressure from the heat-shrink. This flow produces a smooth tapered surface, as shown in Figure 1.5, which aids in the insertion and extraction of the tube. A model which could predict this melt flow would

be of great use to Boston Scientific and this is one of the major goals of this project. To model the melt flow, it is first necessary to accurately model the heat-shrink tubing.

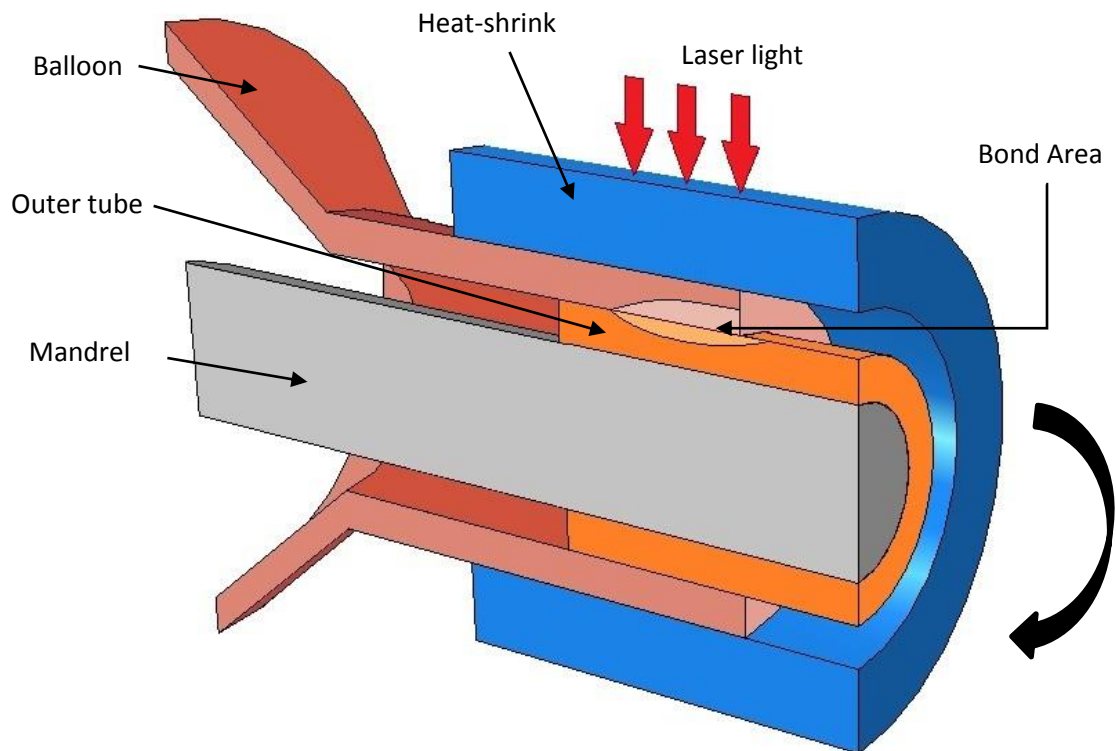


Figure 1.4 Setup for welding of proximal bond. The assembly is rotated at 500 RPM during the laser welding process.

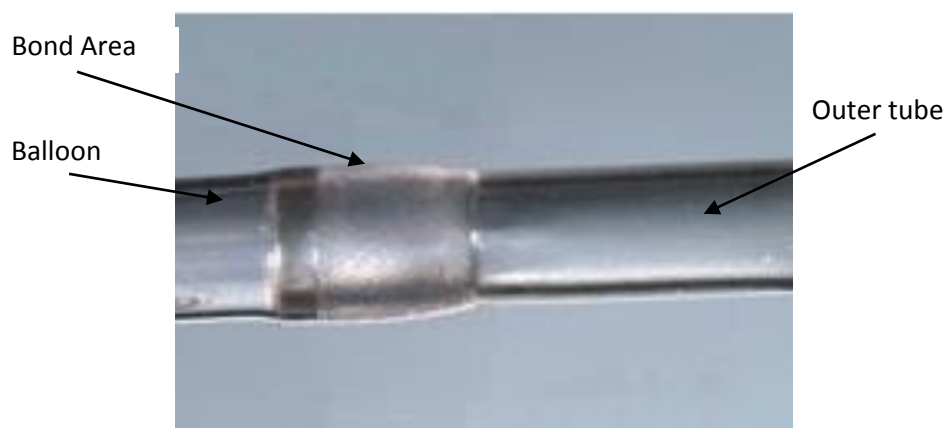


Figure 1.5. Tapered proximal bond after welding

## 1.4 Shape memory polymers

The shape-memory effect in polymers describes the ability to store a deformed shape indefinitely and recover entirely the undeformed shape in response to specific environmental stimulus [67]. The heat-shrink tubing used by Boston Scientific in the laser bonding process is a type of shape-memory polymer (SMP). Heat-shrink tubing can be made from a range of thermoplastics and the heat-shrink used by Boston Scientific is a polyolefin tubing made by Raychem called RNF-100®. The thermomechanical cycle of a SMP is shown schematically below in Figure 1.6. The shape of the polymer after forming (e.g. extrusion or moulding) is called the original or permanent shape. In Figure 1.6 this is represented by the shape in the top-centre. Going clockwise from the top-centre the material is heated above its glass transition temperature,  $T_g$ , so that it is in a rubbery state, then it can be elastically deformed. This causes a stress in the material but when cooled below  $T_g$  the material becomes glassy and the bonds formed during this transition prevent the material recovering to its original shape. The polymer will then remain in this deformed state (bottom-centre of Figure 1.6) until it is heated above  $T_g$ . This heating breaks down the glassy bonds and causes the polymer to re-enter the rubbery state. This releases the elastic energy stored in the polymer which causes the material to revert back to its original shape.

SMPs have been used for years as heat-shrink tubing, packaging, etc. but SMPs are now being developed for uses in medical devices, sensors and actuators. A review of the applications of SMPs is given by Behl and Lendlein [9]. When SMPs only had very simple uses (heat-shrink tubing for installing electrical wires, etc.) there was very little work done in understanding their behaviour. But as they have started being developed for advanced applications, a comprehensive understanding of their behaviour is now of great interest.

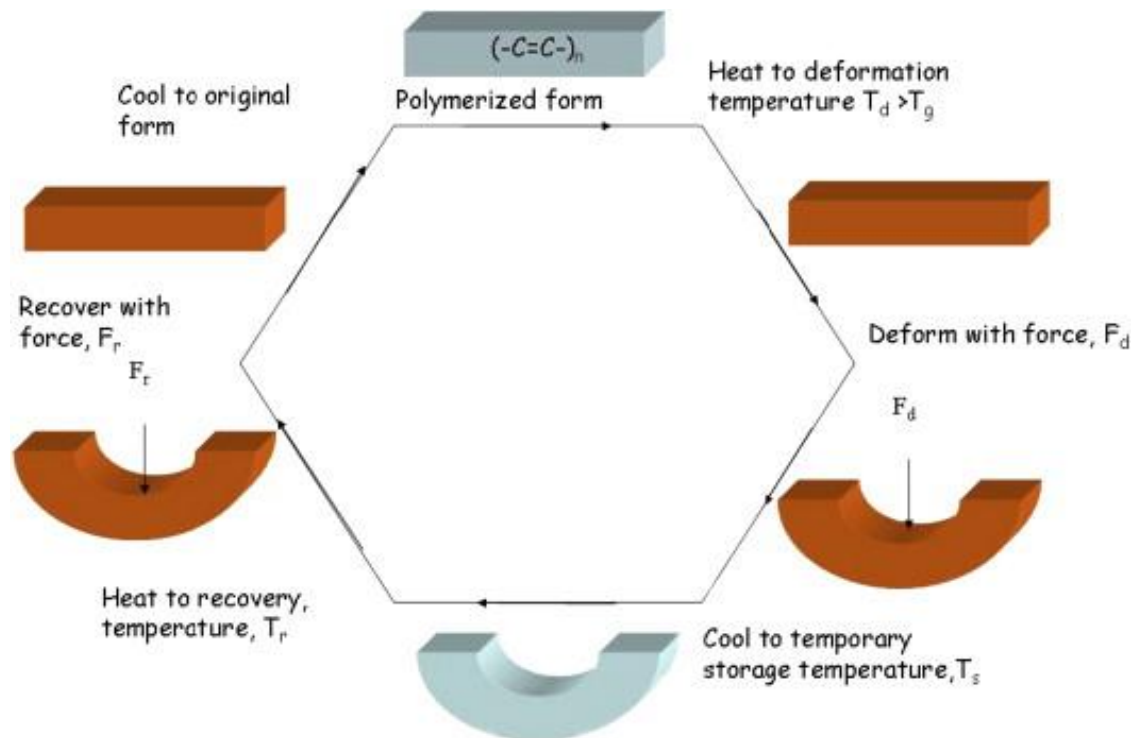


Figure 1.6 Shape Memory Polymer heat deformation cycle. [10]

Shape Memory Polymers can be activated at  $T_g$ , as mentioned above, but the melting point of semi-crystalline networks can also be used to trigger shape recovery. This type of SMP is often referred to as a crystallisable SMP (CSMP). Heat-shrink tubing falls into this category of polymer. In CSMPs the polymer is semi-crystalline and partially cross-linked.

## 1.5 Objectives

The overall objective of this work is to develop an understanding of the thermo-mechanical behaviour of the laser welding process of balloon catheters during laser welding assembly. A computational finite element model is developed in this work to contribute to this understanding. This will involve modelling the temperatures, stresses and melt flow during the welding process. The overall objective has been divided into four main parts.

The first objective of this project is to create a thermal model which can accurately predict the temperatures in the assembly during the laser welding process.

The second objective of this project is to create a model for the heat-shrink tubing. This material will be modelled using a SMP model from the literature. To implement this model in the commercial finite element code, Abaqus FEA, a user defined material model (UMAT) is developed through programming a user subroutine. The material model is then used to

simulate the processing of the shape memory material to represent the stored elastic energy as illustrated schematically in Figure 1.6.

The third objective of this work is to model the melt flow of the bonded region. This will consist of combining the thermal model and heat-shrink model with a model that represents the PEBA<sup>X</sup>® as it is heated to above its melt temperature.

The fourth objective is to use the model to analyse and achieve a better understanding of the welding process. This improved understanding will help in the future design of catheters and will potentially speed up the development process and reduce trial and error experimentation when developing new products.

## **1.6 Thesis overview**

In this thesis, experimental and computational methods are used to address the objectives outlined above. Chapter 2 gives a detailed overview of the background literatures relevant to this work and provides a context of previous work performed in the field and also of methods developed to characterise and represent shape memory polymer materials. Chapter 3 gives an overview of all the experimental testing methods used to characterise and test the thermo-mechanical behaviour of the materials used in this work. The results of these experimental characterisation tests are given in Chapter 4. These experimental results provide inputs into the development and calibration of the shape memory polymer model as well as providing data for validation of its performance.

Chapter 5 describes the investigation into the thermal modelling of the laser welding process. The temperature profiles are examined and compared to those determined from experimental tests. Chapter 6 describes the development of a user defined material behaviour to represent the behaviour of the shape memory polymer, and also describes its performance in accurately representing the thermo-mechanical behaviour of this two-phase material. Chapter 7 goes on to describe the utilisation of this shape memory polymer UMAT in thermo-mechanically modelling the welding process of the balloon catheter assembly and the PEBA<sup>X</sup>® material as it transitions through its melting temperature. A discussion on the overall thesis is given in Chapter 8 where conclusions are made and future work is described.

## **2 Literature Review**

### **2.1 Laser welding of polymers**

Laser beam welding of polymers was considered in the early years of laser technology [11] but at the time there were less expensive solutions to the problem of polymer welding [12] such as hot gas welding and friction welding. However, as polymers have found more and more applications, welding demands arose which could not be easily met with conventional technologies. Also the cost of laser systems has decreased rapidly in recent years while the quality has improved substantially, leading to laser welding being used in many industries such as automotive, electrical and medical devices [13].

During the laser welding of polymers the parts are clamped together and then heated with the laser. The clamping holds the parts in place and is necessary to maintain a pressure at the weld seam, which is important for a good bond. The heat generated by the laser absorption causes the polymer parts to melt. This results in molecular diffusion between the two parts and a solid joint forms as the polymer cools and solidifies. The two main forms of laser welding of polymers are laser transmission welding and CO<sub>2</sub> laser welding.

Laser Transmission Welding (LTW) is the most widely used laser welding technique and also the most discussed in the literature. This technique usually uses Nd:YAG or diode lasers which produce light in the near-infrared (NIR) part of the spectrum which can pass through many polymers. In LTW one part must be transparent to the laser light while the other part absorbs it. The parts are arranged so that the laser travels through the transparent part and is absorbed at the boundary between the transparent part and the absorbent part. This heats up the absorbent part which then heats the transparent part by conduction across the boundary. This technique produces a weld with a small heat affected zone because it delivers the heat directly to the joining area. This process was first described for welding automotive components in [14]. To make the second part absorb the radiation, it is often necessary to add an appropriate pigment [15, 16].

The major advantages of LTW include:

- It produces high quality welds.
- The rapid heating results in a short weld time.

- The energy input is very controlled and localised.

There are still challenges to overcome with LTW such as extending the range of colours of weldable parts. This can be overcome by placing a certain absorbing material between the (transparent) parts but this is not always acceptable due to polymer compatibility, toxicology or cost efficiency.

LTW has been considered by Boston Scientific but they opted to use a different welding technique instead. The welding technique used by Boston Scientific uses a CO<sub>2</sub> laser. CO<sub>2</sub> lasers produce light with a wavelength of 10.6 μm. Light at this wavelength is readily absorbed by most plastics and this leads to rapid heating from the surface through the parts. This rapid heating allows for very rapid processing of thin polymer films. Coelho *et al.* [17] demonstrated welding of polymer film at speeds of up to 10 ms<sup>-1</sup>. Due to the opacity of most plastics at 10.6 μm and the low thermal conductivities of plastics, CO<sub>2</sub> lasers are only used for welding thin plastic films. In thick samples there would be excessive heating at the surface and not enough at the joint area. This is the main reason why CO<sub>2</sub> lasers are not used as extensively as diode (NIR) lasers. The main advantages of CO<sub>2</sub> welding are that it is fast, simple and can be used on any polymer.

## 2.2 Modelling of laser welding of polymers

Currently the majority of laser welding applications rely on experimentation to determine process parameters. An accurate model would enable optimization of process parameters without the need for extensive trial and error experimentation.

The modelling process needs to incorporate various factors such as laser distribution and absorption, heat transfer temperature, pressure and many material properties that vary with temperature. Models can be analytical, such as that described in [18], or more commonly numerical finite element models.

The finite element method (FEM) is a useful tool for material processing simulation. There has been a large amount of work done in applying FEM to the modelling of laser welding of metals and a detailed literature review in this area was carried out by Mackwood and Crafer [19]. However, there are a relatively small number of researchers who have used FEM to model the laser welding of plastics. The main difference between welding plastics and metals is that in metals the laser is absorbed within the first few nanometres whereas in plastics the

laser is absorbed over a scale of a few millimetres (for CO<sub>2</sub>). Also metals have much higher thermal conductivities and melting points.

Mayboudi *et al.* [20] and Frick [21] created and tested an FEM model to predict the temperature profile in laser transmission welding. When modelling the temperature profile in a laser welded part, the first thing to consider is the laser absorption. Light absorption within a solid can be described by the Beer-Lambert law:

$$I(z) = I_0 e^{-\alpha z} \quad (2.1)$$

where  $I(z)$  is the intensity of the beam as a function of depth into the material,  $I_0$  is the intensity at  $z=0$  and  $\alpha$  is the absorption coefficient. This equation is appropriate in the case of absorbent polymers and is widely used [18, 23 and 24]. However for polymers with a low absorption coefficient, the scattering of the laser beam becomes an important issue as demonstrated experimentally by Potente *et al.* [25] and Becker *et al.* [24]. Potente *et al.* [25] defined a correction factor which took the scattering into account and supported their results by comparing the experimentally observed melt layer thickness with the model predictions. These materials scatter light because they are inhomogeneous. This can be due to their semi-crystalline structure or the presence of impurities or additives. Ilie [26] has modelled this scattering using the Mie theory and the Monte Carlo method. This numerical model allows a good estimation of the laser beam profile after it has passed through the transparent layer in LTW.

Most polymers have a high absorption coefficient for CO<sub>2</sub> laser radiation and therefore the Beer-Lambert Law can be applied. However, Coelho *et al.* [27] have found that polyethylene samples thinner than 200  $\mu\text{m}$  have high transparency since the attenuation length is larger than the sample thickness. They proposed methodologies for determining the optical properties (at 10.6  $\mu\text{m}$ ), which involves using an integrating sphere to determine reflectance and transmittance and using these values to determine the complex refractive index. Geiger *et al.*, [28] also used integrating spheres to determine the optical properties of polymers for laser welding and use these properties in an FE simulation of the temperature fields during LTW. One conclusion from this work on polypropylene was that the change of absorption coefficient with temperature had a negligible effect on influencing the melt pool geometry. However, Van de Ven [23] stresses the importance of measuring  $\alpha$  as a function of temperature for the absorbing PVC part in LTW.

The heat transfer resulting from the laser absorption has also been investigated. Heat transfer in a material can be modelled using the general heat conductivity equation [29]. In three-dimensional Cartesian space this can be written as follows:

$$\frac{\partial}{\partial x} \left( k_x(T) \frac{\partial T}{\partial x} \right) + \frac{\partial}{\partial y} \left( k_y(T) \frac{\partial T}{\partial y} \right) + \frac{\partial}{\partial z} \left( k_z(T) \frac{\partial T}{\partial z} \right) + Q(x, y, z, t) = \rho(T)C(T) \frac{\partial T}{\partial t} \quad (2.2)$$

where  $\rho$  is the density,  $C$  is the specific heat capacity,  $T$  is the temperature,  $t$  is time,  $k$  is thermal conductivity and  $Q(x, y, z, t)$  is the heat generation rate. In the case of laser welding the heat generation rate is equal to the light absorption given by the Beer-Lambert law in Equation 2.1 above.

This heat conduction equation can be solved numerically [20-22] or analytically [30] and many researchers now report good agreement between the temperature fields predicted by the models and those observed by experiment.

One interesting heat transfer result came from Coelho *et al.*, [30]. They found that 30% more energy needed to be applied in practice compared to the model. They concluded that gaseous by-products released during the initial moments of processing were absorbing the laser radiation just above the plastics surface. This led to the formation of a plasma on the surface of the materials which was directly observed experimentally.

In addition to the temperature field during welding, the pressure is also of interest. External pressure is applied to the parts to improve the weld quality. Also thermal expansion of the two materials during the welding process can create pressures and tractions. Van de Ven and Potente [22, 23] found that the pressure was not usually a significant factor in LTW as long as excessive limits were not exceeded. Therefore, for many researchers the pressure has not been a crucial factor. However, the CO<sub>2</sub> welding process used in Boston Scientific is different from most of the LTW processes because the surface material melts and flows due to the heat and the pressure applied. Therefore, pressure is more likely to be an important factor.

A study of the residual stresses in polymers after LTW was conducted by Potente *et al.*, 2008 [33]. In this work, material equations were developed to describe the elasto-viscoplasticity at different temperatures and were included in a model developed using the Abaqus FEA software. The main finding of this work was that the model could predict the influence of the process parameters on the development of the residual stresses in the LTW parts.

An earlier paper by Potente and Fiegler [34] presents an Abaqus FEM model, along with experimental data, of melt displacement and temperature profiles for LTW. An interesting

point to note from this work was the use of tracer particles to monitor the melt displacement during the laser welding process. These tracer particles were Tungsten spheres (dia. 75-70  $\mu\text{m}$ ) and were detected using micro-focus radioscopy. This allowed the chronological and spatial displacements of these particles to be recorded throughout the welding process. This data was then compared to the calculated flow profile and the model was found to be in good agreement with experiment.

Often the main objective of thermal modelling is to get a temperature profile at the end of the heating phase, i.e. just as the laser is turned off (as this is when the temperatures are at a maximum) and therefore there is no need to run the simulation after the laser is turned off. However, an important point to note from literature [34] regarding the thermomechanical modelling is that the cooling phase should also be modelled as stresses and strains can change during this period.

The welding process in Boston Scientific uses heat-shrink tubing to provide an external pressure on the assembly to aid welding. Heat-shrink tubing has not been characterised extensively in the literature, probably because it is normally used for simple applications such as installing electrical wires. Also, there are no studies in the literature where the thermo-mechanical behaviour of heat-shrink tubing has been modelled, perhaps due to the commercial sensitivities around revealing processing parameters. However, there is a substantial amount of literature on the related area of shape memory polymers (SMPs). This is discussed in the following section.

### 2.3 Shape memory polymers

As mentioned previously the heat-shrink tubing used by Boston Scientific is a type of shape memory polymer (SMP) and modelling this is a major goal of this work. A large amount of research has been published on characterizing and modelling SMPs. Various reviews exist already [35-39] and they range from the broad overview by Mather *et al.* [36] to more narrowly focused reviews such as the review of cardiovascular applications by Yakacki *et al.* [35] and the review of multifunctional SMPs by Behl *et al.* [37].

Figure 2.1 is a graph of the stress and strain of a sample during an SMP cycle. In step 1 the sample is stretched at a high temperature (50°C) to a strain of  $\epsilon_m$  and is held at this strain for some time. Stress-relaxation occurs and causes the stress to reduce while the strain and temperature remain constant. The temperature is then reduced while the strain is kept

constant (step 2) and this fixes the sample in its temporary shape. When the sample is released (step 3) the stress goes to zero. It remains in this temporary shape until it is heated (step 4) which causes the sample to return to its original shape.

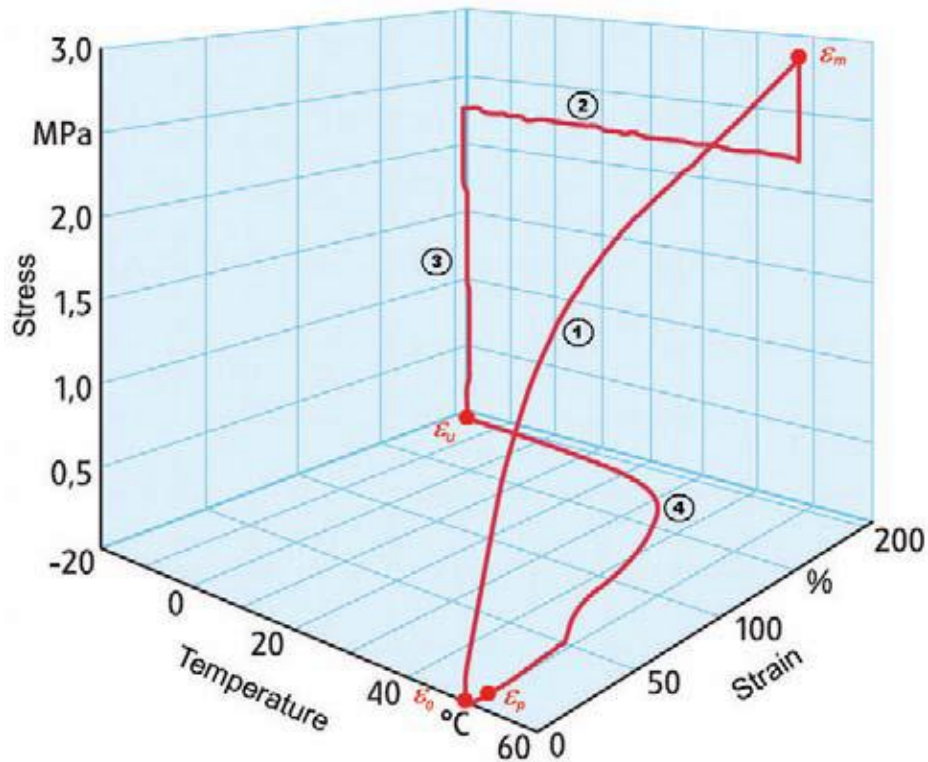


Figure 2.1 The stress-strain-temperature response of an SMP during a typical shape-memory cycle. The sample is stretched (step 1), cooled (step 2), released (step 3) which forms its temporary shape and when it is reheated (step 4) it returns to its original shape [9].

### 2.3.1 Applications and interest

Shape memory alloys (SMA) are currently in use in many industries. In particular, a nickel-titanium alloy called Nitinol is used in many commercial applications. These materials have many merits but also have some limitations which SMPs may be able to overcome.

One of the main advantages of SMPs over SMAs is that SMPs can have very large recoverable strains of up to 400% [40] whereas SMAs maximum strain recovery is about 8% [41]. Also SMPs are inexpensive to manufacture. They are malleable, damage-tolerant and the recovery temperature can be adjusted by changing the chemical structure and composition [35]. These properties mean that SMPs have potential applications in a wide variety of industries.

One area where SMPs could have a large impact is in biomedical applications. Various authors have investigated SMP stents [35, 42, 43]. Lendlein and Langer [44] created a biodegradable SMP suture. Small *et al.* [45] describe a SMP device for the removal of blood clots. Sokolowski *et al.* [46] discuss using SMPs in cardiac pacemakers, vascular grafts and artificial hearts.

Sokolowski *et al.* [47] discusses SMP-based deployable structures for space applications. Other uses include smart fabrics [48], self-disassembling mobile phones [49] and actuators [50, 51]. A comprehensive list of SMP applications has been produced by Meng *et al.* [52] along with a review of recent attempts to strengthen SMPs and Rousseau [53] has reviewed progress toward overcoming the limitations of SMPs.

### 2.3.2 Materials and categorization

Liu *et al.* [54] classify SMPs in 4 categories based on differences on fixing mechanism and the origin of permanent shape elasticity.

#### *Covalently cross-linked glassy thermosets network*

These SMPs are activated at their glass-transition temperature ( $T_g$ ). Above this temperature the material has a rubbery elasticity which provides for a high degree of shape recovery.

#### *Covalently cross-linked semi-crystalline networks*

This class of SMP uses the melting temperature of the semi-crystalline network to trigger shape recovery. Heat-shrink is in this group.

#### *Physically cross-linked glassy co-polymers*

These SMPs have the advantage that their permanent shape can be altered as opposed to covalently cross-linked SMPs whose permanent shape is fixed after the polymer has been moulded or extruded.

#### *Physically cross-linked semi-crystalline block co-polymers*

These SMPs are activated at the melting temperature and can also have their permanent shape reprocessed by thermal processing above 100°C.

### 2.3.3 Characterization

There has been a large amount of work done on the characterization of SMPs. Early work on the properties of SMPs was performed by Liang *et al.* [56] and Hayashi *et al.* [57]. Tobushi *et al.* [58] examined the thermomechanical properties of shape memory polyurethane films, including modulus, yield stress, shape fixity and shape recovery. Lendlein *et al.* [41] discuss the properties of various different SMPs. In particular they discuss how the molecular structure of the polymer affects the strain recovery ratio and the mechanical properties. Gall *et al.* [59] examined the storage and release of internal stress in a SMP cycle. Beblo *et al.* [60] discuss anisotropic properties of SMPs which occur due to the application of a large strain. Diani *et al.* [61] have recently described a new torsion test to study large deformation recovery in SMPs. However, there is very little data available for the SMP used in this work (RNF-100® heat-shrink tubing) so it was necessary to characterise the thermomechanical properties in detail so that the material could be modelled accurately.

The most common methods for characterization of the mechanical properties involve a dynamic mechanical thermal analyser (DMTA) [58, 62, 63, 64, 65, 66]. With the DMTA the temperature-dependent properties of polymers can be assessed quickly and many different types of tests can be performed with it. The DMTA can measure properties including, the complex modulus as a function of temperature, recovery behaviour, viscoelasticity and yield stress. Due to its prevalence in the literature and its versatility, DMA was chosen as the main method for the characterization of the heat-shrink tubing.

## 2.4 Modelling of SMPs

Most work on SMPs has concentrated on experimental characterization especially in the early years of SMP research. However, as SMPs are being used in increasingly complex and ambitious ways, there is a need to be able to predict their behaviour accurately. Many models have been published in the last few years with increasing complexity and accuracy. Nguyen [67] has recently performed a comprehensive review of these models.

There are two main approaches to modelling SMPs 1) Models which are based on standard viscoelasticity with various rheological elements 2) Models which are based on the existence of two separate phases.

### 2.4.1 Thermo-viscoelastic modelling approaches

Many authors have tried to model SMPs using combinations of parallel and series arrangements of rheological elements which have temperature-dependent constitutive relations for the viscosities and/or moduli to affect strain storage and recovery. Tobushi *et al.* [69] proposed a linear constitutive model but this was not valid for large strains. In order to express behaviour at large strains this model was modified [70] to account for nonlinear behaviour and the proposed theory is useful for determining some basic characteristics of SMPs such as the amount of shape recovery and start and completion temperatures.

Morshedian *et al.* [71] also used temperature-dependent rheological elements (springs, dashpots) to create a mechanical model of SMPs. This model was developed to model the stress-strain-time behaviour of heat-shrinkable polyethylene. The proposed mechanical model is shown below in Figure 2.2A. A focus of this work was stress relaxation which can prevent the full dimensional recovery of heat-shrinkable materials. It was found that this stress relaxation occurs during the strain holding/cooling time before the formation of crystallites at the solidification point. If the elapsed time before crystallization is long enough (in this case 30 h) then the elastic restoring force completely releases, resulting in zero shrinkage. The mechanical model was capable of describing the experimental results observed in shape memory induction and dissipation very well after some model parameters were determined by experiment.

Nguyen *et al.* [72] developed a finite deformation model for amorphous SMPs which incorporated a time-dependent model of the glass transition and a structural relaxation model. This model is shown in Figure 2.2B. The model was implemented in an FE program and it reproduced many of the important features of the stress and strain recovery response, such as the hysteresis in the stress-temperature curve and the peak stress during reheating. However some quantitative differences remain such as the unconstrained recovery response and the strain recovery time.

Ghosh *et al.* [73] propose a two-network model which is based on the Helmholtz potential (Figure 2.2C). This work highlights the sensitive dependence of the response on thermal expansion and the importance of modelling the hysteresis in the yield stress during temperature change. This model was developed for small-strain analysis and was implemented in MATLAB. The model results agree well with experiment.

Diagrams of four SMP models based on rheological elements are shown below in Figure 2.2.

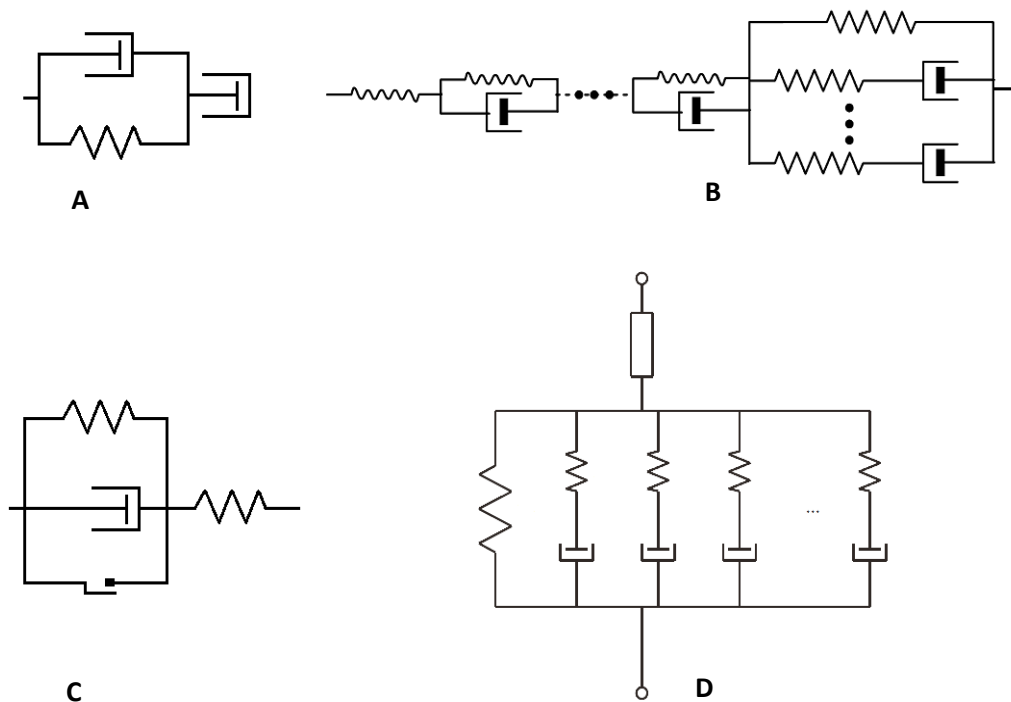


**Figure 2.2** Four SMP models based on rheological elements A) Morshedian *et al.* [71], B) Nguyen *et al.* [72], C) Ghosh *et al.* [73] and D) Westbrook *et al.* [74].

Westbrook *et al.* [74] builds on previous work by Castro *et al.* [75] and Nguyen *et al.* [72] to create a new multi-branch model to capture the SM effect and various relaxation processes of amorphous SMPs. This model is shown in Figure 2.2D and the results of this model are compared with experimental results and are shown below in Figure 2.3. In this experiment a cylindrical sample was heated to 60°C, then subjected to a compressive strain of 20% and cooled to lock-in the deformation (cooling shown in Figure 2.3) . The sample was then reheated (heating shown in Figure 2.3) while the strain was kept at 20% in a constrained recovery experiment. As the sample is reheated the thermal expansion of the material causes a large increase in the compressive stress. As the sample is heated further the material becomes more compliant and the stress reduces.

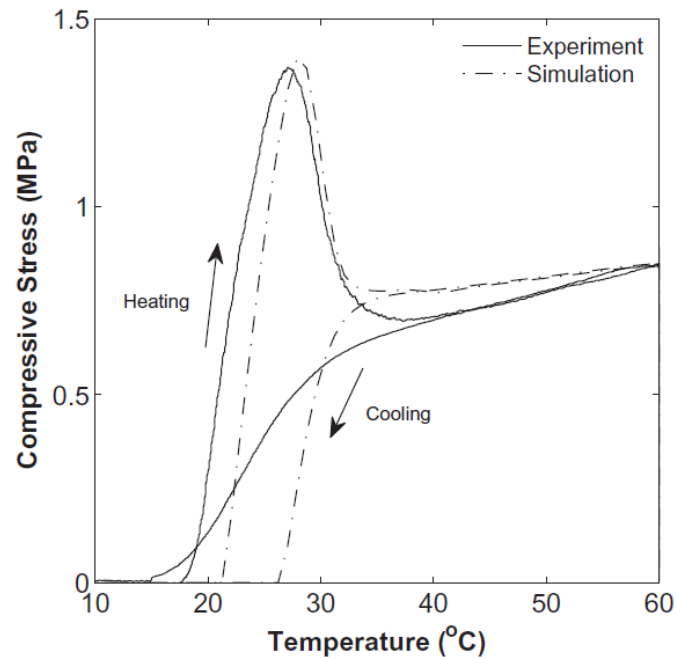


**Figure 2.3 Comparison between numerical simulation and experimental results for the stress response during a constrained recovery shape memory cycle [74].**

This model was implemented in 2D in a user subroutine (UMAT) for the FE package Abaqus FEA. The model involves a significant number of parameters (exact number depends on number of branches used) and a protocol is provided to identify these parameters. The model simulations are compared with a range of thermomechanical experiments and show very good agreement.

#### **2.4.2 Phase transition modelling approaches**

Many researchers take an alternative approach to modelling SMPs and use the concept of two separate phases. This method was first introduced by Liu *et al.* [64]. Their model is based on the thermodynamic concepts of entropy and internal energy. They adopt the concept of “stored” strain into a simplified thermomechanical model. In this model the SMP material is modelled as a mixture of two kinds of extreme phases, the “frozen phase” and the “active phase”. In the frozen phase the material is relatively rigid while in the active phase the material is easily deformed. An SMP cycle of this model is shown in Figure 2.4. This model applies to SMPs which change shape at the  $T_g$  of the polymer. The volume fraction of each phase changes with temperature. In the glassy state, below  $T_g$ , the frozen phase is the major phase but as the material is heated the frozen fraction reduces and the active fraction increases. Above  $T_g$ , when the active fraction has completely replaced the frozen fraction, the polymer is in the rubbery state. The 1-D constitutive equation (excluding thermal expansion) for this model is

$$\sigma = E(\varepsilon - \varepsilon_s) \quad (2.3)$$

where  $\varepsilon_s$  is the stored strain. This model uses a rule of mixtures to derive an equation for the Young's modulus of the polymer as a function of temperature.

$$E = \frac{1}{\frac{\phi_F}{E_F} + \frac{1-\phi_F}{E_A}} \quad (2.4)$$

Where  $E_F$  and  $E_A$  are the moduli of the frozen phase and active phase respectively and are assumed to be constant and  $\phi_f$  is the frozen fraction which can be calculated from:

$$\phi_F = 1 - \frac{1}{1 + c_f (T_h - T)^n} \quad (2.5)$$

In this equation,  $c_f$  and  $n$  are variables which can be determined by experiment as described in [64] and  $T_h$  is an arbitrary temperature above  $T_g$  where the polymer is in the full rubbery phase.

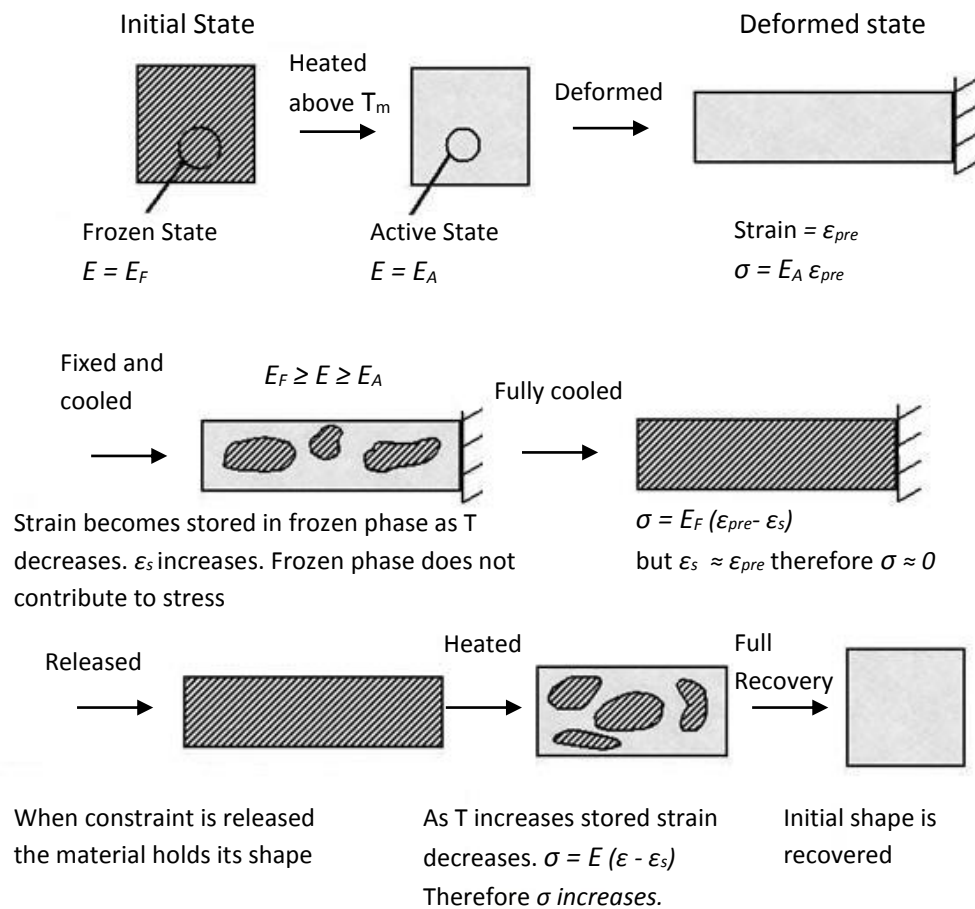


Figure 2.4 The stored strain model of Liu *et al.* [64] of a thermomechanical cycle of an SMP.

This model is demonstrated only for small strains. Chen *et al.* [76] continued on this idea to develop a three-dimensional constitutive theory for large deformations.

The general concept of considering two phases within the polymer with different mechanical properties is very common as evident from Nguyen's recent review [67] of SMP models. Barot *et al.* [77] use a multiple natural configurations approach along with the framework that was developed recently for studying crystallization in polymers [78] to model the behaviour of CSMPs. They formulate constitutive equations to describe the interaction between an amorphous phase and a semi-crystalline phase. The modelling is divided into four parts, namely, the rubbery phase ( $T > T_m$ ), the semi-crystalline phase ( $T < T_m$ ), the crystallization process (on cooling through  $T_m$ ) and the melting process (on heating through  $T_m$ ). The hyperelastic behaviour of different materials can be modelled within the Barot *et al.* framework and it is demonstrated with the Neo-Hookean model. The equation for the stress in a Neo-Hookean material is

$$\boldsymbol{\sigma} = \frac{\mu}{J} \text{dev}(\mathbf{B}^*) + \kappa(J - 1)\mathbf{I} \quad (2.6)$$

Where  $\mu$  is the shear modulus,  $\kappa$  is the bulk modulus,  $J$  is the determinant of the deformation gradient  $\mathbf{F}$ , and  $\mathbf{B}$  is the left Cauchy-Green deformation tensor and  $\mathbf{I}$  is the identity tensor. The model was used to simulate a typical uniaxial cycle of deformation and the results compare very well with the experimental data.

Kafka [79], following on from work on shape memory alloys [80], proposes a model which assumes there are two continuous three-dimensional substructures in SMPs. One substructure remains elastic with a constant Young's modulus. The other substructure is assumed to deform in an elastic-plastic-viscous way with Young's modulus decreasing with increasing temperature. This is a very general model and simulated results agree well with experimental data but at the moment it is only valid for small strains.

Qi *et al.* [81] develop a 3D finite deformation model based on the two phases approach. The hyperelastic behaviour of the rubbery phase is modelled using the Arruda-Boyce eight-chain model which captures the material behaviour up to large strains. This model was implemented in a UMAT and compared with uniaxial experiments. The model captured the isothermal stress strain behaviour and the shape memory effects during heating and cooling. However it did not capture the stress recovery implying the simple volume fraction evolution rule which was used is not accurate enough.

### 2.4.3 Applications of SMP models

While many SMP models have been proposed there has been very little work done in applying these analytical models to industrial applications through the use of numerical models. In 2009 Reese *et al.* [43] developed a 3D SMP model and applied it to a SMP stent through the use of computational finite element modelling. This work is purely qualitative and is not compared to experimental data. Reese *et al.* stated “To our knowledge FE-based simulations of 3-D [shape memory polymer] structures are not found in any previous publication”. This is echoed by Ghosh in 2011 [73], “There is a paucity in experimental data in the 3D response of [shape memory polymer] materials”.

## 2.5 Summary and contribution

The work presented in this thesis aims to contribute to the knowledge within the field through applying the analytical models of Liu *et al.* [64] and Barot *et al.* [77] to simulate the behaviour of shape memory polymers within 3D and axisymmetric models with the purpose of applying these models to the laser welding of a Boston Scientific balloon catheter joint. The model of Liu *et al.* was chosen for initial exploratory modelling work, primarily for its simplicity. The Barot *et al.* model was chosen because it provided a flexible framework that would enable the modelling of large deformations with a relatively simple hyperelastic material model.

A lot of work has been done on characterisation and modelling of SMPs. However there is very little data available for the RNF-100® heat-shrink tubing and there has been very little work done on applying these models to industrial applications. The main three novel contributions of this work are:

1. To accurately characterise and understand the thermomechanical behaviour of the RNF-100® heat-shrink tubing used in the laser welding process. There is no data in the literature on many of the properties needed to model this material such as modulus as a function of temperature, modulus as a function of strain, viscoelasticity and plasticity.
2. To use an SMP model in an industrial FE application and compare the results with experimental data. To our knowledge this has not been done before.

3. This work represents the first thermomechanical simulation of the laser bonding of balloon catheters. This model will combine heat-transfer, an SMP material and a model of a molten polymer in order to predict the melt flow that occurs during the welding process. There is no model like this in the literature.

This work has the potential to make a strong contribution to the field in terms of improving the understanding of the welding process and reducing the need for trial and error experimentation in the early product development stage of catheters.

### 3 Experimental methods

This chapter contains details of the experimental techniques used in this work. The majority of the techniques described here are used to characterise the material properties of the heat-shrink tubing. Some imaging techniques are also described which are used to image the catheter after welding. The determined material properties are used as inputs in calibrating the constitutive behaviour of the heat-shrink material through the development of a user defined material model, as described in Chapter 6. The PEBA<sup>®</sup> properties were obtained from existing literature. Also, separate experimental data is used for validating the performance of the computational model developed.

The majority of the techniques described here are well known and widely used in industry and academia. However, a new experimental technique was also developed and validated to characterise the pressure-volume relationship, and hence elastic modulus, of small-gauge heat-shrink tube as a function of temperature. Another experiment, known as the hanger test, as developed by Boston Scientific, is also described and used to characterise / validate material properties.

It is crucial in any model to know the properties of all the materials involved as accurately as possible. During the welding process the temperature of the heat-shrink reaches 240°C (as measured by Boston Scientific the IR thermometer (Land M6)) and the PEBA<sup>®</sup> reaches approximately 200°C (model prediction [93]) and the whole welding process takes approximately 20 seconds. As the properties of polymers depend on temperature and time it is important to define the ranges relevant to the process. With this in mind a list of properties needed was drawn up and a series of tests were devised to obtain these properties. Extensive testing was carried out at 120°C because it was found that when testing at higher temperatures, the material would discolour and it became stiffer. The high temperatures and extended duration of the tests may have caused the sample to react with the oxygen in the air. However it was found that the modulus is relatively insensitive to temperature above the crystalline melting point of approximately 100°C (see Figure 4.4) and so it was decided that it was acceptable to test at 120°C.

### 3.1 Dynamic mechanical thermal analysis

A dynamic mechanical thermal analyser (DMTA) measures the modulus and the damping of a viscoelastic material, as a function of temperature, as it is subjected to a sinusoidal stress. The modulus is the ratio between stress and strain and in a viscoelastic material the modulus,  $E^*$ , is a complex quantity,

$$E^* = E' + iE'' \quad (3.1)$$

where  $E''$  is the loss modulus and  $E'$  is the storage modulus.  $E''$  represents energy dissipated during deformation of the sample, and  $E'$  refers to the ability of a material to store energy.

A viscoelastic material has properties which contain elements of both elastic and viscous behaviour. In an elastic body, stress and strain are in phase, and stress is proportional to strain. In viscous fluids stress and strain are  $90^\circ$  out of phase and stress is proportional to the rate of strain. In a viscoelastic material under sinusoidal loading, the strain is between  $0^\circ$  and  $90^\circ$  out of phase. The strain lags behind the stress, this lag is represented by the phase angle  $\delta$  [82],

$$\tan(\delta) = E''/E' \quad (3.2)$$

The sample is placed in the DMTA which exerts a periodic tensile force of known frequency on it. This force is usually sinusoidal but complex waveforms can also be used. The temperature is increased at a set rate as a function of time and the force and displacement are measured as a function of temperature. Figure 3.1 shows a sample clamped within the DMTA.



Figure 3.1 Setup for DMTA tensile test in which a sample is clamped

Dynamic mechanical thermal analysis can be used to determine the glass transition, relaxation spectra, degree of crystallinity, molecular orientation, phase separation and structural/morphological changes of copolymer blends. In this work the DMTA was mainly

used to determine the modulus of the heat-shrink in different conditions. The DMTA was also used to determine the thermal expansion coefficient.

## 3.2 Heat-shrink tests performed on DMTA

As heat-shrink tubing is an SMP the parameters that needed to be measured depend on the model that will be used. To decide on which model to use tests were performed to determine the degree of plasticity and viscoelasticity.

The properties needed for the stored strain SMP model of Liu *et al.* [64] are

- i. The modulus of the frozen phase
- ii. The modulus of the active phase
- iii. The frozen fraction
- iv. The thermal expansion coefficient  $\alpha$

Once these properties were known the model could be calibrated. To validate the model a recovery force experiment was performed.

The heat-shrink tubing used in the welding process has a diameter of 2-3 mm and a wall thickness of approximately 0.4 mm which makes testing the properties very difficult with standard approaches and techniques. Due to this a large size (diameter 70 mm) heat-shrink tube was obtained for Boston Scientific. This large tube was made from the same material and was processed in the same way as the smaller tube. The heat-shrink tubing was pre-shrunk in an oven at 120°C to remove the shape memory effect for all of the tests except the recovery force test. The large heat-shrink tubing was used to determine the qualitative properties of the heat-shrink material however the final quantitative data used for the model was determined from the small heat-shrink tubing which was the tubing used in the experiments.

### 3.2.1 Frequency sweep

The DMTA was used to measure the variation of the modulus of the heat-shrink varied with frequency. A rectangular sample measuring 8 mm x 30 mm x 1.2 mm was cut out of pre-shrunk heat-shrink as shown in Figure 3.2. Five samples were measured and placed in the DMTA.

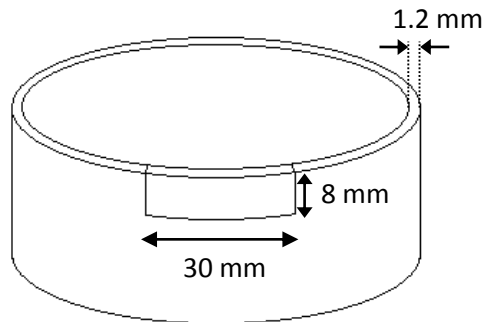


**Figure 3.2 Sample preparation for large size heat-shrink tube in circumferential direction**

The chamber was heated to 120°C and left for 5 minutes to come to thermal equilibrium. Then a sinusoidal strain of 0.5 % was applied. The frequency of the applied strain was varied from 0.1 Hz to 100 Hz. The load required is used to calculate the modulus and this is plotted against frequency. This test was repeated for five samples at 120°C and five samples at 30°C. This plot is used to assess the viscoelastic properties.

### **3.2.2 Temperature dependence of elastic modulus**

Two methods were used to measure the elastic modulus as a function of temperature: A dynamic method and a static method. For the dynamic method a rectangular sample of heat-shrink was placed in the DMTA. The temperature was ramped from 20°C to 120°C at a rate of 2°C/min. A small sinusoidal load of 0.5 % strain was applied to the sample and the force required to maintain this load was recorded by the DMTA. The DMTA software calculated the stress and strain from the applied force and sample dimensions and also calculated the modulus as a function of temperature. Ten samples were used for each of these tests.

The static method also used rectangular samples in the DMTA. However, in the static method a number of tensile tests were carried out at different temperatures and the modulus was for each tensile test. In these tests the temperature was increased in intervals of 10°C and then the temperature in the chamber was held constant for 5 minutes before the tensile test was performed. The pause was to allow the sample to reach the same temperature as the chamber. The tensile test was performed to a low strain value to minimize the plastic

behaviour. The modulus was calculated by measuring the slope of the stress/strain curve for each tensile test, and then the modulus was plotted as a function of temperature.

### 3.2.3 Thermal expansion coefficient $\alpha$

The DMTA was also used to measure the thermal expansion coefficient  $\alpha$ . A sample of pre-shrunk heat-shrink was placed in DMTA. A small constant load of 0.001 N was applied then the sample was heated up at a rate of 2°C/min and the change in displacement was measured. A load of zero would be ideal but this was not possible in the DMTA. The test was carried out with a tensile load and with a compressive load to minimize the error introduced by the material straining under the small load. This test was repeated for five samples.

### 3.2.4 Plasticity

The plastic behaviour of the heat-shrink was characterised in the DMTA by performing tensile tests to various different strain levels. The stress/strain curves are the plotted for loading and unloading and the amount of plasticity can be measured in the strain that is not recovered during unloading. All plasticity tests were carried out at 120°C.

### 3.2.5 Anisotropy

The properties of polymer tubes are often different in different directions due to extrusion processes. To measure this, tensile tests were performed on samples cut from the axial direction and these were compared with samples cut from the circumferential direction.

### 3.2.6 Frozen fraction

The frozen fraction,  $\varphi_f$ , is a parameter used in the stored strain SMP model of Liu *et al.* [64] and not an intrinsic material property. The method used by Liu *et al.* was to fit a curve to the free strain recovery curve. This is a somewhat arbitrary curve to choose but it produces good results. In this work another method was attempted using data from differential scanning calorimetry (DSC). DSC measures energy flowing into a sample during heating at a constant rate and reveals how much energy is absorbed or released during phase transitions. The

extra energy absorbed by the sample during the melting of the crystalline phase was used as a measure of the frozen fraction.

The other method used was an approximation of the free strain recovery used by Liu *et al.* where the strain is measured during the recovery of an unconstrained sample. The Liu *et al.* experiment was performed with a video extensometer and a heated chamber but the experiment used in this work was performed in the DMTA. A small sinusoidally varying load was applied to a sample of heat-shrink and the temperature was ramped slowly. As the heat-shrink recovered the DMTA records the change in displacement. This gives a strain recovery as a function of temperature graph which was used to fit a curve to the frozen fraction.

### **3.2.7 Recovery force tests**

To measure the recovery force of the large-size heat-shrink tubing, rectangular samples were cut and placed in the DMTA. A small preload was applied and then the temperature was ramped from room temperature up to 120°C at 2°C/min. When the crystalline phase of the heat-shrink melts the rubbery phase tries to contract. This produces a force which is measured by the DMTA. This test was repeated twenty times.

### **3.2.8 Stress relaxation tests**

Stress relaxation experiments were performed to investigate the effect of time on the shrink force. In these tests a sample is held at a constant strain in the DMTA and the drop in stress is measured over time. The sample was heated to 120°C and then stretched to a strain of 5%. The strain was held constant for 10 minutes and the stress was measured. These tests were repeated three times.

## **3.3 Differential scanning calorimetry**

In differential scanning calorimetry (DSC), the temperature of a sample and a reference pan is raised at the same rate and the heat flow required to keep the samples at the same temperature is measured. The difference in heat flow is then plotted as a function of temperature. Changes in the heat flow indicate phase changes and these appear as peaks and dips in a plot of heat transfer rate as a function of temperature. DSC can be used to determine heat capacity, purity, and degree of crystallinity as well as measuring the

enthalpies of chemical reactions and phase changes that occur during heating of a material. A typical DSC output is shown below in Figure 3.3. The three phase changes shown in this figure show the glass transition  $T_g$ , the crystallisation temperature  $T_c$  and the melting temperature  $T_m$ .

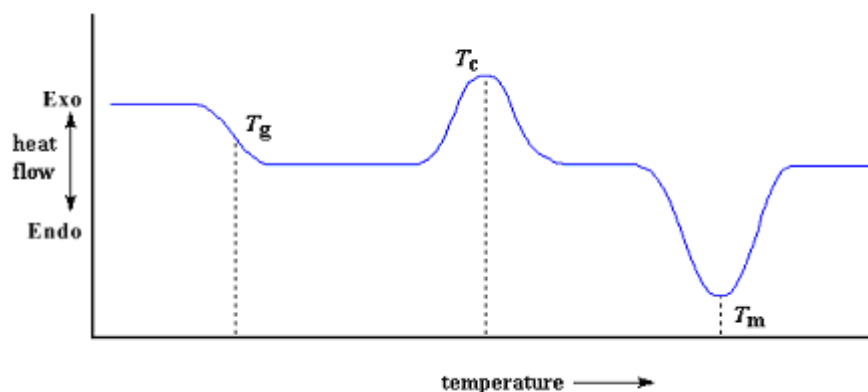


**Figure 3.3** Typical output from a DSC indicating the glass transition  $T_g$ , the crystallisation temperature  $T_c$  and the melting temperature  $T_m$ .

The sample to be investigated is placed on an aluminium pan and a lid is crimped onto the pan. This prevents the sample interacting with the nitrogen which is used to heat the furnace. The samples used are typically 2-50 mg in mass. Another pan is prepared and left empty. This is used as the reference pan. The chamber is small so it can heat up and cool down fast. The temperature increases at a predetermined rate and is monitored by two thermocouples. Heat flow differences between the sample and reference pan will occur due to exothermic or endothermic reactions in the sample.

The heat capacity,  $C_p$ , is the quantity of heat,  $q$ , needed to increase a unit mass of a material by  $1^\circ\text{C}$  and is calculated using Equation 3.3

$$C_p = q/\Delta T \quad (3.3)$$

where  $\Delta T$  is the change in temperature. A step in the DSC curve indicates a change in heat capacity.

Above the glass transition temperature, molecules have more freedom to move and so the sample can absorb more heat. This leads to an increase in heat capacity, which is represented by a downward step on the graph.

When the sample reaches a certain temperature, crystallisation begins as the molecules begin to move in ordered arrangements. This means the material gives off heat and this is represented by a large peak in the graph. The area under the peak is the latent energy of crystallisation.

Melting occurs when the molecules have too much energy to be held in a crystal structure. Extra energy is needed to melt the crystals and this results in an endothermic dip in the graph. The area between the dip and the baseline represents the latent heat of fusion of the material.

### **3.4 Microscopy**

Boston Scientific use microscopy extensively to examine the quality and consistency of catheter joint bonds. The two main types of microscopy used by Boston Scientific are polarized microscopy and optical coherence tomography (OCT).

#### **3.4.1 Polarized microscopy**

In polarized microscopy a light microscope is used with two polarizing filters, one between the light source and the sample the other between the sample and the eyepiece. The polarizing filters are set up perpendicular to each other so no light passes through when the sample is isotropic and amorphous. However if the sample consists of optically anisotropic crystals, the light will be split into two rays polarised perpendicular to each other [83]. Some of this light can then pass through the second polarizing filter which produces an image with good contrast.

Sample preparation involves carefully cutting a section out of the catheter in the axial direction. This method of imaging produces a very clear image of the melt pool. However, this is a destructive technique and sample preparation is difficult.

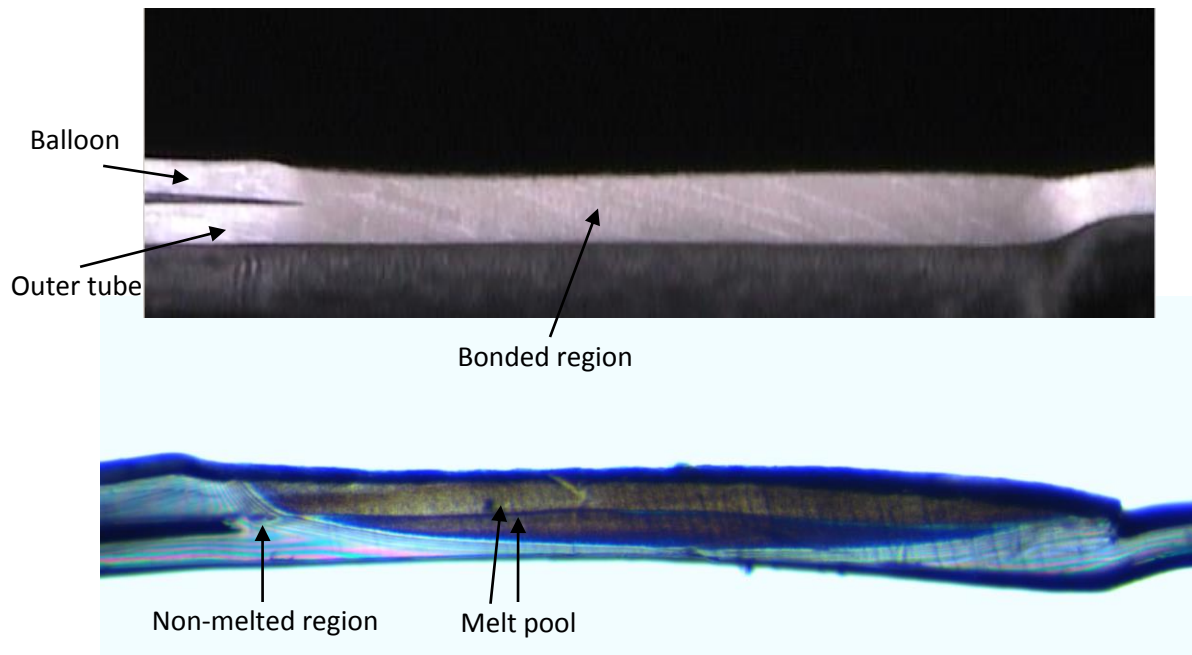


**Figure 3.4 Image showing advantages of polarized light (lower image) over non-polarized light (upper image)**

A comparison of regular microscopy and polarized microscopy is shown above in Figure 3.4. The melt pool is clearly visible in the lower image as the darker region while the rest of the catheter is much brighter. The upper image using non-polarized light produces no contrast between the melted and non-melted regions showing the advantages of polarized microscopy. The material in the catheter is anisotropic due to the extrusion process but when the material is heated above its melting point, the anisotropic crystals melt and the material becomes isotropic. This is the reason the melt pool is much darker than the non-melted region when imaged with polarized microscopy.

### 3.4.2 Optical coherence tomography

Boston Scientific also uses optical coherence tomography (OCT) to image the bonded region. This technique produces a cross-sectional slice image in transparent or translucent samples. The major advantage of OCT over polarized microscopy is that OCT is non-destructive.

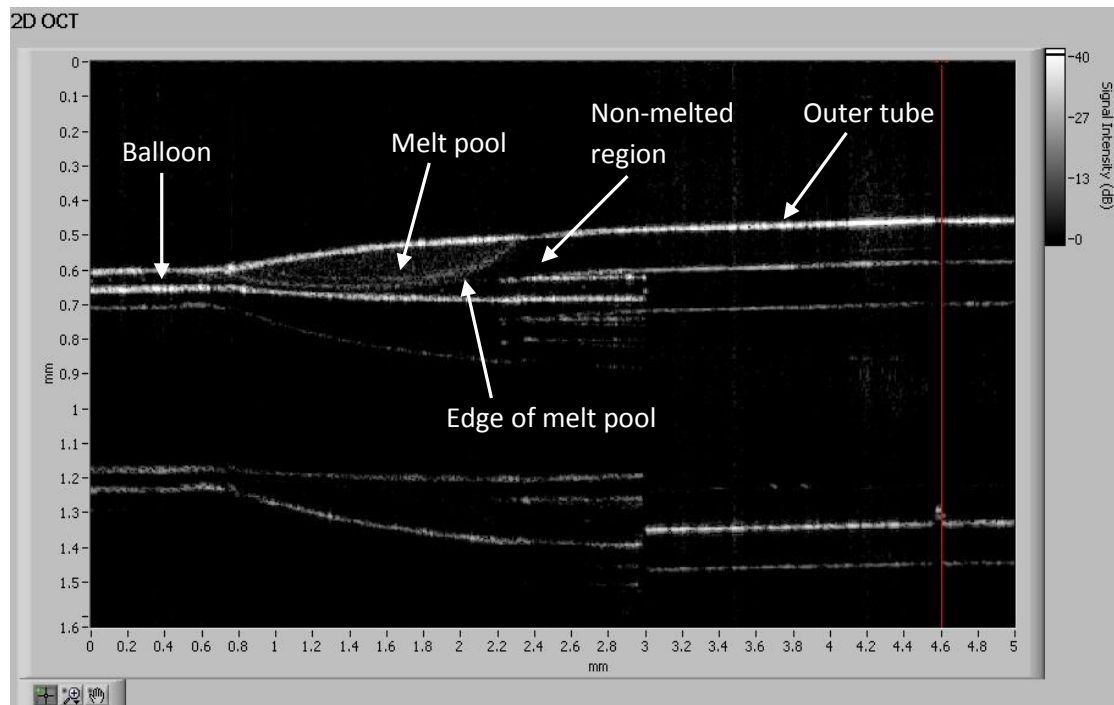


Figure 3.5 OCT image of bonded region of catheter

An OCT image of a bond is shown above in Figure 3.5. The melt pool is clearly visible. Note: the dimensions in the vertical direction below the surface are not accurate due to refraction effects.

### 3.5 Shrink force test

To measure the shrink force of the heat-shrink tubing Boston Scientific developed a test called the hanger test. In this test a short sample (2 mm) of heat-shrink tubing was placed on two horizontal hangers which are held in a fixed position in a DMTA. The setup is shown below in Figure 3.6. The temperature in the DMTA chamber was then ramped up to 150°C over approximately 5 minutes which causes the tube to contract. As the tube contracts it places a force on the hanger and this is measured by the DMTA. The results of this test depend on the distance between the hangers so care has to be taken that the test is setup accurately.

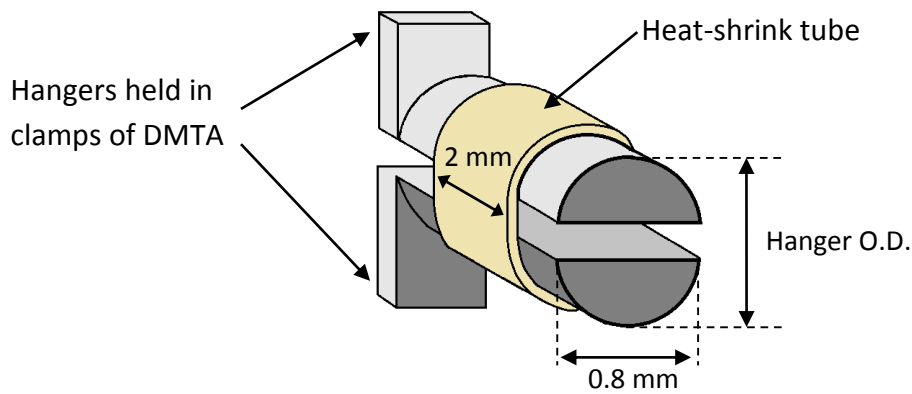


Figure 3.6 Schematic diagram of shrink force test used by Boston Scientific

The change in shrink force as the tube shrinks was also investigated. This was done by varying the outside diameter of the hangers (hanger O.D. in Figure 3.6) and measuring the shrink force as a function of the hanger O.D.

### 3.6 Pressure test

As mentioned in Section 3.2, the heat-shrink tubing used in the laser welding bonding process has a diameter of 2 mm. This makes testing in the DMTA difficult. Therefore, a custom designed pressure test was developed to measure the modulus of the small heat-shrink tubing. The principle of the pressure test is to measure the pressure that the heat-shrink tubing applies to a fluid during a constrained recovery. The dimensions of the tube during the test do not change because the tube cannot compress the fixed volume of oil inside the tube. The internal diameter of the tube in the expanded state is approximately 2 mm and the internal diameter of the recovered tube is approximately 1 mm. This test assumes that when the heat-shrink tube is heated to 120°C it exerts a pressure that is equivalent to the pressure that would be needed to expand the tube from the recovered diameter to the expanded diameter. This is equivalent to heating the 2 mm tube, letting it shrink to a stress-free state with a diameter of 1 mm and then pressurising it to expand it again to 2 mm.

As the dimensions of the tube do not change during the pressure test, the pressure of the fluid in the tube is proportional to the modulus of the tube and therefore the modulus can be calculated from the pressure produced. The dimensions were supplied by Boston Scientific [99]. An FE model of this test was used to calculate the modulus from the pressure test results and this is described in Section 4.7.

The pressure is equal in magnitude to the radial stress  $\sigma_r$  at the inner surface of the tube and assuming that there is no axial strain and the material is Neo-Hookean and incompressible, the radial stress at the inner surface of a thick-walled cylinder undergoing finite deformation can be calculated from the equation below [98].

$$\sigma_r = G \left( \frac{A^2 - a^2}{2} \left( \frac{1}{a^2} - \frac{1}{b^2} \right) + \log \frac{Ab}{Ba} \right) \quad (3.4)$$

In this equation  $G$  is the shear modulus,  $A$  and  $B$  are the internal and external radii before the tube is expanded and  $a$  and  $b$  are the internal and external radii after expansion.

In this test a 200 mm length of tube was filled with oil. One end of the tube was sealed with a clamp and the other end was connected to a pressure transducer. The pressure sensor used was a Honeywell SCC SMT which required a supply current of 1 mA and produced an output voltage of 2.9 mV for every 1 psi of pressure measured (including atmospheric pressure). The tube was then immersed in bath of oil which had been heated to 120°C. Upon immersion in the oil bath the heat-shrink tube is rapidly heated to above its crystalline melting temperature. The pressure of the oil within the tube was measured as the heat-shrink tube tried to contract. A schematic diagram of the pressure test set-up is shown below in Figure 3.7.

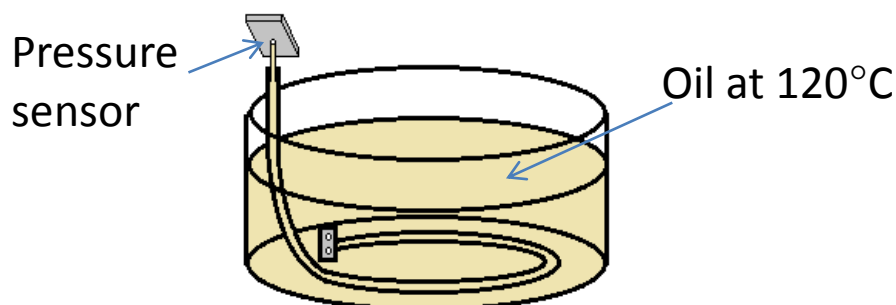


Figure 3.7 Schematic diagram for pressure test

A sealing mechanism had to be created between the heat-shrink and the pressure sensor. The configuration below in Figure 3.8 was decided upon. This allows the tubes to be changed quickly and easily between tests while provided a leak-proof seal. As the nut is screwed in towards the back-plate, it pushes the metal spacer which puts pressure on the rubber seal. As the seal is compressed it pushes the heat-shrink tube against the small steel tube forming a seal.

Once the sealed tube is lowered into the hot oil the pressure inside the tube increases quickly and then drops off with time. To ensure a leak was not causing this drop in pressure, a leak

test was performed. This involved placing the sealed oil-filled tube on flat surface and putting weights on the tube until the pressure inside was approximately the same as that seen when the heat-shrink is placed in the hot oil.

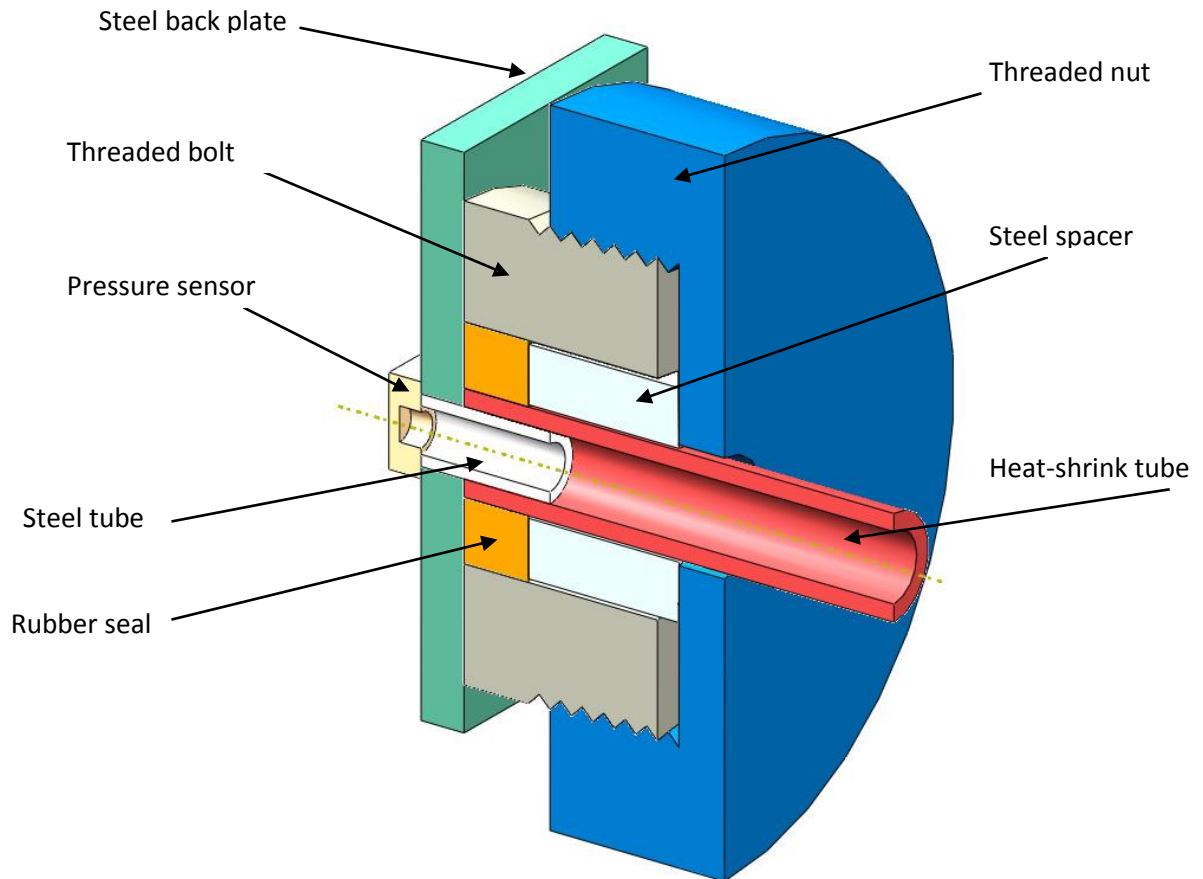


Figure 3.8 Sealing mechanism developed for pressure test

Once leakage had been ruled out a series of tests were carried out on five different grades of heat-shrink. These five types of tube have very similar dimensions and are made from the same material but produce different shrink forces when tested on Boston Scientific's hanger test. This is due to the varying levels of irradiation which the tubes received when they were manufactured. Higher levels of irradiation produce more cross-linking and more cross-linking results in a higher modulus. The modulus of the tubes is calculated from the pressure they produce. To validate this method the modulus was then used as the input into a finite element model of the hanger test. The results of this model were then compared with the results of the hanger test performed by Boston Scientific.

## **4 Results of material characterisation**

This chapter contains the results of the experiments on the heat-shrink tubing described in Chapter 3 and the details of the material model used to model the PEBA<sup>®</sup> which is the material the balloon and outer tube are made from. The objective of this chapter is to comprehensively characterise the polyolefin heat-shrink tubing and to obtain material properties which are required for subsequent modelling. No experiments were performed on the PEBA<sup>®</sup> - PEBA<sup>®</sup> data was obtained from the literature for the PEBA<sup>®</sup> model. The heat-shrink tubing was tested through DMTA and the pressure test as described in Chapter 3.

Two types of heat-shrink tube were tested, the large heat-shrink with a diameter of 70 mm and small heat-shrink (Raychem tab 10 Lot No. 15867) with a diameter of 3 mm. The small tubing is used in the welding process but due to its small size it was difficult to characterise. Therefore, the large tube was used to characterise the behaviour of heat-shrink tubing through more extensive testing. Various characteristics of the heat-shrink tubing were investigated including:

- i. The elastic behaviour
- ii. The effect of viscoelasticity
- iii. The effect of plasticity
- iv. The recovery force
- v. The thermal expansion coefficient

This chapter describes the material behaviour of PEBA<sup>®</sup> through data obtained from the literature and details on how this data was used to create a material model for PEBA<sup>®</sup> to be used in modelling the welding process.

### **4.1 Measurement of elastic modulus of large heat-shrink tube**

#### **4.1.1 Elastic properties under dynamic loading**

The first method used to measure the modulus of the heat-shrink tube was a dynamic test conducted with the use of a Dynamic Mechanical and Thermal Analyser (DMTA). This

involved applying a sinusoidal strain with amplitude of 0.5% at a frequency of 1 Hz and measuring the force while increasing the temperature. These tests were performed on 10 rectangular samples cut from the large size heat-shrink tubing as shown in Figure 3.2. The dimensions of the samples were measured with a digital callipers. The minimum and maximum thickness of the samples were 1.18 mm and 1.22 mm respectively. Some samples were shrunk before testing and some were tested in the stretched (as received) state. Results are shown below in Figure 4.1 below.

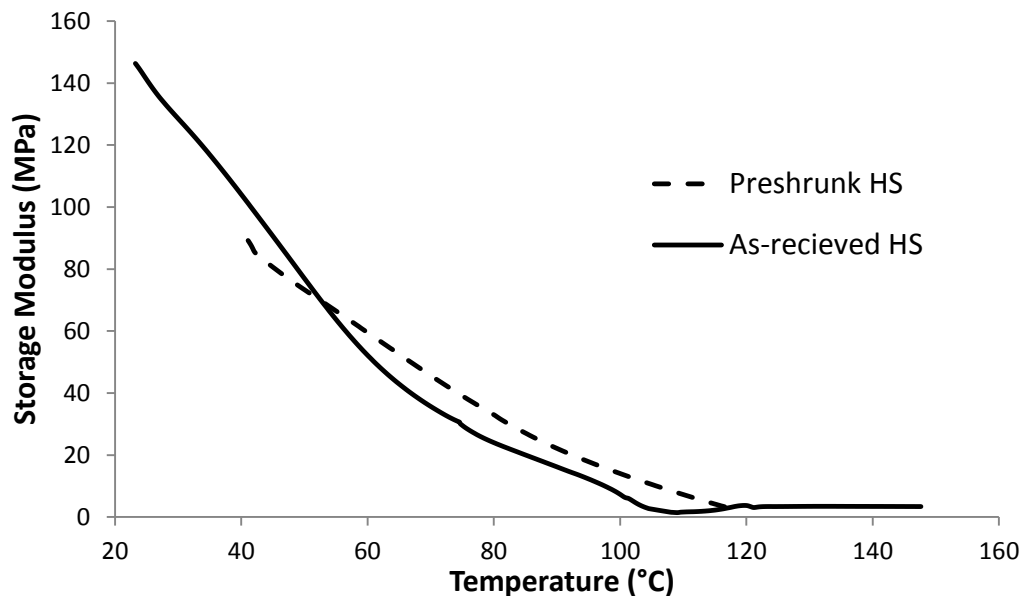


**Figure 4.1** Storage modulus of large-diameter heat-shrink tubing as a function of temperature. Tests were conducted at a frequency of 1 Hz and the heating rate is 2°C/min.

The modulus varies strongly with temperature up to approximately 120°C, after which it stabilises. The modulus at room temperature is approximately 140 MPa and above 120°C the modulus is less than 1 MPa. The curve for the pre-shrunk heat-shrink tubing is more linear than that of the as-received tube. This is due to the shape memory effects in the as-received tube which cause it to shrink during testing.

#### 4.1.2 Effect of frequency

The effect of test frequency on the modulus was also investigated using the procedure described in section 3.2.1. Results are shown in Figures 4.2 and 4.3 for DMTA tests over a range of loading frequencies at constant temperature. In Figure 4.2 tests were performed at 120°C because it was found that when testing at higher temperatures, the material began to react with the air in the chamber. However it was found that the modulus does not vary a lot with the temperature above the crystalline melting point of approximately 100°C (as seen

in Figure 4.4, the modulus at 1 Hz decreases by 5 % when the temperature is increased from 120°C to 160°C), and so it was decided that it was acceptable to test at 120°C. Figure 4.4 below shows the variation in modulus over a smaller frequency range at three different temperatures.

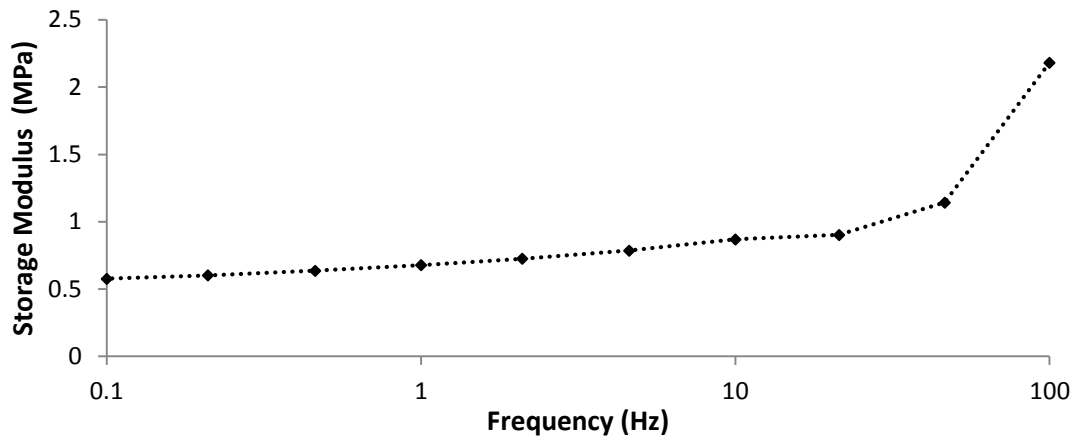


Figure 4.2 Storage modulus of large-diameter heat-shrink tubing as a function of frequency. Tests were performed at a constant temperature of 120°C with loading in the circumferential direction.

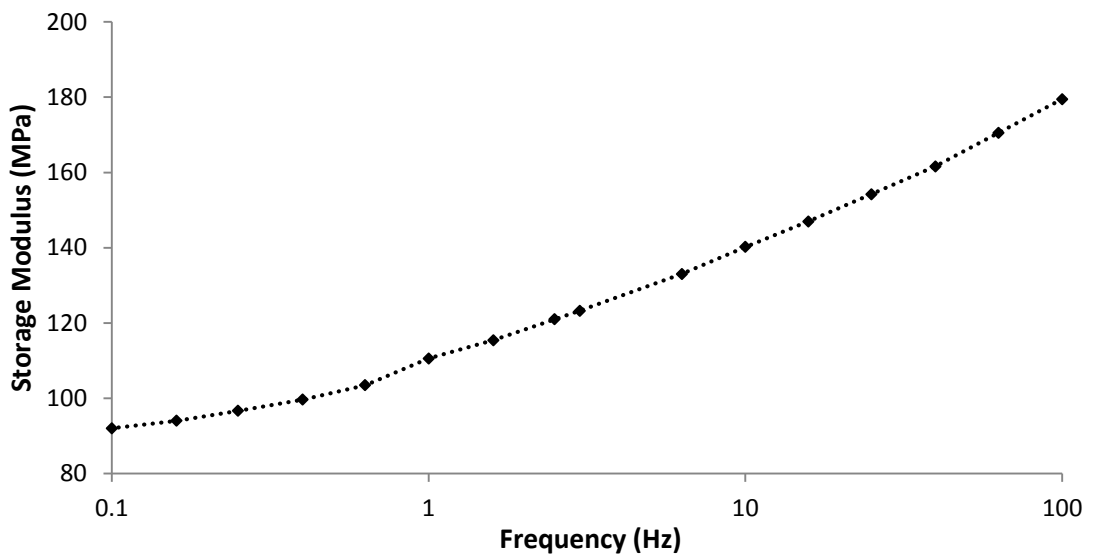
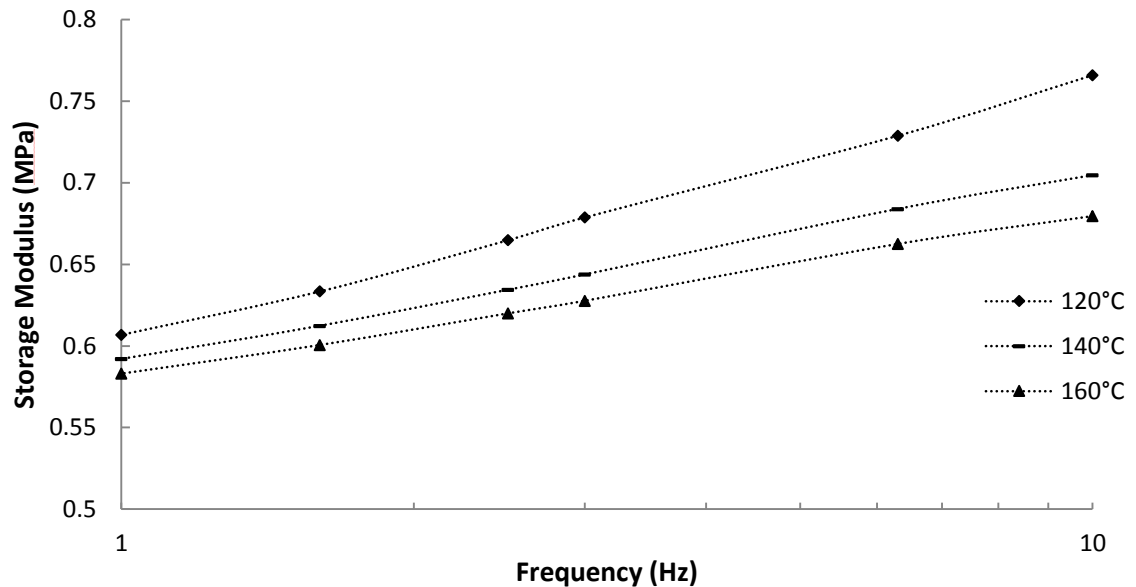


Figure 4.3 Storage modulus of large-diameter heat-shrink tubing as a function of frequency. Tests were performed at a constant temperature of 30°C with loading in the circumferential direction.



**Figure 4.4** Storage modulus of large-diameter heat-shrink tubing as a function of frequency for 3 temperatures.

These results show that the heat-shrink tubing is a viscoelastic material, as the modulus increases slightly with higher frequency. The welding process takes place over approximately 20 s, and so the lower ranges of frequency are more relevant than the higher ranges. It is not known what causes the increase in modulus between 20 Hz and 100 Hz in Figure 4.2, but deformation at these high frequencies are not relevant to the laser welding process.

From Figure 4.4 it can be seen that the change in modulus from 120°C to 160°C is very small at low frequencies but increases at higher frequencies. The change in modulus from 1 Hz to 10 Hz is approximately 20%. The highest temperature reached during the welding process is approximately 245°C.

#### 4.1.3 Static tests

Static tests were also performed in the DMTA to determine the stress-strain relationship. This involved tensile testing at 120°C and at strain rates of 30%/min. The welding process takes place over 20 seconds and during this time the diameter of the heat-shrinks halves. The strain rate varies significantly over the 20 s and it varies throughout the heat-shrink and therefore choosing a strain rate to do the tests at was difficult. The maximum strain rate in the process occurs during the free recovery of the heat shrink at the centre of the laser, before it comes into contact with the PEBA<sup>®</sup>. In this region the strain reduces by approximately 40% over approximately 2 s. However, the heat-shrink strain rate when the

PEBAX® begins to flow (the most important part of the process) is in the region of 30%/min and lower. This is estimated from the change in radius of the outer tube during the welding process. The radius of the outer tube decreases by approximately 0.05 mm over approximately 10 s and this equates to a 5% change in strain over 10 s for the heat-shrink; therefore a strain rate of 30% was chosen for these tests. Figure 4.5 below shows a stress-strain curve for the loading and unloading of a rectangular sample of the large heat-shrink tubing in the circumferential direction. It can be observed that the stress-strain relationship is non-linear. Figure 6 shows the repeated loading of a single sample with increasing levels of strain.

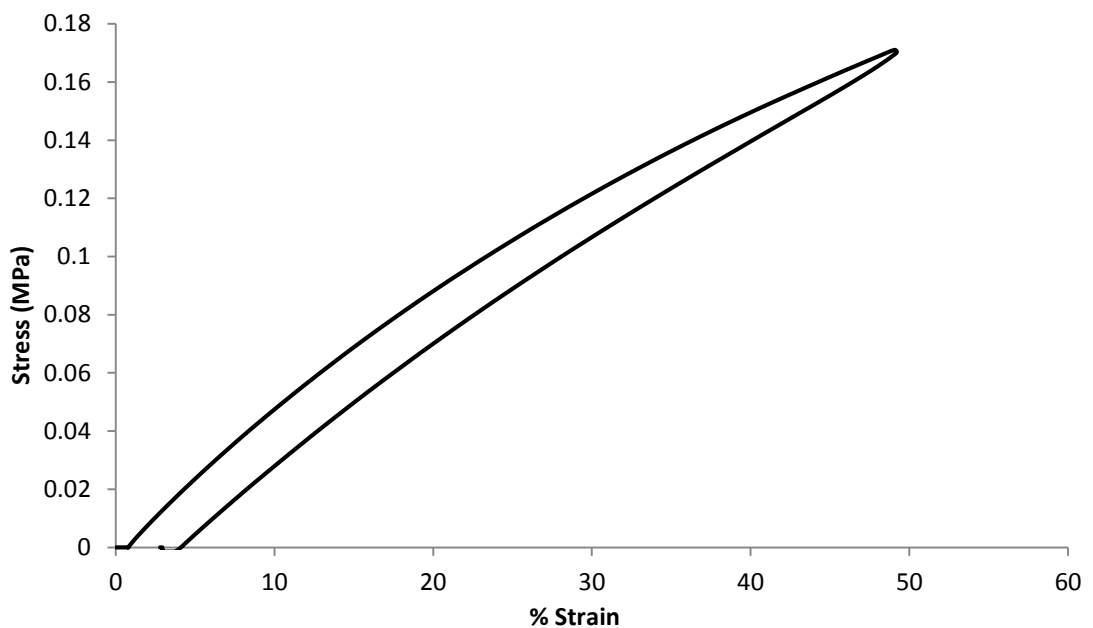


**Figure 4.5 Tensile loading and unloading of heat-shrink at 120°C. Test performed in the circumferential direction and with a strain rate of 30%/min.**

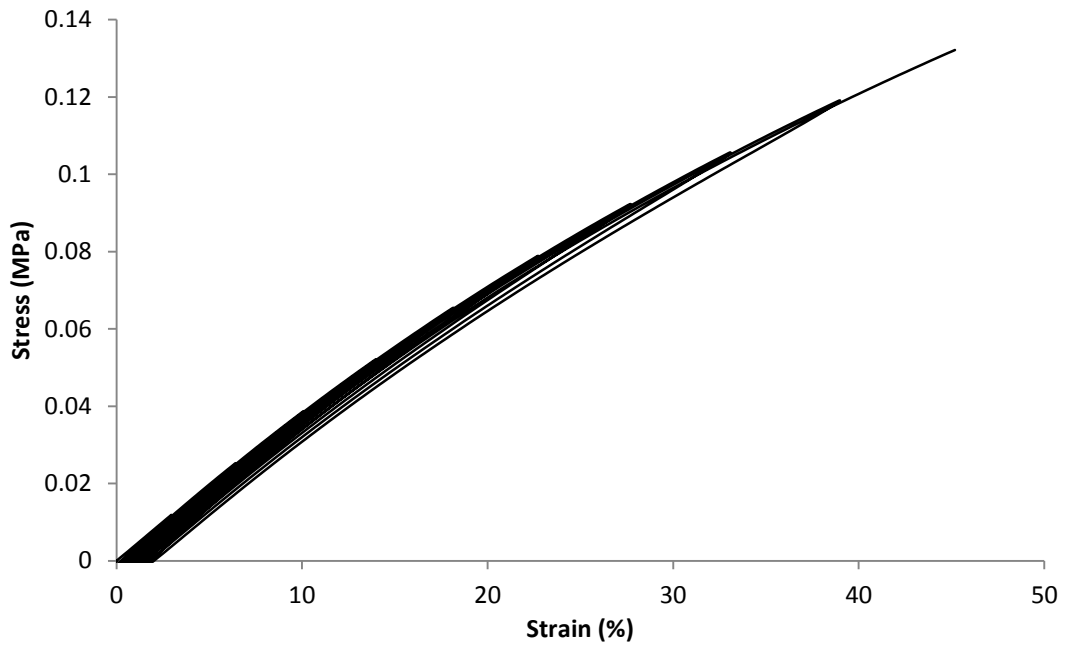


**Figure 4.6** Repeated loading of a single sample. Testing was conducted at 120°C.

These curves show that when the heat-shrink is stretched to 45% strain about 2.5% strain is not recovered due to plasticity. This is quite a small amount of plasticity. At higher strain values slipping in the clamps became significant.

Static tests were also performed at a range of temperatures to compare with the dynamic (DMTA) results. Figure 4.7 below shows the conditions used for these tests and Figure 4.8 shows the results. Young's modulus is calculated by measuring the slope of the stress/strain curve, which at low strain levels is very linear.

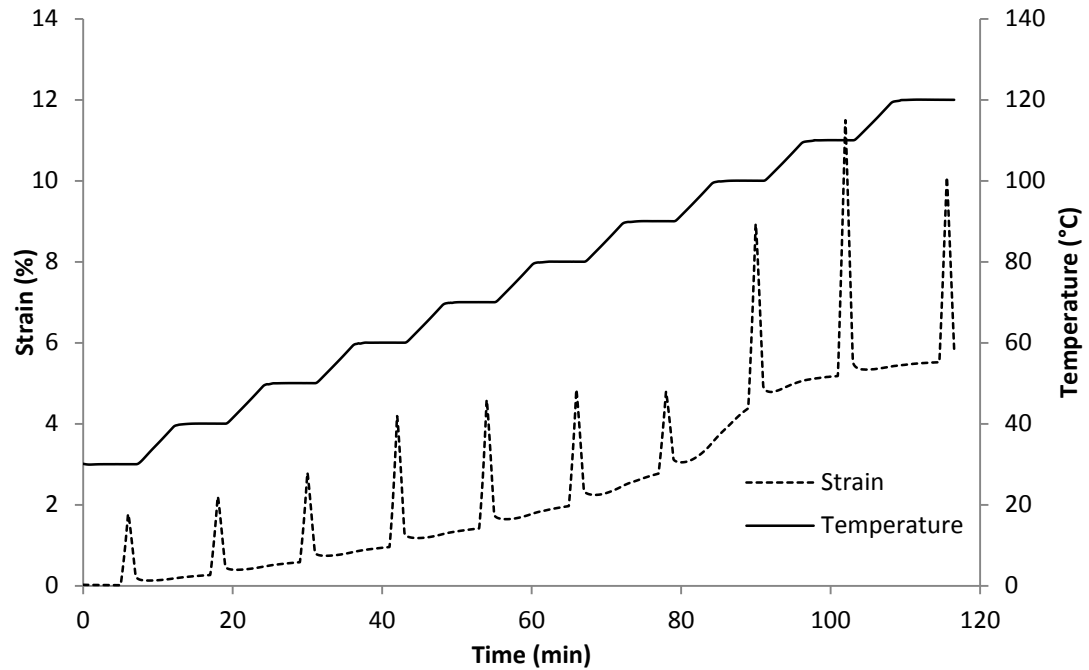


Figure 4.7 Tensile tests were performed at a number of temperatures. This graph shows the applied loading conditions. The temperature was increased then left to come to equilibrium. Then a stress/strain test was conducted at relatively small strains to determine the Young's modulus. The strain rate used was 2%/min.

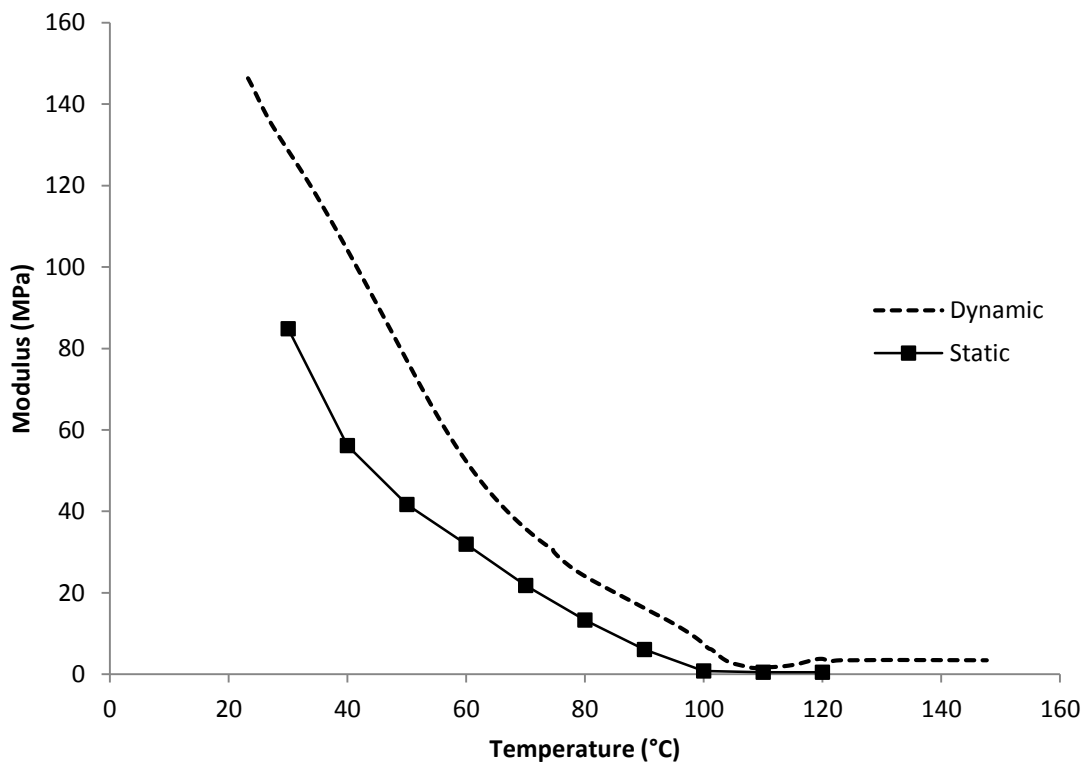


Figure 4.8 Comparison of static and dynamic test results. The static test results are from Figure 4.7 and the dynamic test results are from Figure 4.1.

The static and dynamic results show a substantial difference this may be due to the samples being at different temperatures because of the temperature of the sample in the dynamic test lagging behind the temperature of the chamber.

Dogbone samples were created using a sample cutter to cut samples for loading in the circumferential direction. The samples were then shrunk and tested. These samples showed a much greater repeatability than the rectangular samples when stretched to high strains. Figure 4.9 below shows 6 samples tested to large strains (>150% at centre).

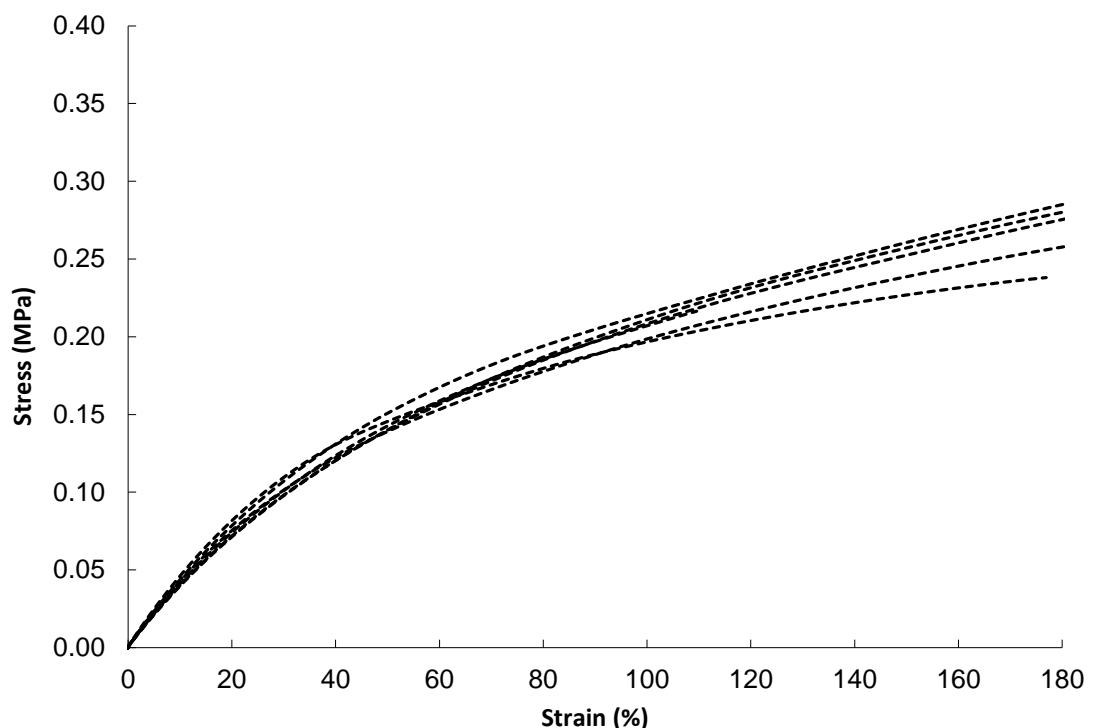


Figure 4.9 Comparison of stress/strain curves for 6 rectangular samples.

The greater repeatability of the dogbone samples is demonstrated in Figure 4.10 and Figure 4.11 below. In Figure 4.10 the force is plotted as a function of length change for 6 dogbone samples and in Figure 4.11 the same data is plotted as stress as a function of strain. The stress/strain curves vary more than the force/length change curves because the strain is calculated from the distance between the clamps and this distance varied slightly for each test. Ideally the strain would be measured by video extensometry measuring the strain at the narrow part of the dogbone sample but this was not possible in the DMTA and also the strain in the wide parts of the dogbone sample is significant.

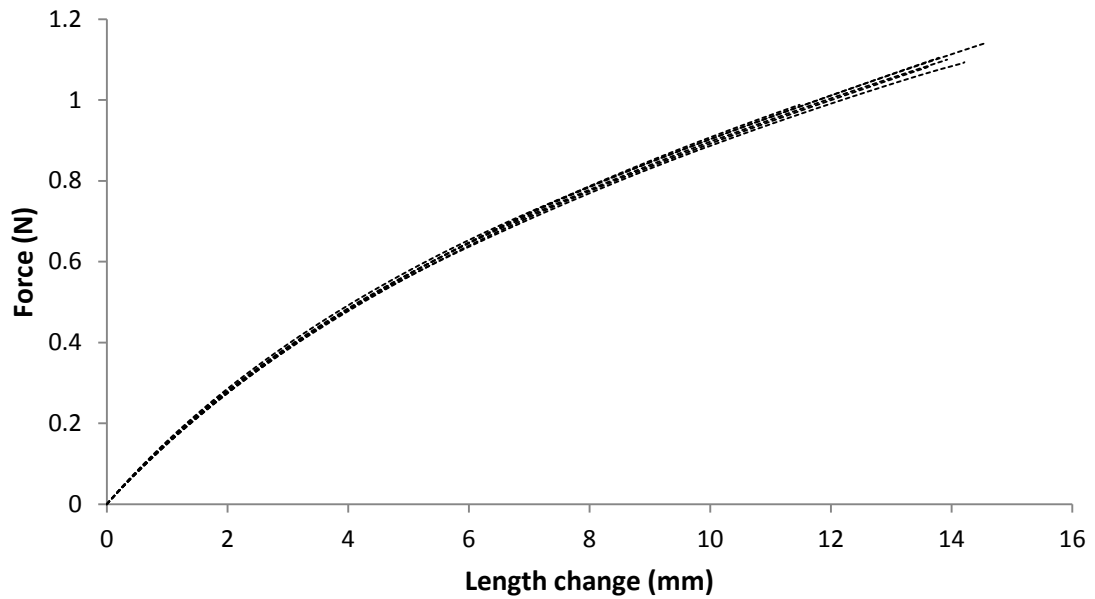


Figure 4.10 Force as a function of the change in length for 6 dogbone samples. Original sample length was 7.9 mm.

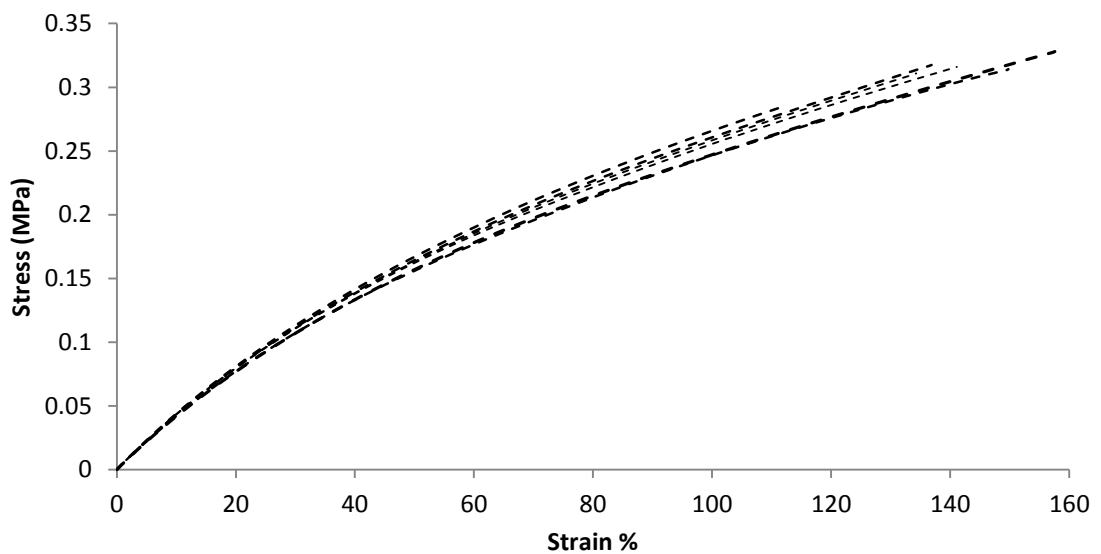


Figure 4.11 Same data as above but converted to stress as a function of strain. Strain calculated using distance between clamps as original sample length. This causes the increase in variation.

In order to use this data to create a material model for the heat-shrink tubing, a finite-element model of the dogbone tensile test was created. The set-up of the model is shown below in Figure 4.12. The test was modelled in 3-D using the same dimensions used in the experimental tests. A Neo-Hookean hyperelastic model (see Equation 2.6) was used to model the heat-shrink tubing and the stiffness was adjusted until the model data matched the experimental data. Figure 4.13 is a comparison of the force as a function of length change for the model and experimental data and it shows good agreement. The results are plotted

as force as a function of length change because the strain varies significantly over the sample and is much higher at centre as shown in Figure 4.12.

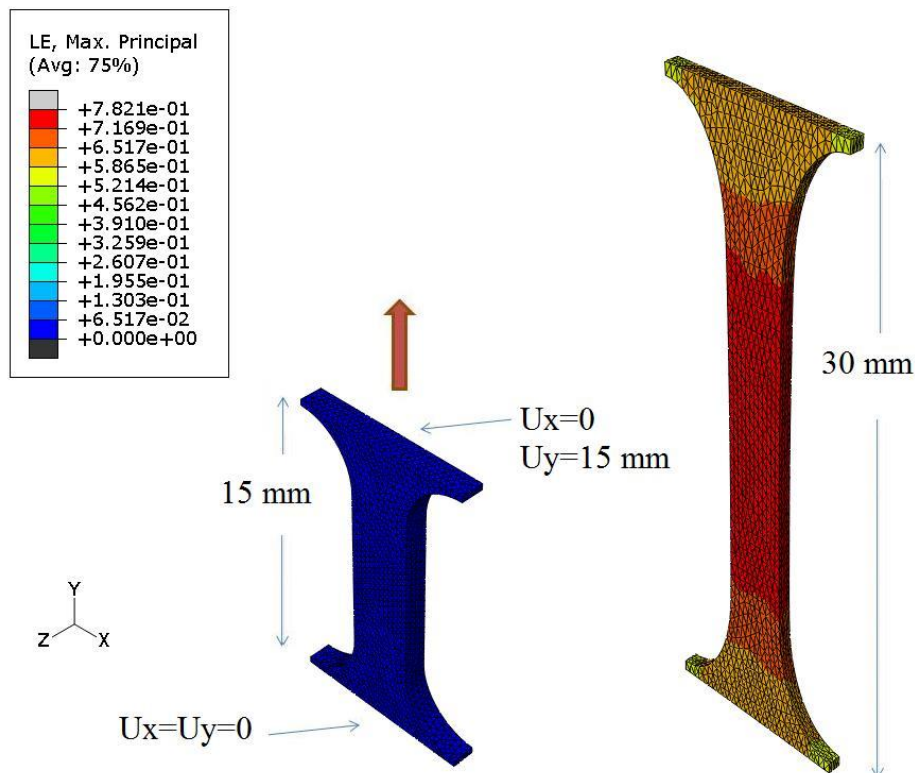


Figure 4.12 Finite element model of tensile test of dogbone heat-shrink sample. A Neo-Hookean model was used and the stiffness was adjusted to match the experimental data.

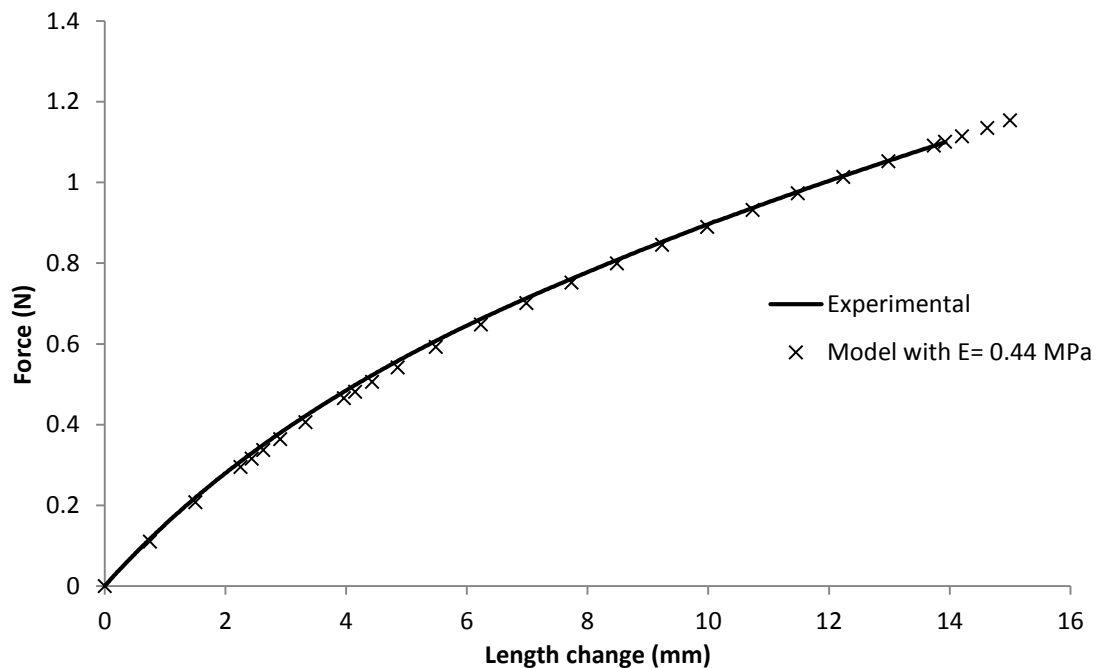
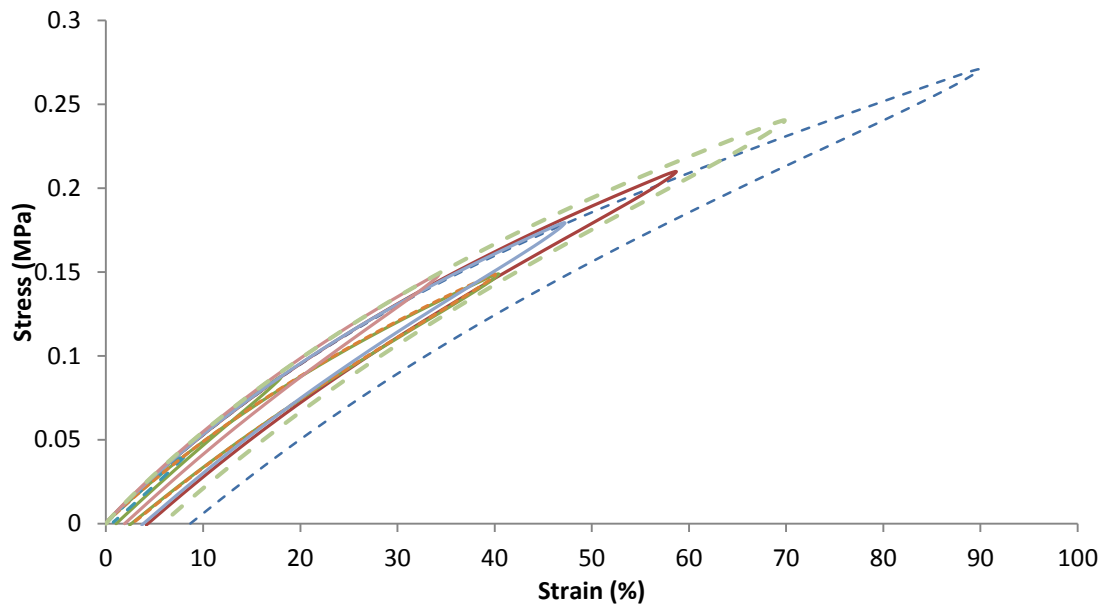


Figure 4.12 Force as a function of length change for tensile test on large heat-shrink test samples. Comparison of experimental tests with FE model of test. The Neo-Hookean hyperelastic model was used to model the heat-shrink tubing.

These tests show that the stress/strain behaviour of the large heat-shrink tube (at 120°C and in the circumferential direction) can be accurately modelled using an incompressible Neo-Hookean model with a Young's modulus of 0.44 MPa. Young's modulus is converted to shear modulus for use in Equation 2.6.

The plasticity of the material at large levels of deformation was investigated (Figure 4.13) by stretching a number of samples to various strain levels, as described in section 3.2.4.



**Figure 4.13** Graph showing loading and unloading of heat-shrink to large deformations. In these tests the force is ramped at 0.5 N/min and strain is calculated from distance between clamps.

From this graph it can be seen that there is a relatively small amount of plasticity in the material even when stretched to large strains. To quantify the plasticity the non-recoverable strain was plotted as a function of the maximum strain (Figure 4.14).

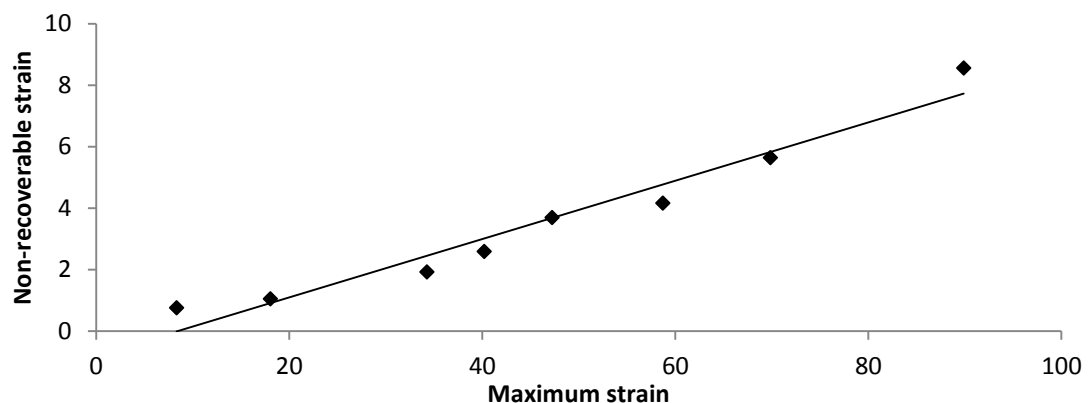


**Figure 4.14** Graph of non-recoverable strain as a function of maximum strain. Same data as Figure 4.13.

From Figure 4.14 it can be seen that there is no clear yield point for this material below 90% strain. The non-recoverable strain is approximately 7-9% of the maximum strain.

#### 4.1.5 Axial tests

A small number of tests were performed in the axial direction. It was not possible to create dogbone samples in the axial direction and so the tests were only performed to relatively low strains. A small number of tests were also performed on the small size heat-shrink tubing. Figure 4.15 below shows a comparison of the stress-strain curves for the large and small tubes. Both samples were rectangular in shape and oriented in the axial direction.

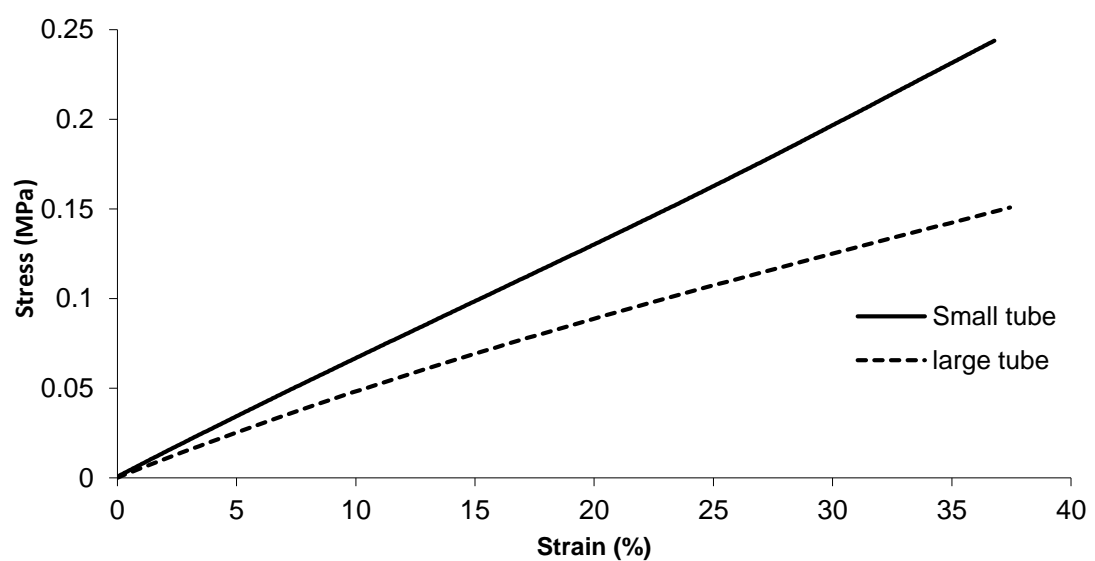
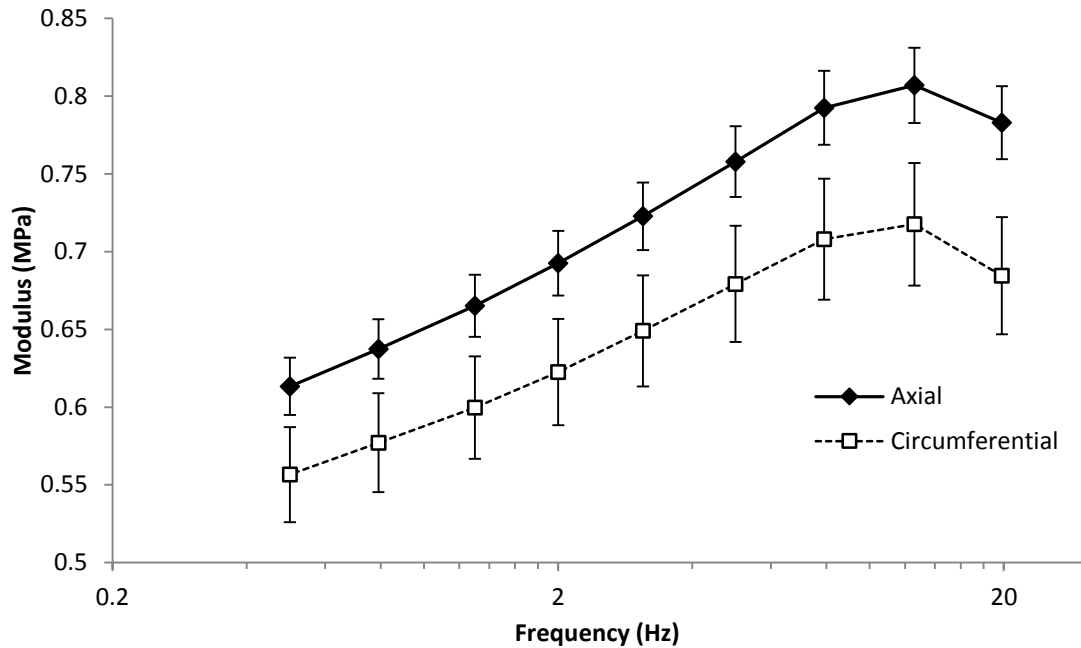


Figure 4.15 Comparison of stress versus strain curves for small and large heat-shrink tubing. Tests were performed in the axial direction at 120°C.

This graph indicates there is a significant difference between the modulus of the small and large tubes. According to this limited data, the modulus of the small tube is 55% larger than the modulus of the large tube. The modulus was calculated from the slope of the two curves in Figure 4.15.

#### 4.1.5 Anisotropy

The level of anisotropy in the heat-shrink was quantified by measuring the modulus in the axial and circumferential directions. The modulus was measured in the DMTA using the frequency sweep described in section 3.2.1. The results of these tests are shown below in Figure 4.16.



**Figure 4.16** Comparison of dynamic modulus in axial and circumferential directions. Results are an average of 5 samples. The error bars are  $\pm$  the standard deviation.

On average the modulus in the axial direction is approximately 11% higher than the modulus in the circumferential direction. The tube is stiffer in the axial direction because the extrusion process causes the polymer chains to align in the axial direction.

## 4.2 Recovery force

As described earlier, the heat-shrink tubing recovers to its original shape when heated. If the material is held at constant strain then the heat-shrink generates a recovery force. This recovery force is used to apply a pressure to the catheter assembly during welding. Modelling this recovery force is a key part of creating a computational model of the laser bonding process.

Many tests have been performed on the recovery force of the large heat-shrink tubing as described in section 3.2.7. Figure 4.17 below shows that these tests are quite repeatable. In these tests a small tensile strain of 0.1% was applied and the force required to maintain the strain as the sample is heated was measured. This is the reason for the small positive stress observed at low temperature. As the temperature increases, the force required initially decreases and becomes negative (compressive) due to the thermal expansion of the sample. As the material is heated to approximately 55°C, the crystalline phase begins to melt and the

sample begins to recover. Above approximately 55°C the tensile stress due to the shape memory effect exceeds the thermal stress and the force required to keep the strain constant becomes positive (tensile). The modulus decreases significantly with temperature and this reduces the stress in the material. The bump in the curve around 100°C is not understood but probably due to the processing conditions when creating the shape memory effect.

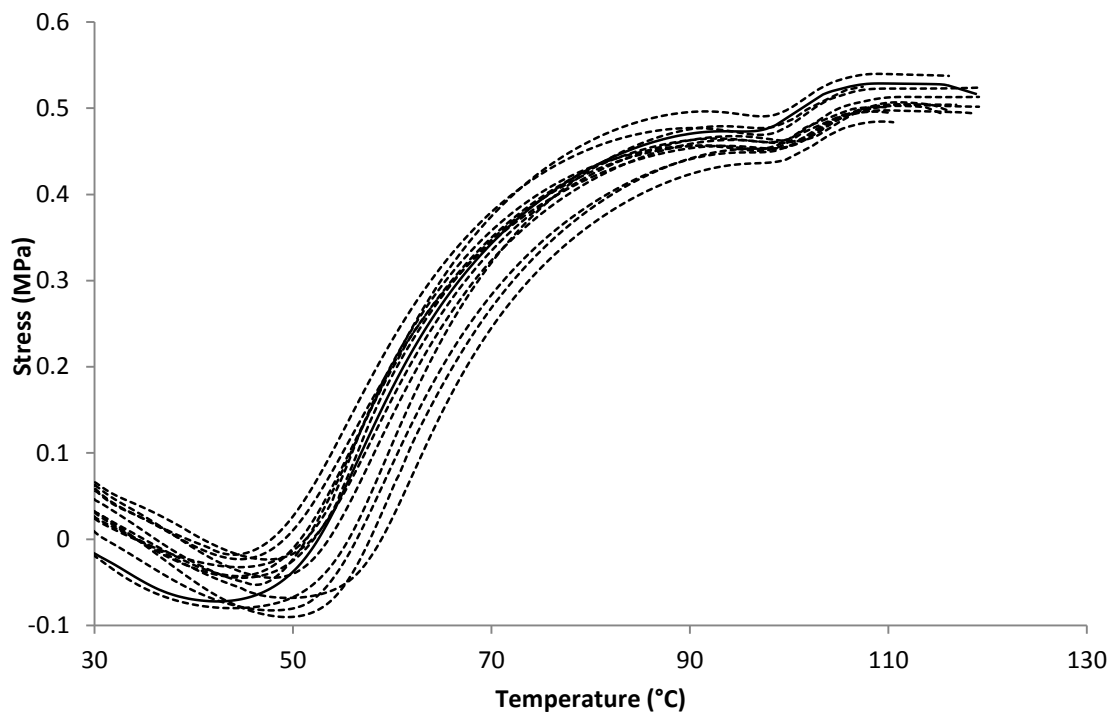


**Figure 4.17** Stress as a function of temperature for 13 samples of the large diameter heat-shrink tubing. In these tests the strain was kept constant at 0.1% while the temperature was ramped at 2°C/min.

Heat-shrink that had been shrunk was heated, stretched and cooled to create “Re-expanded heat-shrink”. Samples with different strains were created and tested to see how much of the forming force was recovered. The recovery force graphs of these samples are shown below in Figure 4.18.

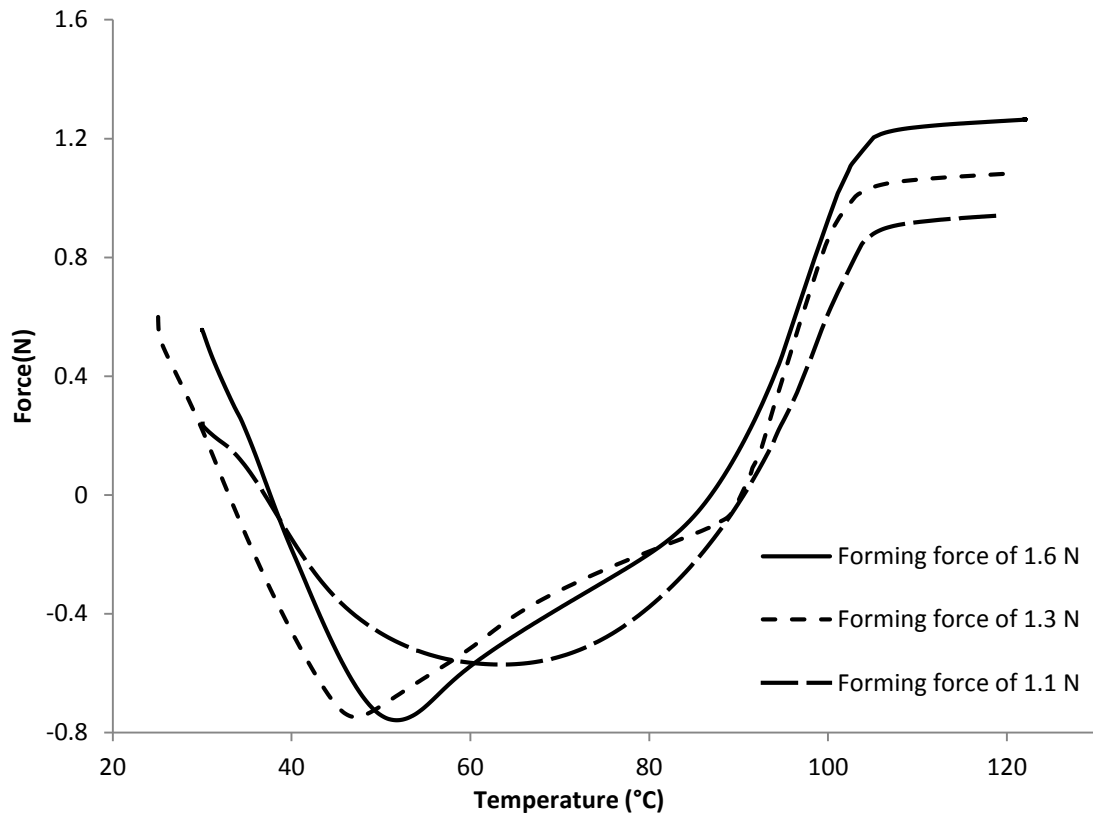


Figure 4.18 Recovery force of re-expanded heat-shrink as a function of forming force.

These graphs show that not all of the force needed to form the samples is recovered during reheating. This is thought to be primarily due to plasticity in the material but stress relaxation may also have an effect on the recovered force. The recovered force is approximately 80% of the forming force, however, these results showed significant variation from test to test.

## 4.3 Viscoelastic properties

### 4.3.1 Stress relaxation

Stress relaxation experiments were performed as described in section 3.2.8. In this test a sample is held at a constant strain in the DMTA at 120°C and the stress is measured over 10 mins. The results are shown below in Figure 4.19.

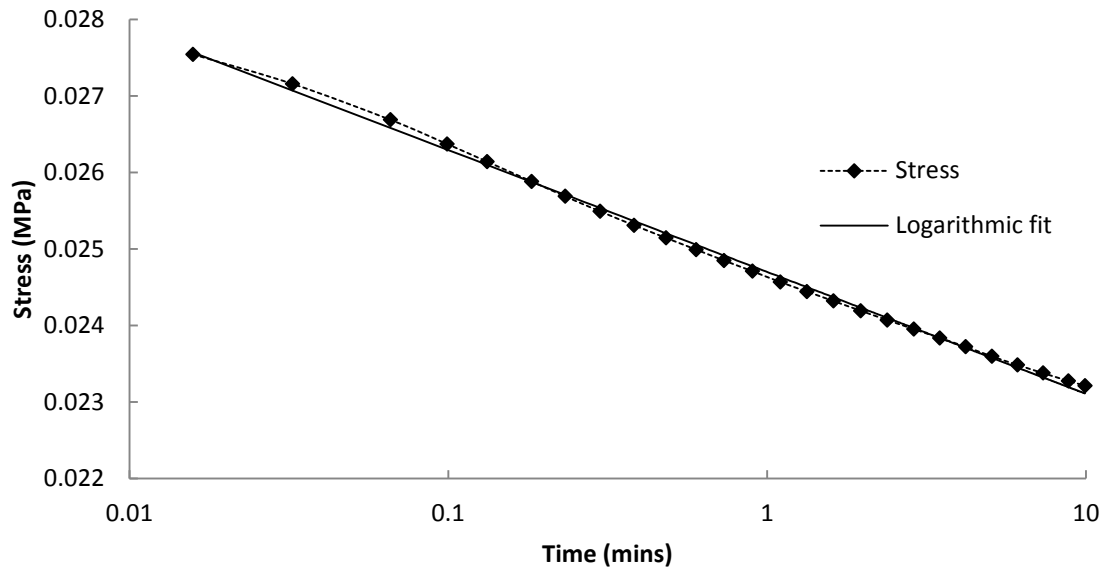
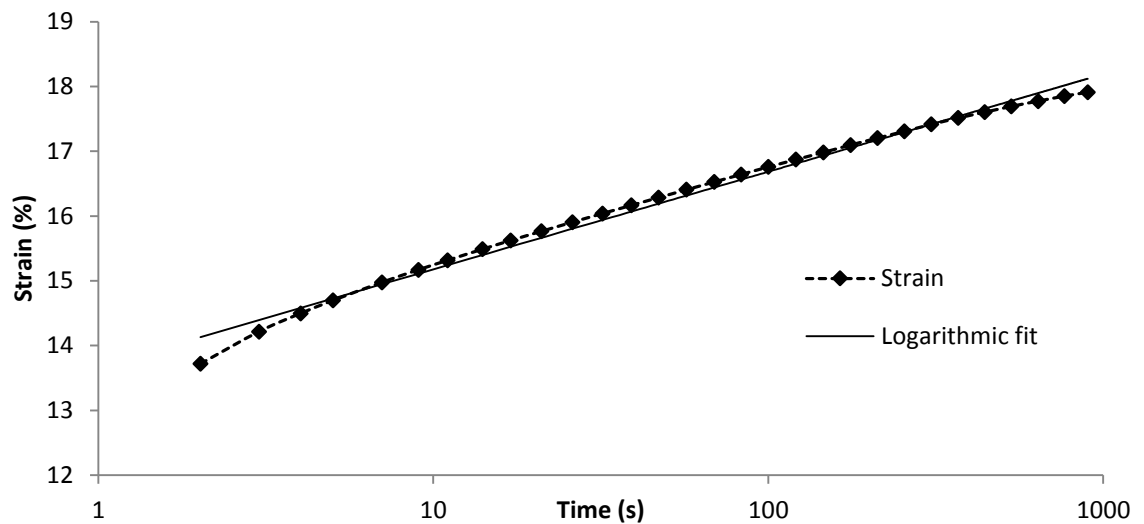


Figure 4.19 Stress relaxation of heat-shrink tubing at 120°C with a strain of 5%.

From Figure 4.19 it can be seen that the stress decreases logarithmically with time. Overall, the stress relaxation over the 10 minutes accounted for approximately 17% of the overall stress. It should be recognised that in the welding process, the heat-shrink material recovers its strain over 20 seconds at temperatures above 120°C, so it is therefore estimated that the drop in stress over this time period is on the order of 10%.

### 4.3.2 Creep

In these tests the DMTA was used to apply a constant load to the material and monitor the change in strain with time. A constant stress of 0.05 MPa was applied and dogbone samples were used. The change in strain is shown below in Figure 4.20.



**Figure 4.20** Creep test showing strain increasing logarithmically. Dogbone samples used and result is an average of 3 tests.

After 2 seconds the strain is approximately 14%. The strain then increases by 25% over 20 minutes in an approximately logarithmic fashion. It is estimated that for a constant stress over time periods relevant to the welding process, the increase in strain of the material is approximately 10%.

#### 4.4 Thermal expansion coefficient

The thermal expansion coefficient of the heat-shrink,  $\alpha$ , was determined by placing a sample in the DMTA and applying a small constant load as described in section 3.3.1.3. The temperature was then ramped up to 120°C very slowly (1°C/min) and the displacement monitored. The slow heating rate was chosen to see how alpha changes during heating. It can be seen that there is a large increase in length between 60 and 80°C.

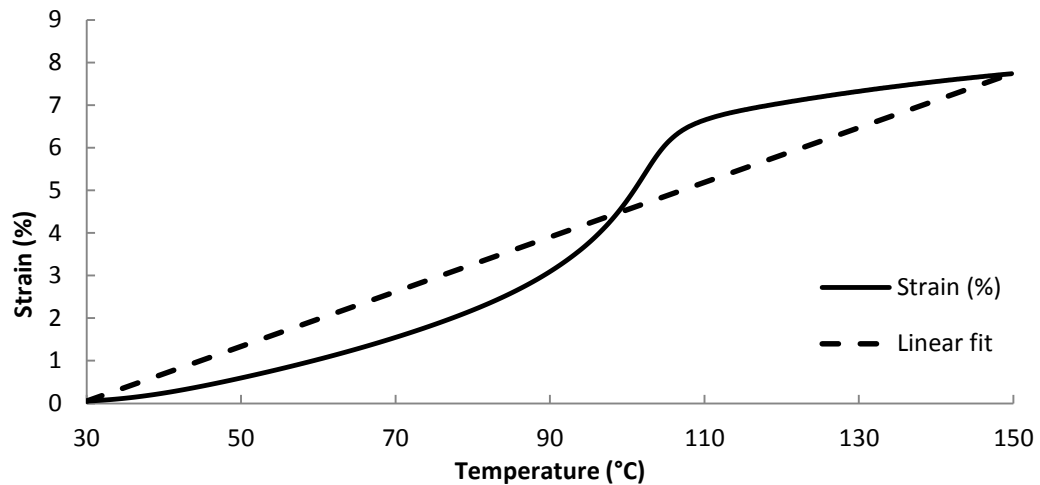


Figure 4.21 Strain as a function of temperature with slow heating rate (1°C/min) showing variation of  $\alpha$  at different temperatures.

The thermal expansion coefficient varies significantly during heating however, for the purpose of calculating a single value it is assumed to be constant and this linear fit is shown in Figure 4.21. The maximum difference between the linear fit and the experimental strain is approximately 1% and because the strain level that occurs in the welding process is approximately 100%, it was determined that the error introduced by this approximation was small. The average thermal expansion coefficient over the range of 30°C to 120°C is  $6.4 \times 10^{-4} / ^\circ\text{C}$ .

## 4.5 Hanger test

The hanger test was performed by engineers in Boston Scientific and is described in section 3.5. Short samples (2 mm) of heat-shrink tubing with internal diameter of 2 mm were placed on hangers in the DMTA and the position of the hangers was kept constant while the temperature in the chamber was increased to 150°C. As the heat-shrink contracts the force it applies to the hanger is measured by the DMTA. This test was repeated with different distances between the hangers. The results are shown below in Figure 4.22 and it can be seen that the shrink force is approximately proportional to the hanger outside diameter (OD) over quite a large range.

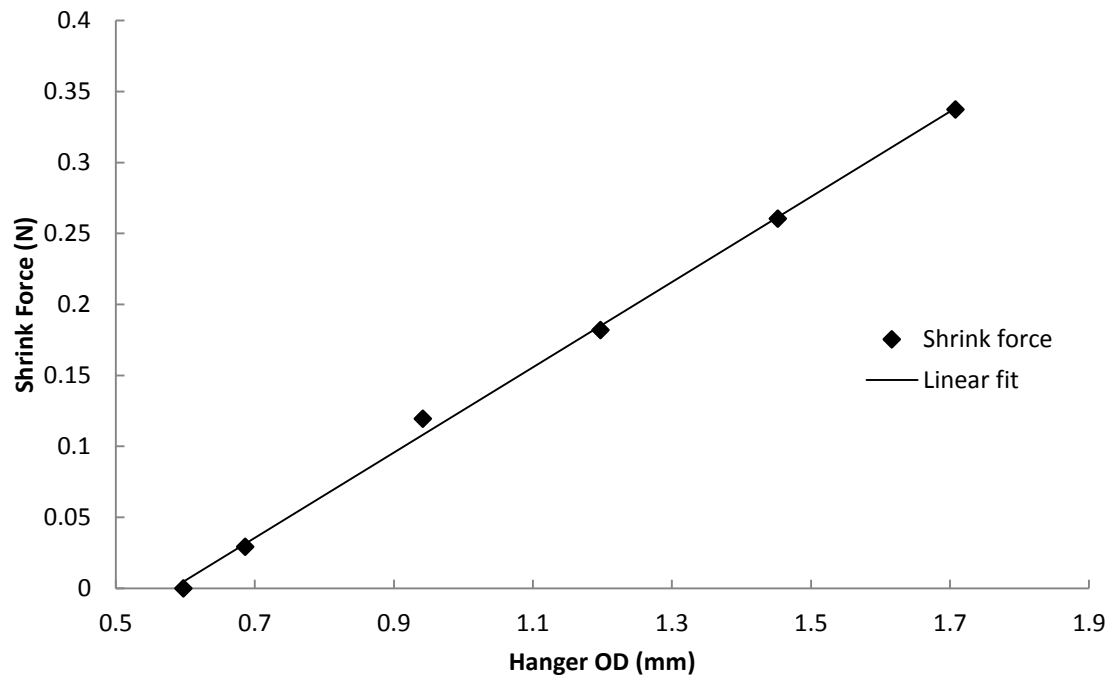


Figure 4.22 Test performed by Boston Scientific showing linear relationship between force and hanger OD.

This graph shows that the outer diameter of the hangers needs to be measured very accurately for this test. For example, if an outer diameter of 1 mm is used then an error of 0.02 mm would cause a 5% error in shrink force. This effect becomes smaller as the hanger outer diameter increases and so a larger hanger OD should be used if possible.

## 4.6 Pressure test

The shrink force of the small heat-shrink tube was also measured using a pressure test as described in section 3.6. In these tests a heat-shrink tube is filled with oil and then immersed in oil at 120°C, while the pressure inside the tube is measured.

The first test performed was a leak test to ensure the seal between the tube and pressure sensor was not leaking (also described in 3.6). The leak test involved placing a weight on the sealed tube and measuring the pressure of the oil inside the tube. If there was a leak the pressure would be expected to decrease. The results of the leak test are shown below in Figure 4.23.

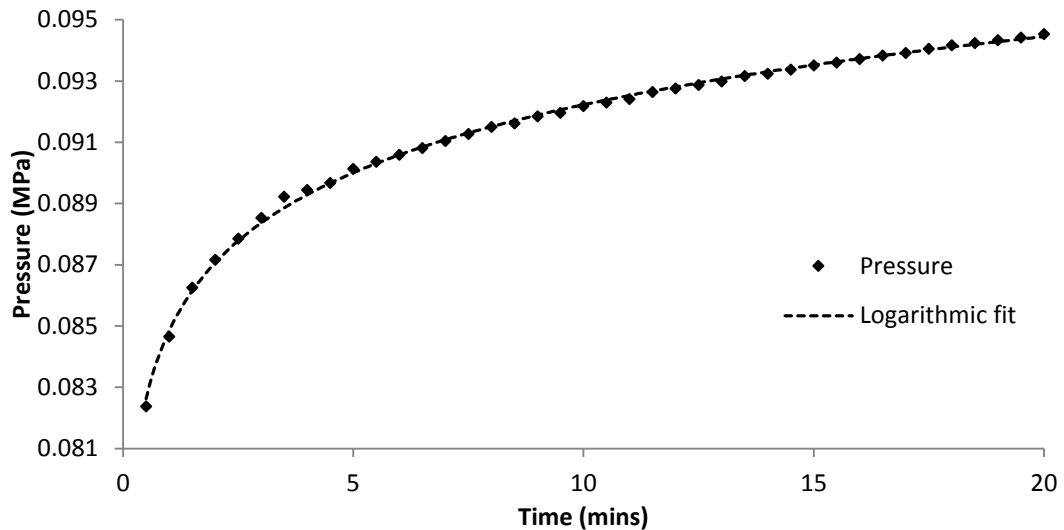


Figure 4.23 Results of leak test showing increase in pressure with time. This test was performed at 20°C.

As the pressure in the tube does not decrease during the 20 min test it was assumed that the seal was not leaking. The pressure increases by approximately 14% over 20 minutes during this test. This increase is thought to be due to stress relaxation in the wall of the heat-shrink tubing. As the weight is being supported by the elasticity of the tube and the pressure of the oil, any stress relaxation in the tube will cause an increase in oil pressure.

The results of a pressure test are shown below in Figure 4.24. During the tests the pressure reaches a maximum within a few seconds and then begins to drop off.

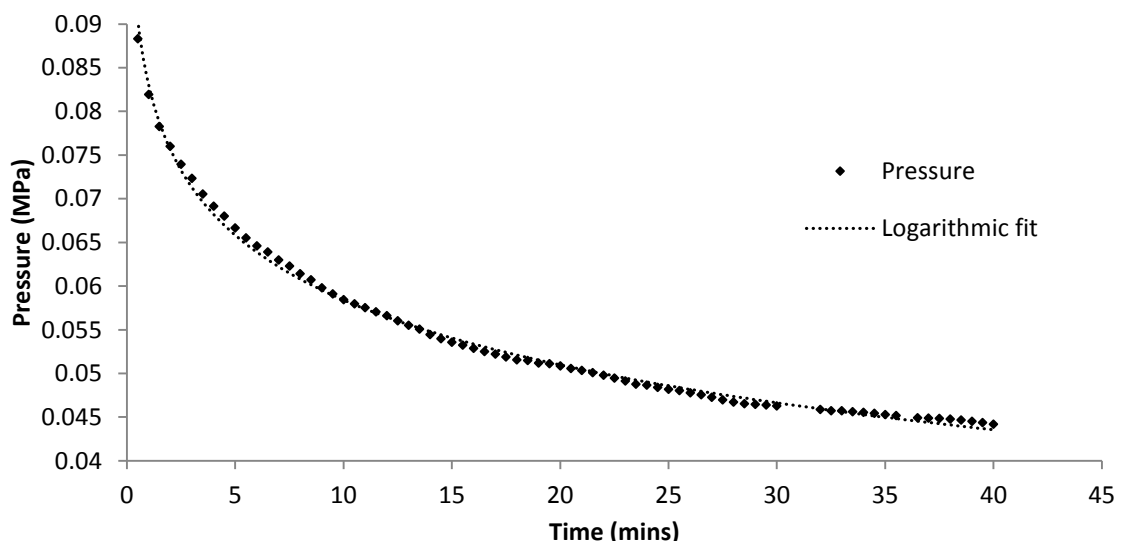


Figure 4.24 Variation of pressure with time for pressure test. At  $t = 0$  the heat-shrink tube was immersed in oil at 120°C at the pressure inside the tube was recorded every 30 s for 40 minutes.

The pressure drops by 50% over 40 minutes. After 10 minutes the pressure has dropped by 34%. When this is compared with the results of the uniaxial stress relaxation experiment in

Figure 4.19, it can be seen that the pressure in the pressure test drops significantly faster than the stress in the stress relaxation experiment. This is due to the fact that in the stress relaxation experiment, the stress relaxation occurs in one dimension (circumferential), whereas in the pressure test the stress relaxation occurs in three dimensions (circumferential, axial and radial). Creep may also play a role in this pressure drop.

Five different grades of the small heat-shrink tubing were tested. The five tubes had approximately the same dimensions but produced significantly different shrink forces when measured on the hanger test. The shrink force value of the tube depends on the elastic modulus at high temperatures. The modulus of the tube is determined by the amount of cross-linking which in turn is determined by the amount of irradiation the material received when being produced [84]. The five different tubes tested were exposed to five different levels of irradiation and therefore produce different elastic moduli at high temperature.

Figure 4.25 below shows the results of the pressure test on the five different heat-shrink grades. The pressure plotted is the maximum pressure of the oil in the heat-shrink tubing which occurs immediately after being immersed in the hot oil bath. At least five different samples were used for each heat-shrink grade. The error bars show the range which all samples fell within.

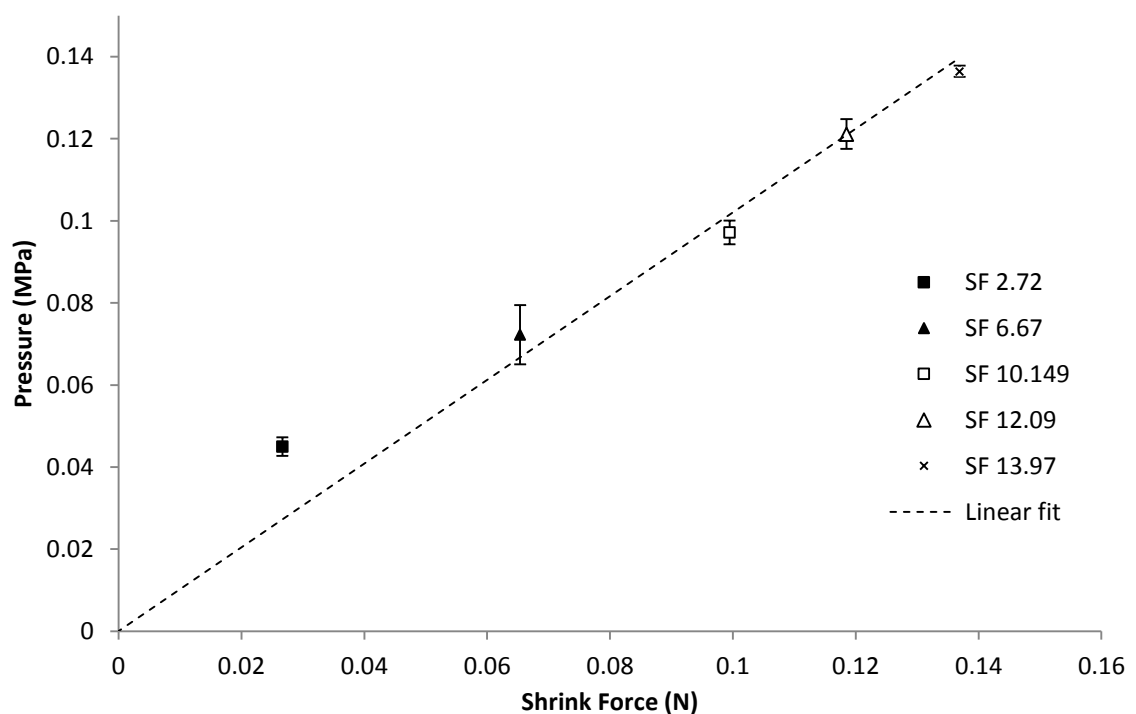


Figure 4.25 Maximum pressure of the oil during pressure test plotted against shrink force values provided by Boston Scientific. The error bars show the range all samples fell within. The linear fit shown has been set to go through the origin.

The pressure produced by the heat-shrink during the pressure test is approximately linearly proportional to the shrink force measured with the hanger test. This is expected as the samples have the same dimensions and the only difference between the samples is the modulus. The linear fit shown in Figure 4.25 has been set to go through the origin as it is assumed that as the shrink force goes to zero the pressure would also go to zero.

#### 4.7 Determination of modulus of small heat-shrink tubes

To calculate the modulus of the different tubes an FE model of the pressure test was created. The FE model consisted of an axisymmetric model of an incompressible Neo-Hookean hyperelastic tube (see Equation 2.6). The initial dimensions of the tube were those of a fully recovered heat-shrink tube. An arbitrary modulus (1 MPa) was assumed initially and a pressure load was applied to the tube to cause it to expand. Using an iteration process, the pressure was varied until the dimensions of the tube after stretching matched those of the as-received heat-shrink. This pressure was then recorded. As the pressure produced by an elastic tube is linearly proportional the modulus, as shown in Equation 3.4, the ratio of the pressure from the FE model to pressure from experimental pressure test is equal to the ratio of the assumed modulus to the actual modulus of heat-shrink tubing used in the pressure test. Using this process the modulus of the five tubes was calculated and the results are shown in Table 4.1.

Results from pressure test		
SF (g)	P (MPa)	E (MPa)
2.72	0.045	0.208
6.67	0.072	0.339
10.15	0.097	0.443
12.07	0.121	0.537
13.97	0.136	0.613

Table 4.1 Modulus values calculated from pressure test for the 5 different grades of heat-shrink

## 4.8 Determination of the frozen fraction

Two methods were used to calculate the frozen fraction, one using the DSC as described in Section 3.2.6 and the other was using an approximation of the free strain recovery used by Liu *et al.*, also described in Section 3.2.6. The DSC method was used to try to connect the frozen fraction to a physical parameter, namely the crystallinity. However using the frozen fraction calculated from this method in the simulation of the recovery stress (see section 3.2.7) produced a result which did not agree well with the experimentally observed recovery stress. Therefore the Liu *et al.* model of fitting a curve to the free strain recovery curve was used and the results are shown below in Figure 4.26.

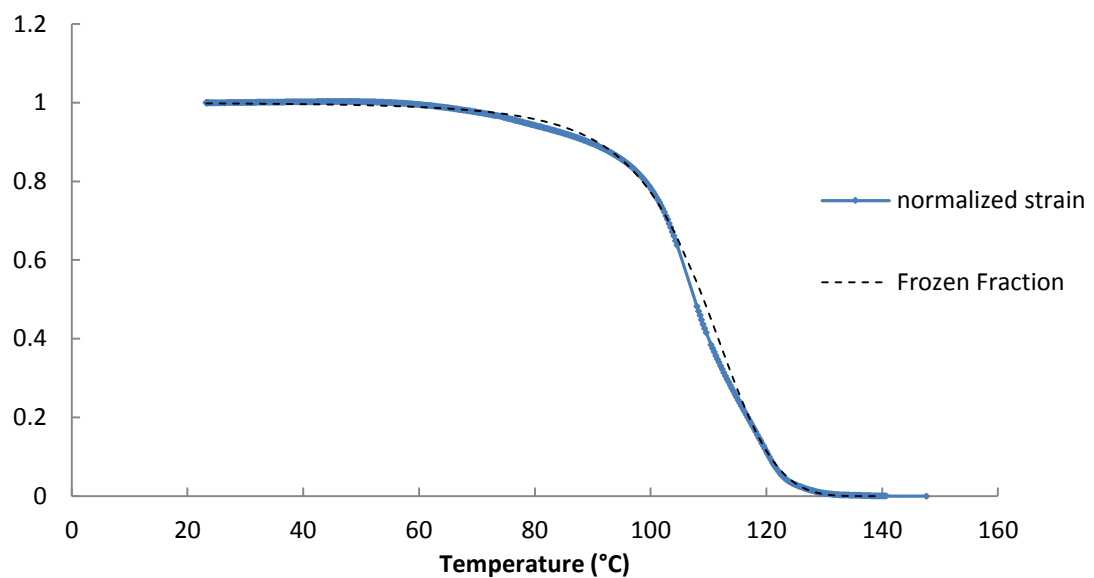


Figure 4.26. Normalized free strain recovery as a function of temperature. The frozen fraction curve was fitted to the strain curve.

## 4.9 Discussion

In this chapter the results of the experimental characterisation of the heat-shrink tubing have been presented. The majority of the testing was done using a large size heat-shrink tube in the DMTA as the tube used in the welding process was difficult to test due to its small size. The only test performed on the small size tube was a pressure test which measured the pressure applied by the small tube when heated.

The modulus of the heat-shrink and the parameters which affect it were investigated. The parameter with the largest effect on the modulus was the temperature. Heating the heat-

shrink from 20°C to 120°C causes the modulus to drop by a factor of 100. However, further heating has a relatively small effect as shown in Figure 4.4.

The viscoelastic properties were investigated by measuring the modulus in a dynamic test at different frequencies and also by performing stress relaxation and creep tests. It was found that the modulus is dependent on frequency but over the range of values relevant to the welding process the effect was quite small. The stress relaxation causes a drop in stress of approximately 10% over the relevant time period (20 s). Due to these results, it was decided that viscoelasticity could be left out of the heat-shrink model as a reasonable approximation.

Tensile tests were performed on the large-size heat-shrink using large strains (> 100%). A hyperelastic model was fitted to the resulting stress/strain curve and it was found that the Neo-Hookean model produced a very good fit.

The anisotropy was quantified by measuring the modulus in the circumferential and axial directions. The axial modulus is approximately 10% larger than the circumferential modulus but this difference was deemed small enough to be left out of the heat-shrink model. The circumferential direction is more relevant to the process so data from this direction was used to calibrate the model.

The elastic modulus of 5 different grades of small heat-shrink tube was calculated using data from the pressure test. These values are used in Chapter 6 to model the shrink force test. Due to the relatively small effects of viscoelasticity, plasticity and anisotropy it was decided that the SMP could be modelled using a Neo-Hookean hyperelastic SMP model with the modulus derived from the pressure test.

## 5 Thermal modelling of the laser welding of balloon catheters

The purpose of the thermal model is to predict the temperatures throughout the balloon catheter proximal joint assembly (shown in Figure 1.4) during the laser bonding process of the PE balloon to the catheter shaft. Obtaining an understanding of the thermal profile throughout the joint assembly is essential if the thermo-mechanical behaviour of the PE material during welding is to be analysed. Preliminary thermal modelling of the balloon catheter joint assembly was completed by engineers at Boston Scientific [93]. However, it was deemed necessary to validate this work in order to gain a full understanding of the thermal model and to be able to apply the thermal methods to different assembly geometries. The thermal model consists of two parts, modelling the laser absorption and modelling the heat flow through the assembly. These two aspects are discussed below in sections 5.1 and 5.2 respectively.

### 5.1 Laser thermal absorption

When modelling laser welding, the first thing to consider is the heat source and its representation within the model. The diagram below (Figure 5.1) shows the laser beam interacting with the assembly. The assembly is rotating at approximately 500 rpm so the heat generation calculated below is averaged circumferentially and assumed to be axi-symmetric. The incoming continuous laser radiation source is represented within the model by dividing it up into approximately 200 beams. Similarly, the cross section of the catheter assembly is divided into approximately 500 annuli. Each beam is tracked through the assembly and the volumetric heat source due to the absorption of the laser light,  $\dot{q}$ , is calculated by taking the magnitude of the derivative of Equation 2.1 with respect to depth,  $z$  [20].

$$\dot{q} = \alpha I_0 e^{-\alpha z}$$

The laser beam is refracted at the surface of the assembly due to the change in refractive index. The angle of refraction is calculated using Snell's law [90]:

$$n_1 \sin(\theta_1) = n_2 \sin(\theta_2) \quad (5.1)$$

where  $n_1$  is the refractive index of air,  $n_2$  is the refractive index of the heat-shrink,  $\theta_1$  is the angle between the ray and the surface normal outside the assembly and  $\theta_2$  is the angle between the ray and the surface normal inside the assembly. Reflection at the outer surface is accounted for using Fresnel's equation [91]:

$$I = I_0 \left[ 1 - \left( \frac{n_2 \cos \theta_1 - n_1 \cos \theta_2}{n_2 \cos \theta_1 + n_1 \cos \theta_2} \right)^2 \right] \quad (5.2)$$

Where  $I$  is the intensity of the light that is transmitted and  $I_0$  is the intensity of the incident beam of light.

Reflection and refraction between layers in the assembly is neglected in this model. Reflection and absorption of the laser by the mandrel is also neglected (i.e. all light which reaches the mandrel is assumed to be lost).

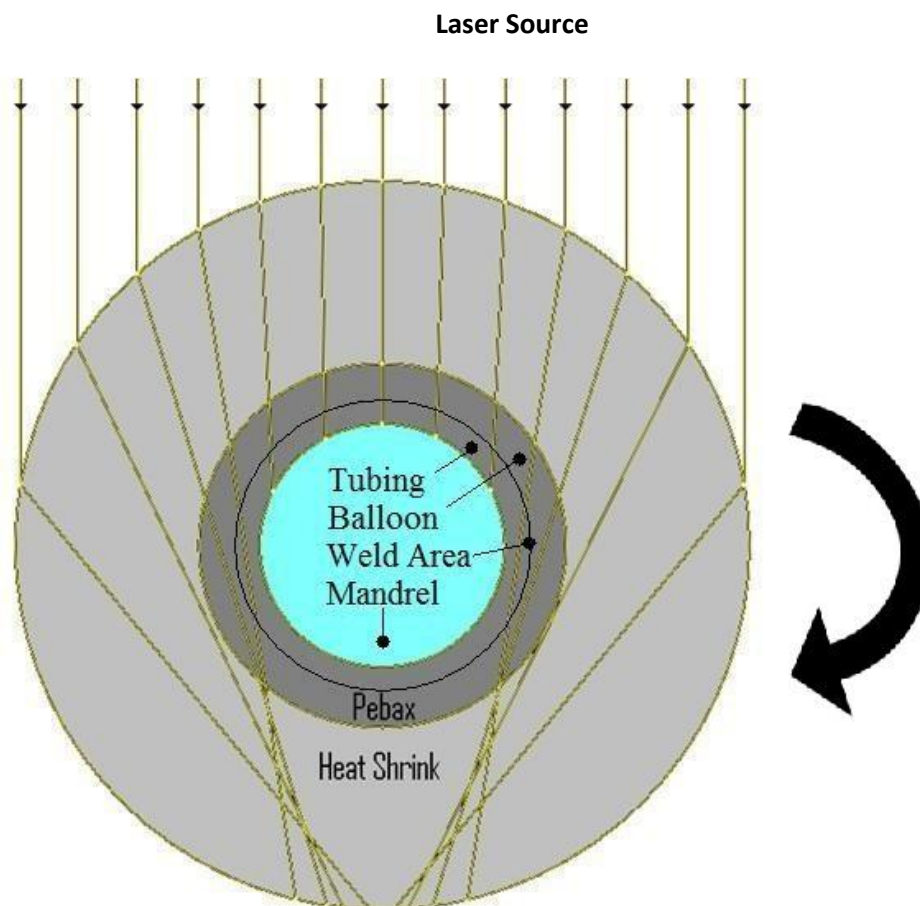


Figure 5.1 Laser interacting with the balloon catheter assembly shown in a cross sectional profile. The dark line between the tubing and the balloon represents the area to be welded. The assembly is rotated to get an even weld around the joint and the heat source is averaged circumferentially to account for this rotation.

This technique is known as ray tracing and the results of this are shown below in Figure 5.2. The results are compared with previous Boston Scientific work. The engineers in Boston Scientific used MATLAB to implement the ray tracing technique from first principles. They then used a commercial ray tracing software package called TRACEPRO to verify their work.

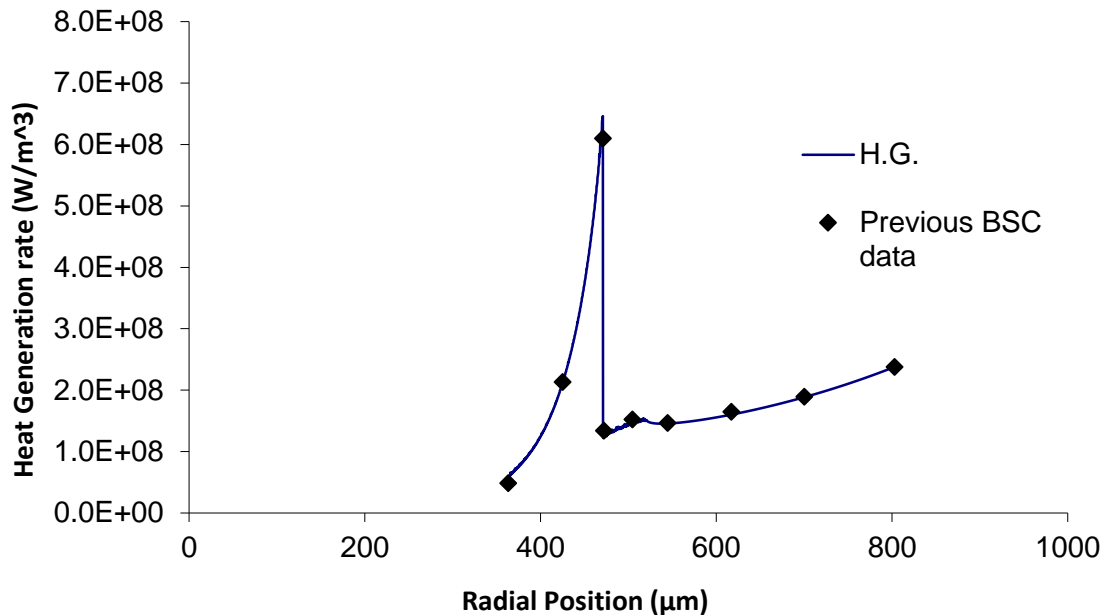


Figure 5.2 Graph of Heat generation as a function of radial distance from the centre of the assembly. The line labelled H.G. is the data obtained from the ray tracing technique while the data points represent results from previous work by Boston Scientific.

These results have been averaged around the circumference of the assembly to obtain an axisymmetric heat generation rate which takes into account the rotation of the assembly [94]. There is very good agreement between the results obtained from this ray tracing technique and the results of Boston Scientific. An equation was then fitted to this graph so that it could be included in a thermal model.

## 5.2 Heat transfer model

A transient thermal model was created in the commercial finite element code Abaqus FEA using the balloon catheter joint assembly geometry and the laser parameters used by Boston Scientific in the laser welding process. The model is assumed to be axisymmetric. The geometry is axisymmetric and the heat generation has been averaged circumferentially to provide an axisymmetric loading. Heat generation is calculated using laser thermal absorption data calculated using the ray-tracing method shown in Figure 5.2 above and the heat losses of free convection and radiation are implemented. Forced convection due to the

rotation of the balloon catheter joint assembly was neglected. It is worth noting that the mandrel conducts a large amount of heat away from the welded area due to the high thermal conductivity of stainless steel and the relatively long length of the mandrel (approx. 1 m). This is represented within the model. The entire assembly is represented as a single part, hence neglecting contact effects and air gaps between the assembly parts. This single part is then partitioned into different sections which are assigned the various material properties (see Table 5.1 below). It is noted that the conductivities of the PEBAX® and heat-shrink vary with temperature.

Material	Density (kg m <sup>-3</sup> )	Specific Heat Capacity (J kg <sup>-1</sup> K <sup>-1</sup> )	Conductivity (W m <sup>-1</sup> K <sup>-1</sup> )	T <sub>melt</sub> (°C)	Latent heat of fusion (J kg <sup>-1</sup> )	α (m <sup>-1</sup> )
PEBAX®	1020	2520	For T < T <sub>m</sub> =0.336-0.0012*T  For T > T <sub>m</sub> =0.1296	172	54428	18898
Stainless Steel	8000	500	16.2	-	-	-
Heat- shrink	1020	2200	For T < 100°C =0.35-0.0011*T  For T > 100°C =0.24	-	-	3543

**Table 5.1: List of material properties of the various materials used in the balloon catheter joint assembly.**

The total heat flux out of the surface of the assembly is the sum of the convective and radiative heat fluxes:

$$q = h(T_W - T_\infty) + \Omega\varepsilon(T_W^4 - T_\infty^4) \quad (5.3)$$

Where  $q$  is the total heat flux,  $h$  is the heat transfer coefficient,  $T_W$  is the surface temperature of the assembly,  $T_\infty$  is the external temperature,  $\varepsilon$  is the emissivity of the surface of the assembly and  $\Omega$  is the Stefan-Boltzmann constant [93]. The heat transfer coefficient was calculated from various empirical relationships over an appropriate range of the Rayleigh

number [95] and its' value was determined to be  $30 \text{ W/m}^2/\text{K}$ . Boston Scientific determine the value of the emissivity,  $\varepsilon$ , through available experimental data to be 0.95 [93].

The assembly represented within the finite element model is assumed to have an initial temperature of  $20^\circ\text{C}$ . The elements used were quadratic heat transfer elements and there were 775 elements in the model. The heat input was implemented using the subroutine HETVAL within the Abaqus FEA finite element code. This enables the creation of a spatially varying volumetric heat source. Figure 5.3 below shows the meshed assembly, the mesh is finer in the heated area because the thermal gradients are highest in this region. This mesh is quite coarse; however, good agreement with previous work performed by Boston Scientific [93] is achieved.

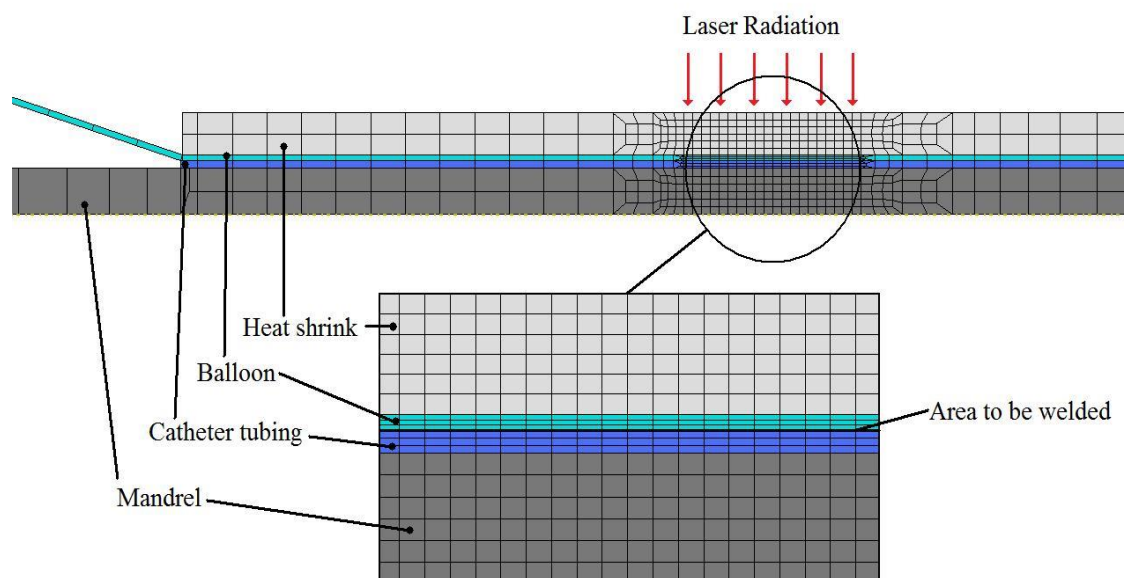


**Figure 5.3** The meshed geometry used to represent the balloon catheter joint assembly. The heat-shrink outer diameter is 1.6 mm. The mandrel radius is 0.36 mm. The outer thickness is 0.062 mm. The balloon waist thickness is 0.046 mm.

As in all modelling approaches, some assumptions have been made and some phenomena have been neglected. The effect of the air in the balloon heating up has been neglected. The mandrel is coated in Teflon to stop the PEBA<sup>®</sup> sticking to it. The effect of this Teflon coating on the thermal properties has also been neglected. The intensity of the laser beam is assumed to be uniform across the width of the beam which is 1.5 mm. It is also assumed that the laser absorption is independent of temperature. In addition, as this is a thermal model only, no material deformation and melt flow is represented within the model. This is examined in detail in Chapter 7.

Figure 5.4 below compares the surface temperature (after 20 s) prediction of the model with that of a Boston Scientific model. It can be seen that the models are in good agreement.

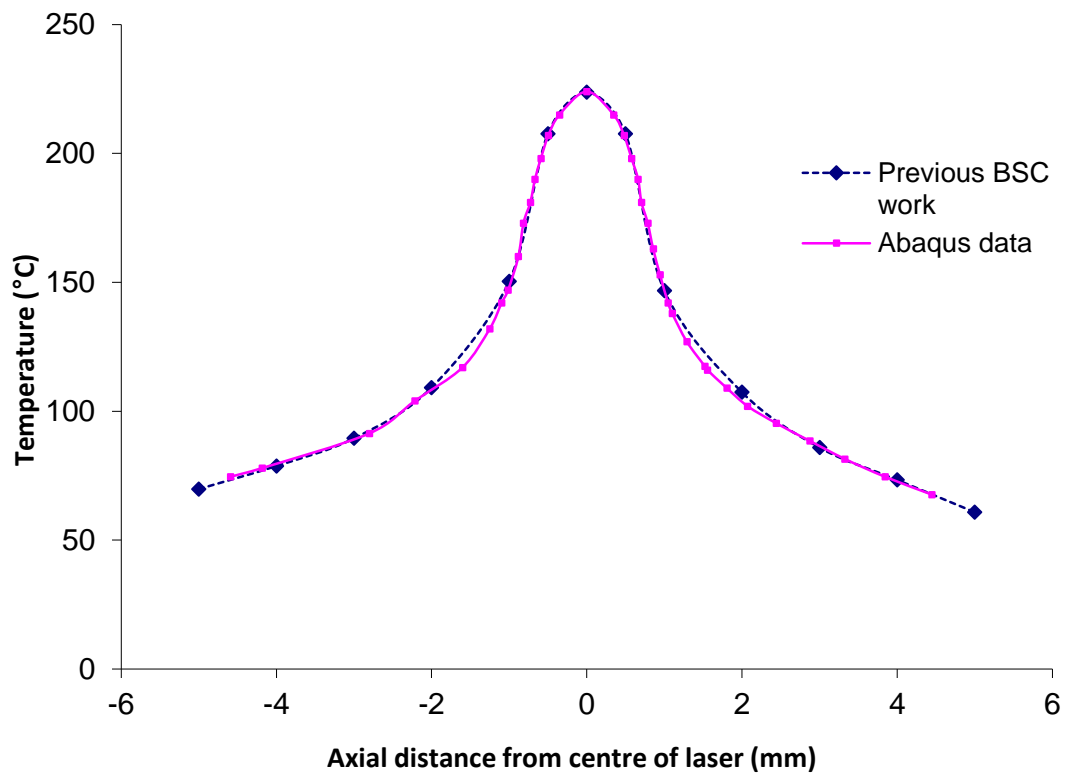


Figure 5.4 This graph shows the temperature variation along the surface of the heat-shrink.

Figure 5.5 shows how the temperature at the heat-shrink surface varies over time. Simulations were run using various time steps, the influence of changing from 20 time steps to 210 was quite small and any more time steps produce virtually no change.

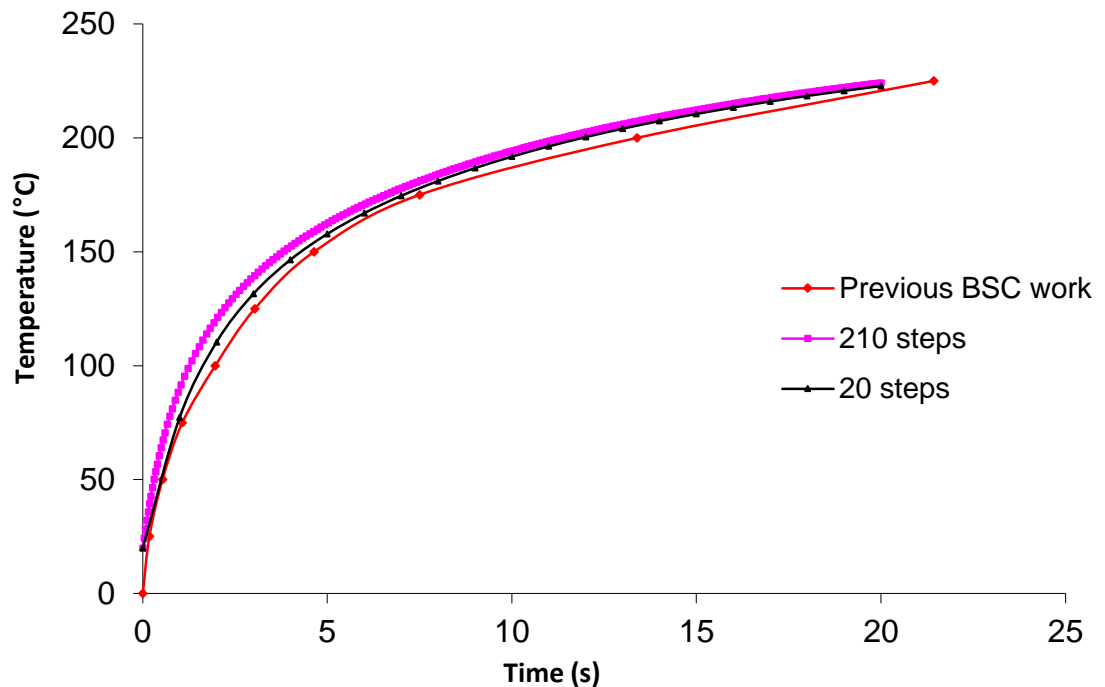


Figure 5.5 Variation of temperature of heat-shrink surface at centre of laser beam.

The results obtained from these simulations show that the temperatures are a little higher during the welding process than in the previous work. The difference between the results may be due to the time steps or the mesh density but is broadly in good agreement with previous work.

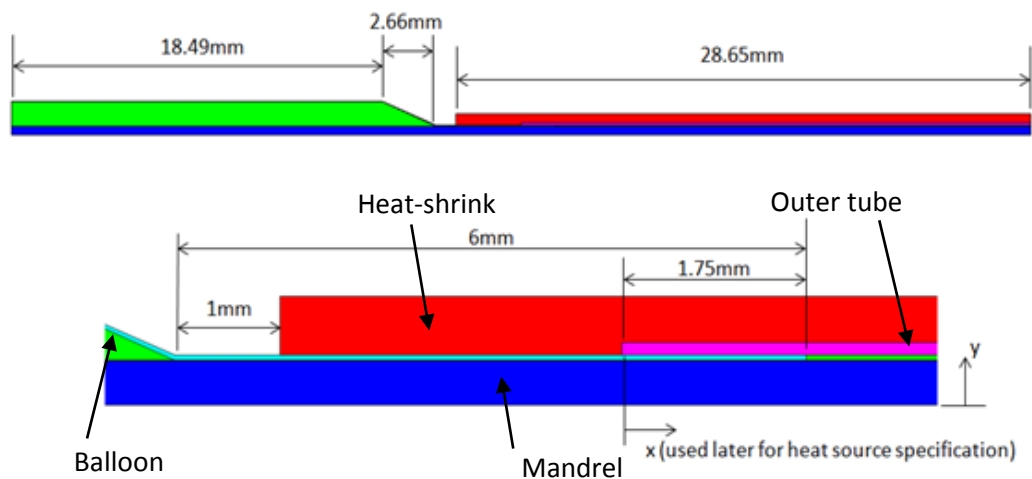
The engineers in Boston Scientific have compared their results to experiment by using polarized microscopy. This technique allows the shape of the melt region to be determined and this can be compared with the melt region predicted from the model. There is good agreement between the melt pool shape predicted by the Boston Scientific model and the melt pool region observed on a welded catheter so this model is compared against the Boston Scientific model and not directly with an experiment.

### 5.3 Modelling of the Sterling™ balloon catheter joint assembly

The Sterling™ balloon catheter is the catheter geometry examined in this work. More specifically, the proximal bond of a catheter with a 3 mm balloon is represented within the computational models of this work and in those of the thermo-mechanical investigation of Chapter 7. There are a number of differences between the thermal model of the Sterling™ catheter and the thermal model in Section 5.2 including a different geometry, a moving laser

and a temperature feedback to control the laser power. These differences and their effects are described here.

The first difference is the geometry. In the Sterling™ catheter, the balloon is inside the outer tube as shown in Figure 5.6 and there is an overlap of 1.75 mm. Also, the end of the outer tube is within the laser beam and this has to be taken into account when calculating the laser absorption. In the thermal model in Section 5.2 the heat generation by laser absorption is constant across the width of the laser beam but this is not the case for the Sterling™ model. The right-hand-side of the laser passes through the outer but the left-hand-side does not as shown in Figure 5.7. This results in two different heat generation curves, which are shown in Figure 5.8.



Mandrel radius: 400  $\mu\text{m}$   
 Teflon coating thickness: 6.35  $\mu\text{m}$   
 Balloon waist thickness: 46.4  $\mu\text{m}$   
 Balloon body wall thickness: 16  $\mu\text{m}$   
 Balloon body O.D.: 3.12 mm  
 Outer tube thickness: 114  $\mu\text{m}$   
 Heat-shrink O.D: 1967  $\mu\text{m}$

Figure 5.6 Representation of the model geometry for the Proximal joint assembly of the Sterling™ catheter.

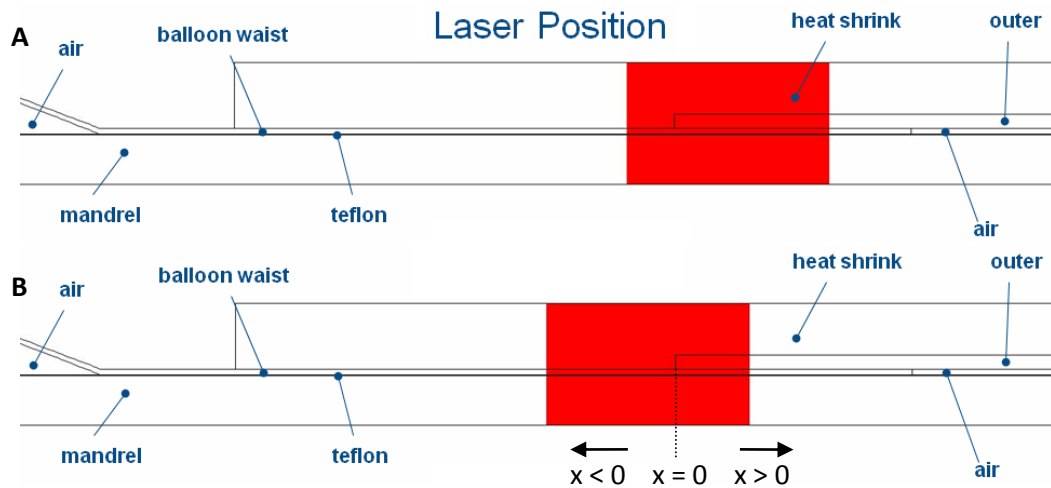


Figure 5.7(A-B) Movement of laser during welding. The laser is stationary for the first 10 seconds of the process in the position shown in A. It then moves 0.6 mm to the left over 8 seconds and finishes in the position shown in B.

Another difference with the Sterling™ catheter model and the previous model, discussed in Section 5.2, is that the laser is stationary in the previous model but in the Sterling™ catheter model it moves. The laser is shown as the red region in Figure 5.7. The laser is stationary for 10 s in the position shown in Figure 5.7 A and then it moves 0.6 mm to the left over 8 s and finishes in the position shown in Figure 5.7 B.

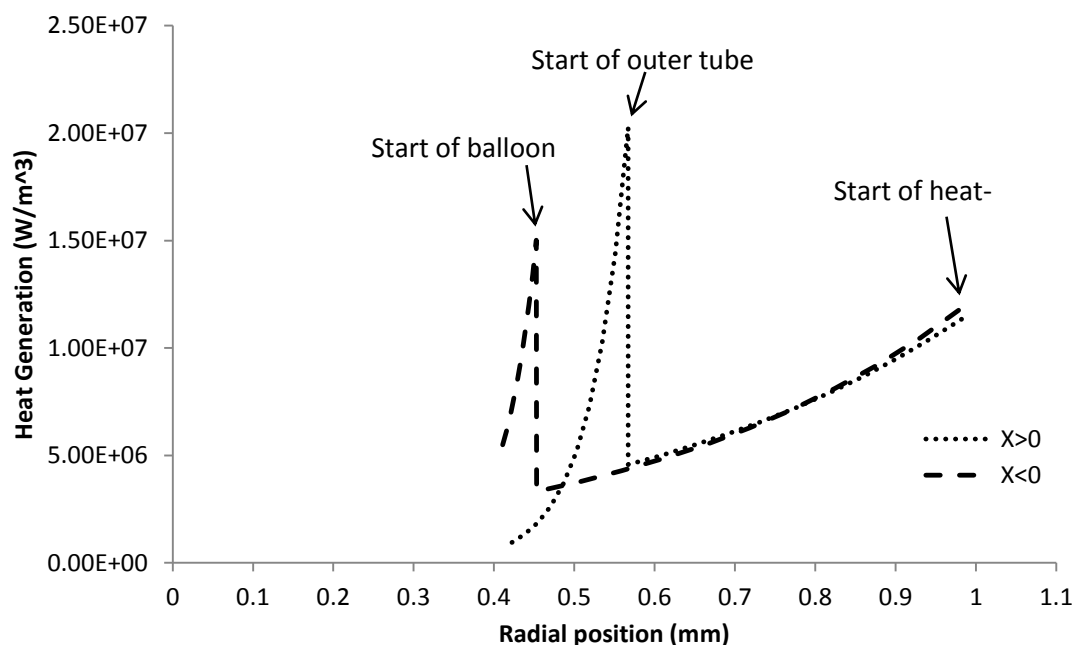
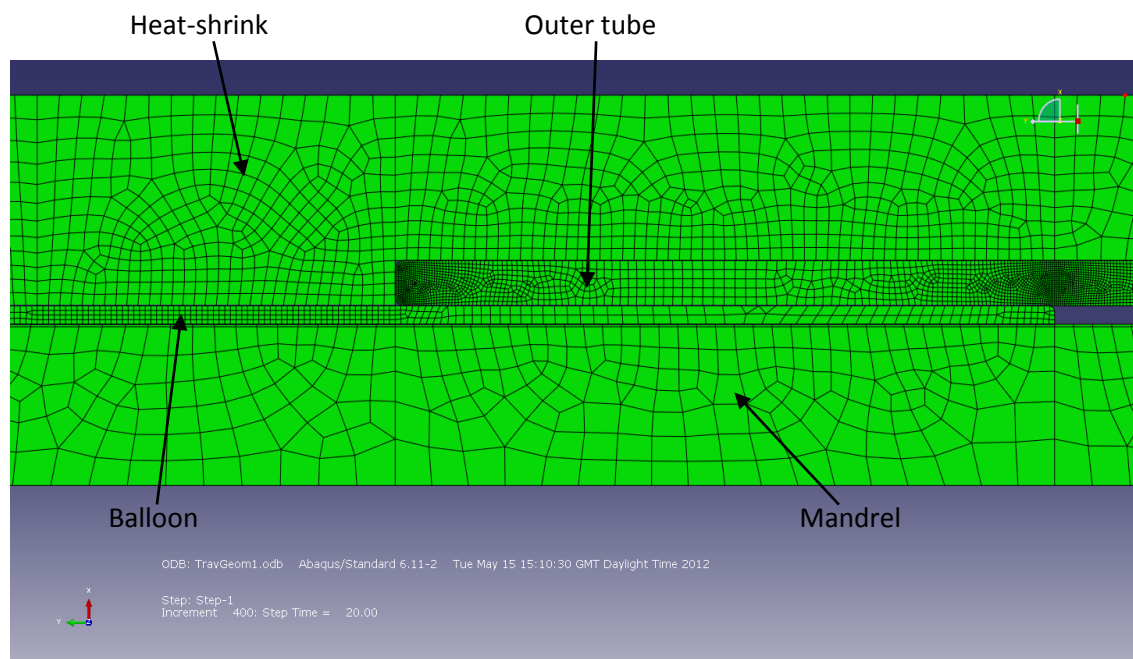


Figure 5.8 Heat generation as a function of radial position.  $X$  is the axial position shown in Figure 5.7. When  $X < 0$  (to the left of the end of the outer tube) the laser does not pass through the outer tube and when  $X > 0$  it does. Therefore, two heat generation curves are required.

The heat generation as a function of radial position is shown in Figure 5.8. There are two heat generation curves because some of the laser passes through the outer tube and some of it does not. These heat generation curves provide the thermal loading for the model. As in the previous model, heat losses through free convection and radiation are implemented, but forced convection due to the rotation of the assembly was neglected. The model consists of four parts and there is assumed to be perfect conduction between the parts when they are in contact therefore there is no contact resistance. This is achieved by setting the heat transfer coefficient to a very large number, in this case  $1 \times 10^9 \text{ W}/(\text{m}^2\text{K})$ . This is a possible limitation but as no data was available and the thermal model predictions were reasonably accurate it was deemed acceptable. In reality there will be a thermal contact resistance that decreases as the pressure increases. This thermal resistance would slightly reduce conduction between the different layers. In this case that would mean the heat-shrink would be slightly hotter and the PEBA<sup>®</sup> slightly cooler.

The mesh used for the model is shown in Figure 5.9. The model used approximately 6,000 linear heat transfer axisymmetric elements (DCAX3 and DCAX4).



**Figure 5.9 Geometry and mesh for Sterling™ thermal model.**

The material properties used in this model are summarised in Table 5.2 below.

Material	$\rho$ (kg/m <sup>3</sup> )	$c_p$ (J/kg/K)	$k$ (W/m/K)	$T_{MELT}$ (°C)	$\Delta H_{FUS}$ (J/kg)	$\alpha$ (1/m)
Mandrel	8000	$477 + 0.2267 * T$	$14.4 + 0.015 * T$	-	-	-
Teflon	2160	$630 + 1.258 * (T + 273)$	0.25	-	-	-
PEBAX®	1020	$-187 + 6.12 * (T + 273)$	0.2	162- 172	43000	18898
Heat-shrink	920	$309 + 5.09 * (T + 273)$	$= \begin{cases} 0.35 - 0.00104 * T & \text{if } 0 < T < 106 \\ 0.24 & \text{if } T \geq 106 \end{cases}$	50-102	100500	3543

**Table 5.2** Material properties used for Sterling™ thermal model.  $\rho$  is the density,  $c_p$  is the specific heat capacity,  $k$  is the conductivity,  $T_{MELT}$  is the melt temperature,  $H_{FUS}$  is the latent heat of fusion and  $\alpha$  is the absorption coefficient. The temperature,  $T$ , is measured in °C.

During the catheter assembly process at Boston Scientific, the Sterling™ catheter bond laser welding process uses a feedback loop to control the temperature. An infra-red camera is used to monitor the surface temperature of the heat-shrink during the laser welding process and a PID (proportional-integral-derivative) control algorithm is used to control the laser power. The power of the laser is adjusted to keep the temperature at a predetermined value.

Boston Scientific have modelled this PID control algorithm in detail and their results agree very well with experimental measurements [93]. In this work the PID control algorithm has not been implemented into the computational finite element models. Instead, the input power to the laser (laser drive) has been approximated (from Boston Scientific's model) as a series of discrete steps. Figure 5.10 below shows the laser drive used by Boston Scientific and the approximated one used in this work. The integral of the two curves is also plotted to ensure the same amount of energy is going into both.

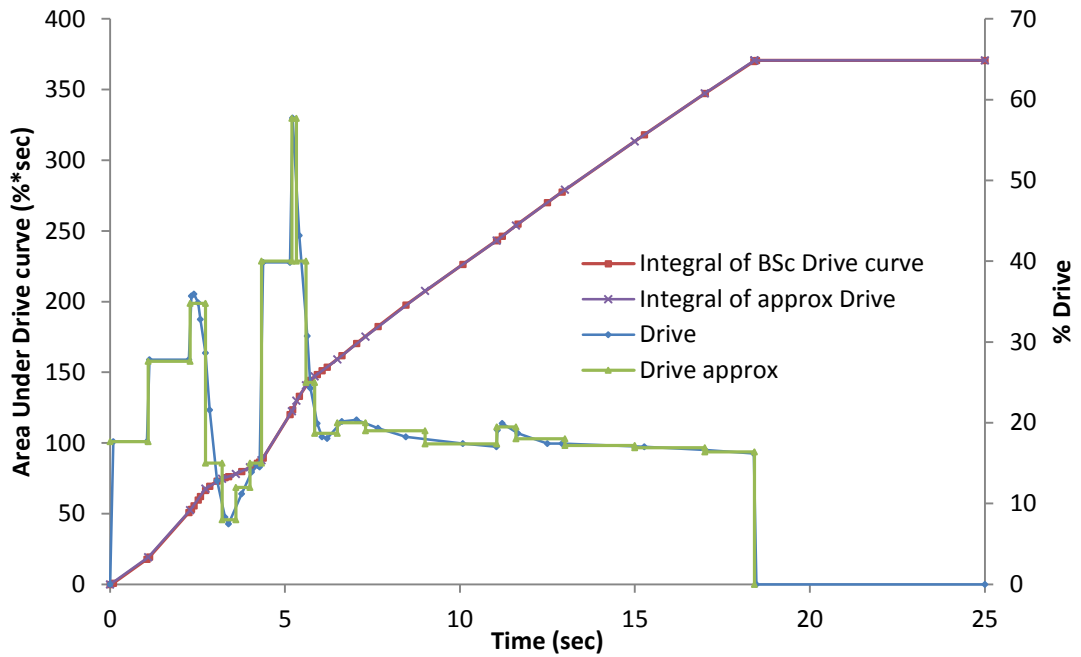


Figure 5.10 Input drive for the laser during the Sterling™ catheter laser welding process. A curve (drive approx) was fitted to Boston Scientific data [93] (drive). The integral of both curves was plotted to check that the same amount of energy is going into both.

The output power of the laser as a function of the input drive is shown below in Figure 5.11.

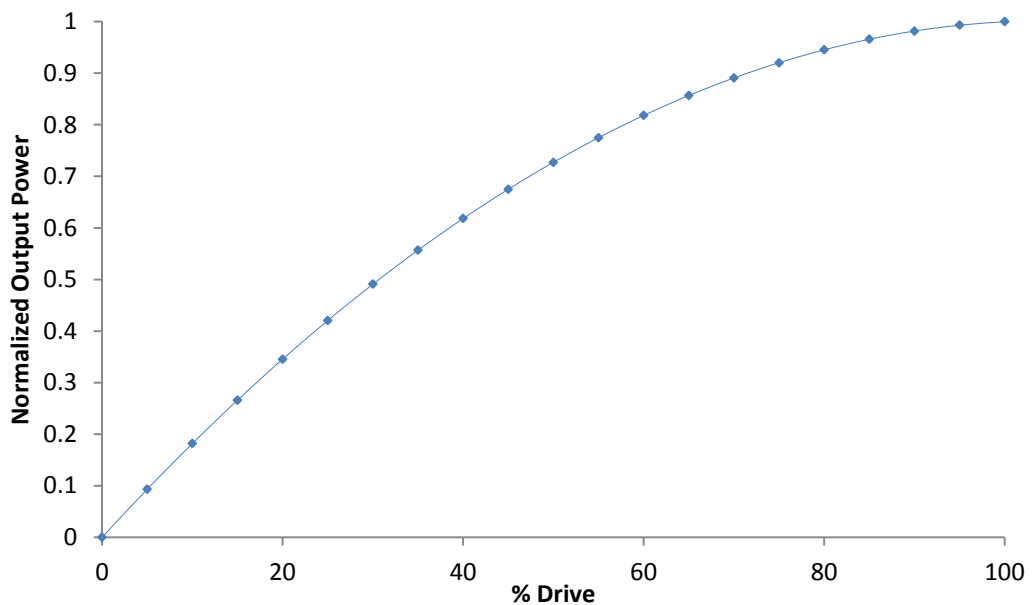
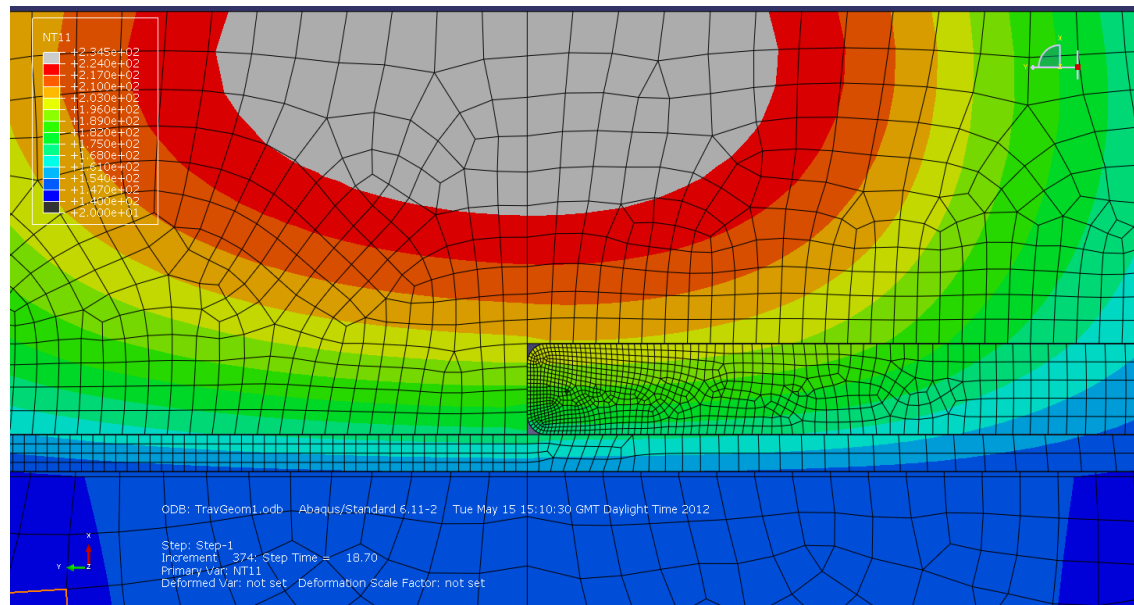


Figure 5.11 Normalized laser output power versus % input drive

The heat generation obtained from Figure 5.8 was multiplied by the normalized output power to obtain the heat generation through the assembly as the input drive varied. The

thermal aspect of the welding process was then modelled using the finite element model shown in Figure 5.8 and the results are shown in Figure 5.12 and 5.13 below.



**Figure 5.12 Temperature distribution throughout the assembly at the end of the welding process.**

Figure 5.12 above shows the temperature distribution predicted by the model at the end of the welding process just before the laser is turned off. The surface temperature predicted by the model is compared with the Boston Scientific model in Figure 5.13 below. The temperature is outputted for 0.5 mm from the centre each side of the laser beam and is averaged over this distance.

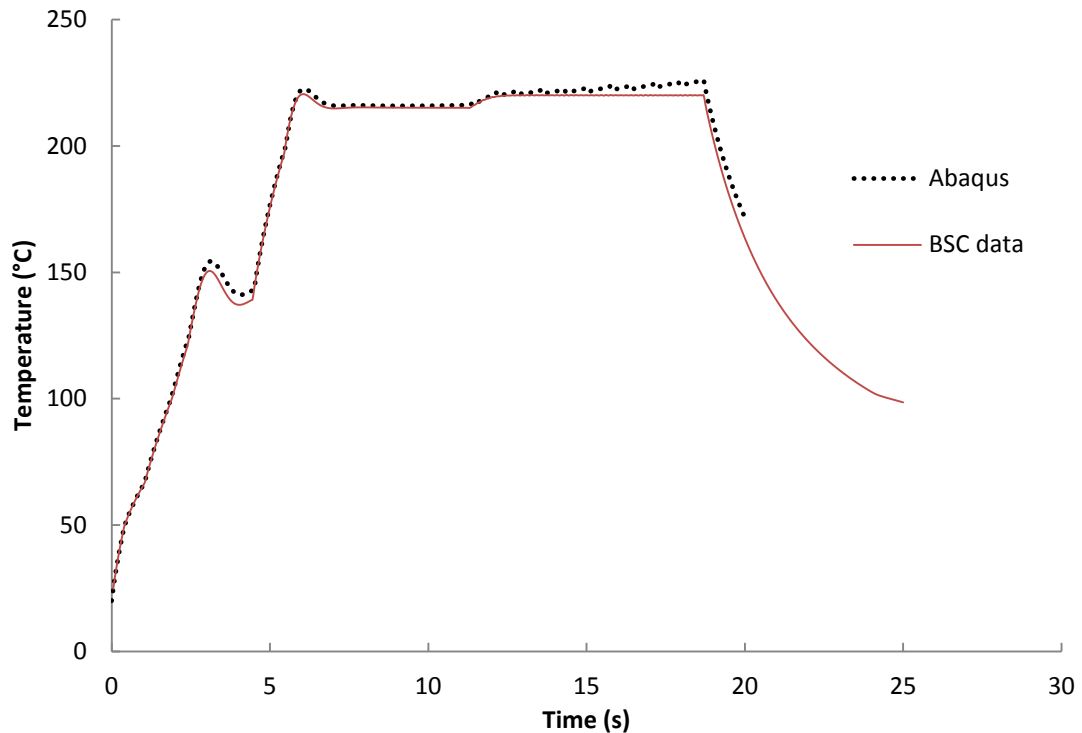


**Figure 5.13** Temperature profile at the surface of the heat-shrink (averaged over 1 mm) plotted against time. Comparison of Abaqus model and Boston Scientific model.

The temperature shown in Figure 5.13 is the surface temperature averaged over 1 mm (0.5 mm each side of the centre of the laser). The temperature ramps up to 215°C over the first 6 s and is then kept constant by the PID control algorithm which control the laser power. As can be seen in Figure 5.13, the surface temperatures of the heat-shrink of the two models agree very well.

## 5.4 Comparison of computational model with experimental data

The results of the computational thermal model of the laser welding process, described in Section 5.3 were compared to the surface temperature profile of the heat-shrink, as shown in Figure 5.13. However, the surface temperature is only one means of determining the accuracy of the temperature profile within the bonding PE layers itself. As direct experimental temperature measurements through the thickness of the bond were not possible, the thermal model predictions were compared to optical analysing images of the welded bond geometry after the laser welding process. The images were obtained through the use of polarized microscopy and OCT images (as described in Chapter 3). Figure 5.14 below shows an image of the proximal bond taken of the Sterling™ catheter following the

welding process. The PE balloon is shown on the left and the outer PE tube is shown on the right. This image only shows the surface of the bond. In order to get more detailed information about the shape of the melt pool, it is necessary to cut a section out of the bonded area. Figure 5.15 below is a polarized microscopy image of a Sterling™ proximal bond which has been cut along the axial direction.

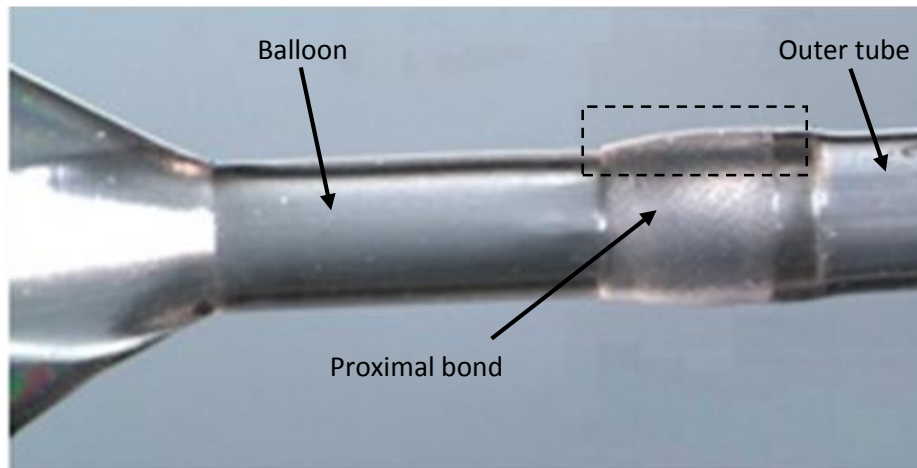


**Figure 5.14** OCT image of the proximal bond of the Sterling catheter following the laser welding process. The dashed box shows where a section of the bond was removed for polarized microscopy to determine the extent of the melt pool, as shown in Figure 5.15.

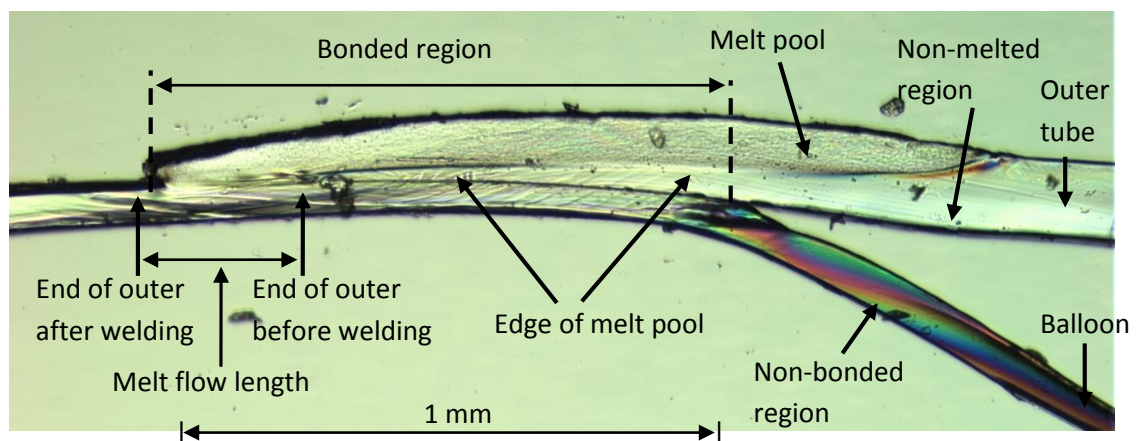


**Figure 5.15** Polarized microscopy image of the proximal bond of the Sterling™ catheter following welding.

As outlined in Section 3.4.1, polarized microscopy produces images with a good contrast between the relatively dark amorphous phase and the relatively bright crystalline phase. In Figure 5.15 above, the slightly darker region is assumed to be the melt pool which became amorphous after melting and the lighter region to the right is assumed to be the non-melted region which retained its anisotropic crystallinity from the extrusion process. The boundary between these two regions is clearly visible due to the different crystal structures. It is assumed that this boundary represents the edge of the melt pool and that the maximum

temperature reached at this boundary was approximately 172°C, which is the melting point of the PEBA<sup>®</sup>. The melt flow region to the left of the image is also clearly visible. The non-bonded region to the lower-right of the image is part of the balloon which has been separated from the outer tube. This region has separated from the outer tube as a direct result of removing the sample from the catheter and from the sample preparation for imaging.

The bonded region consists of two distinct zones. In the bonded area on the left of the image, the boundary between the outer tube and the balloon is no longer visible due to the melting and mixing of the materials. The bonded area to the right has not melted and the boundary between the outer tube and the balloon is still visible. However, this area is still bonded due to the “autohesion” between polymers at high temperatures. Autohesion occurs when two surfaces of the same elastomer bond when pressed together. It is caused by the diffusion of polymer chain ends across the interface of the two surfaces [92]. The autohesive bond strength increases with time, temperature and pressure [92].

The image shown in Figure 5.16 below shows the results of an OCT image of a Sterling<sup>™</sup> proximal bond. As discussed in Chapter 3, this imaging technique has the advantages of being non-destructive and there is no sample preparation which can affect the results. The disadvantages of this technique are that the image is not as clear as the polarized microscopy images and the dimensions in the vertical direction are affected by refraction effects and are not considered to be accurate.

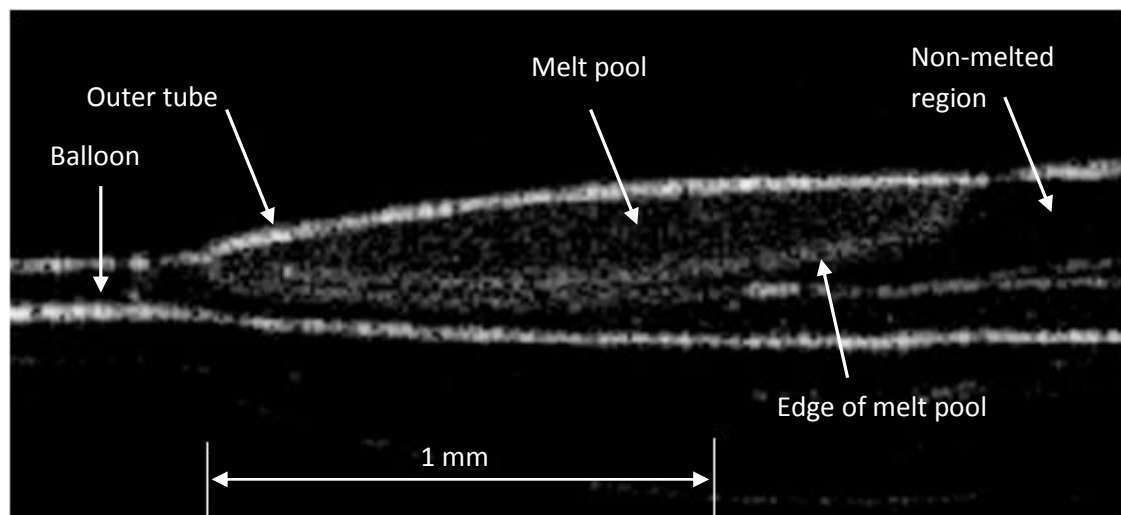
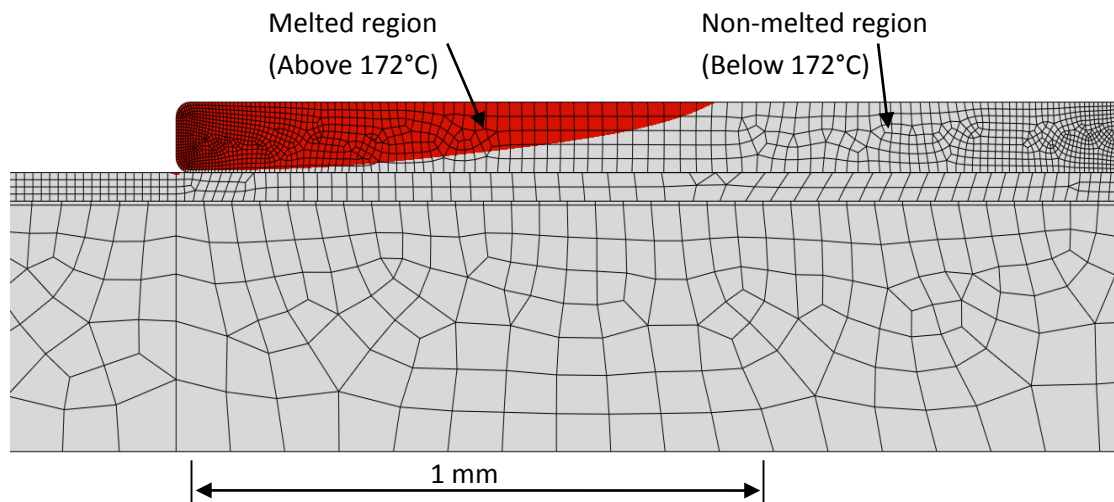


Figure 5.16 OCT image of proximal bond for Sterling<sup>™</sup> catheter following the welding process.

The contour plot below in Figure 5.17 shows the predicted area of the outer tube that exceeded the melting temperature of 172°C during the computational modelling of the

welding process. The length of the melt pool predicted by the model is 1.0 mm. This is compared with the experimental result in Figure 5.15. The length of the melt pool measured in the experiments is approximately 1.6 mm, which includes the melt flow region which was not represented within the thermal model in this work.



**Figure 5.17** The melt pool predicted by model. The red region represents the area that was heated to temperatures above 172°C during the simulation of the welding process and the gray area represents material with a predicted temperature below 172°C.

In the experimental image the melt pool at the edge of the outer tube encompasses almost all of the outer tube and comes within approximately 0.02 mm of the balloon. The melt pool predicted by the model comes within approximately 0.005 mm of the balloon.

Figure 5.18 below shows a graph of the maximum temperature reached at the interface of the balloon and the outer tube. At the edge of the outer tube ( $x=0$ ) the temperature reaches approximately 170°C which is very close to the melting temperature of 172°C. In Figure 5.15 above, the axial position of the right-hand edge of the bonded region is approximately 0.83 mm from the initial edge of the outer tube ( $x=0$ ). According to the model, the maximum

temperature reached at this point ( $x=0.83$  mm) is  $153^{\circ}\text{C}$ . This implies that the minimum temperature needed to bond the PEBA<sup>®</sup> is  $153^{\circ}\text{C}$ .

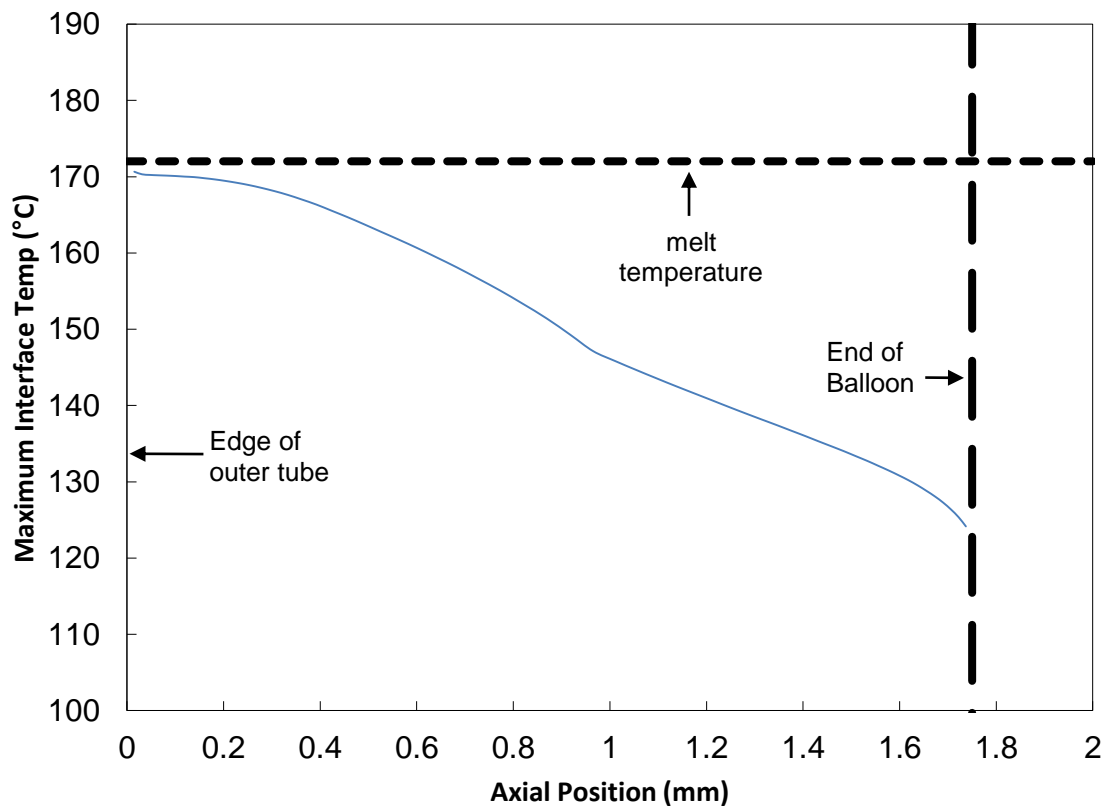


Figure 5.18 Temperature at interface of balloon and outer for model of Sterling<sup>™</sup> process. The region from  $x = 0$  to  $x = 1.75$  mm represents the area where the outer tube overlaps the balloon.

## 5.5 Discussion

Thermal models were created for two separate laser bonding processes. The first model was a preliminary investigation which involved reproducing the results of previous work by engineers at Boston Scientific. The second thermal model was for the more complicated Sterling<sup>™</sup> welding process. Both models accurately reproduced the work previously undertaken by Boston Scientific.

There are two methods available to check the accuracy of the model. The first is to compare the melt pool length in the experiment with that predicted by the model. The second is to compare the melt pool shape in the experiment with that predicted by the model. The melt pool length predicted by the Sterling<sup>™</sup> model is 1.0 mm while the observed melt flow length

is approximately 1.6 mm. One major reason the model under-predicts the size of the melt pool is that there is no melt flow in this model.

To compare the melt pool shape the model data in Figure 5.17 is compared with the experimental image in Figure 5.15. From these it can be seen that the overall shape of the melt pool is similar. Also the melt pool depths can be compared. The melt pool depth predicted by the model is approximately 0.015 mm larger than the melt pool depth seen in the experiment. This is quite a small difference and gives confidence that the temperatures predicted by the model are reasonably accurate.

Overall these models predict the temperature throughout the assembly quite accurately. This is essential for the future thermomechanical models involving melt flow (Chapter 7) as the properties of the materials vary significantly with temperature.

## **6 Implementation of thermo-mechanical model of shape memory polymer**

### **6.1 Introduction**

The purpose of this chapter is to explain in detail two of the mathematical models of shape memory behaviour reviewed in Chapter 2, and describe how they are implemented in the finite element code of Abaqus FEA. These models are used to model the behaviour of the heat-shrink tubing and therefore are an important part of this work.

Two shape memory polymer (SMP) models were implemented in Abaqus FEA. The first is the stored strain model of Liu *et al.* [64] and the second is the multiple natural configurations model of Barot *et al.* [77]. These two models were introduced in the literature review of Chapter 2 and are described in more detail here along with their implementation into the Abaqus code via a User Material (UMAT) subroutine.

### **6.2 Review of stored strain model of Liu *et al.***

Liu *et al.* [64] assumes that the polymer is a mixture of two kinds of extreme phases: The “frozen phase” and the “active phase”. The frozen phase consists of relatively stiff polymer chains which resist deformation and result in a high elastic modulus. As the material heats up these polymer chains become more flexible and cannot resist deformation, resulting in a much lower elastic modulus. This compliant phase is called the active phase. The volume fraction of each of the phase depends only on the temperature, while the thermomechanical properties of each phase stay the same.

This model uses the concept of “stored strain” to describe the shape memory effect. To incorporate the shape memory effect into a material the material is heated, stretched and then cooled. The strain that the material was stretched to is “stored” during cooling and released upon reheating.

This model assumes that the stress at a given point is the same for the frozen phase and the active phase. The strain in the material is given by a rule of mixtures addition of the strains in the active and frozen phases,

$$\boldsymbol{\varepsilon} = (1 - \varphi_F)\boldsymbol{\varepsilon}_A + \varphi_F\boldsymbol{\varepsilon}_F \quad (6.1)$$

where  $\varphi_f$  is the volume fraction of the frozen phase and  $\boldsymbol{\varepsilon}_A$ ,  $\boldsymbol{\varepsilon}_F$ , and  $\boldsymbol{\varepsilon}$  are the strains in the active phase, the frozen phase and the overall material respectively.

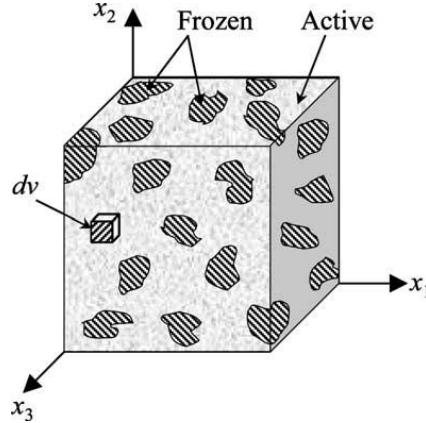


Figure 6.1 This diagram shows a polymer in an intermediate state with a predominant active phase.

This model was developed within a small-strain framework and the constitutive equation is

$$\boldsymbol{\sigma} = \mathbf{C} (\boldsymbol{\varepsilon} - \boldsymbol{\varepsilon}_s - \boldsymbol{\varepsilon}_T) \quad (6.2)$$

where  $\boldsymbol{\sigma}$  is the Cauchy stress matrix,  $\mathbf{C}$  is the stiffness matrix,  $\boldsymbol{\varepsilon}$  is the strain,  $\boldsymbol{\varepsilon}_s$  is the stored strain and  $\boldsymbol{\varepsilon}_T$  is the thermal strain. The stiffness matrix used here is the same as that used for temperature-dependent linear elasticity, where the Young's modulus,  $E$ , depends only on temperature (not on strain). Liu *et al.* give an equation which relates  $E$  to the frozen fraction.

$$E = \frac{1}{\frac{\phi_F}{E_F} + \frac{1 - \phi_F}{E_A}} \quad (6.3)$$

Where  $E_F$  and  $E_A$  are the moduli of the frozen phase and active phase respectively and are assumed to be constant and  $\varphi_f$  is the frozen fraction which can be calculated from:

$$\phi_F = 1 - \frac{1}{1 + c_f (T_h - T)^n} \quad (6.4)$$

$c_f$  and  $n$  are experimentally determined constants.

Liu *et al.* derive an expression for  $\boldsymbol{\varepsilon}_s$  in terms of the strain in the frozen phase and volume fraction. Using this expression for  $\boldsymbol{\varepsilon}_s$  and the constitutive equation above they give a differential equation which describes how the stored strain varies with temperature. In 1-D this equation is

$$\frac{d\varepsilon_S}{dT} = \frac{\varepsilon - \varepsilon_S - \varepsilon_T}{E_A \left( \frac{\phi_F}{E_F} + \frac{1 - \phi_F}{E_A} \right)} \left( \frac{d\phi_F}{dT} \right) \quad (6.5)$$

This can be solved to give an expression for  $\varepsilon_S$ . If we assume that during cooling the strain is held at a constant value (called  $\varepsilon_{pre}$ ) this expression is

$$\varepsilon_S = \varepsilon_{pre} \left( 1 - \left( \frac{E_F}{(E_A - E_F)\phi_F + E_F} \right)^{\left( \frac{E_F}{E_A - E_F} \right)} \right) \quad (6.6)$$

When  $E_F$  is much greater than  $E_A$  then this expression for  $\varepsilon_S$  is approximately the same as

$$\varepsilon_S = \varepsilon_{pre} \phi_F \quad (6.7)$$

which is easier to interpret.

### 6.3 The multiple natural configurations model of Barot *et al.*

Barot *et al.* [77] also employed a two-phase approach in their multiple natural configurations model for SMPs. The rigid frozen phase dominates at low temperatures and the relatively soft rubbery phase dominates at high temperatures. However, this model uses a finite-strain formulation so it is better suited to modelling the large deformations which typically arise in SMP applications. Another difference between this model and the stored strain model described in Section 6.2 is that in this model both phases have the same deformation gradient but the stress in each phase is different.

The multiple natural configurations model assumes that as the material freezes, the deformed configuration of the material becomes the stress-free natural configuration of the frozen phase. Therefore, the natural configuration (stress-free state) of the frozen phase can be changed by heating, stretching and cooling, but the natural configuration of the active phase remains the same. The changing of the natural configuration is how this model captures the shape memory behaviour.

The stress is given by a rule of mixtures based on the volume fraction of each phase

$$\boldsymbol{\sigma} = (1 - \varphi)\boldsymbol{\sigma}_A + \varphi\boldsymbol{\sigma}_F \quad (6.8)$$

where  $\sigma_F$  and  $\sigma_A$  are the stresses in the frozen and active phases respectively and  $\phi$  is the volume fraction of the frozen phase. The two phases are assumed to be Neo-Hookean. In the Neo-Hookean model the stresses are computed from the deformation gradient  $\mathbf{F}$ . In the Barot *et al* model the active and the frozen phases have different deformation gradients  $\mathbf{F}_A$  and  $\mathbf{F}_C$  respectively. When these are known the stress in each phase can be calculated and then summed using the rule of mixtures above to give the overall stress in the material.

Figure 6.2 below shows a graphical representation of the various deformation gradients during a shape memory cycle.

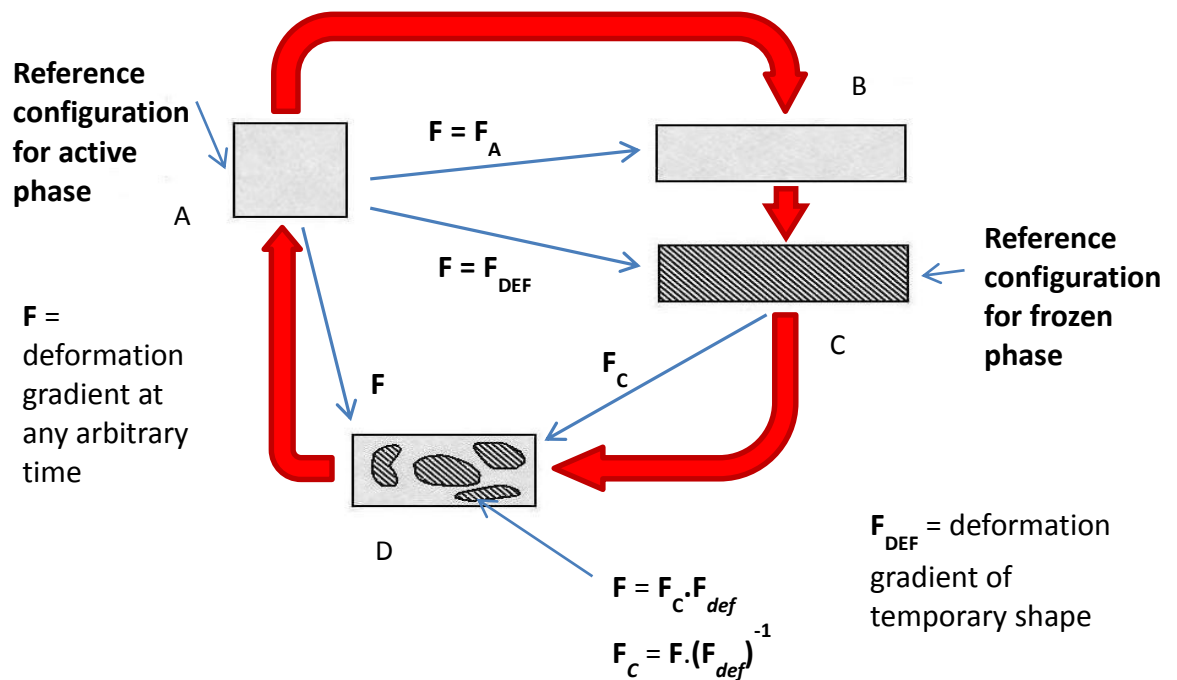


Figure 6.2 Diagram showing the deformation gradients used in the Barot *et al.* model of SMPs.

At state A, the material is in the active state and in its reference configuration (i.e. zero stress, zero strain). When the material is stretched to point B the deformation of the active phase results in a stress but the frozen phase does not contribute to the stress as all the material is in the active phase. The deformation gradient of the active phase  $\mathbf{F}_A$  is always the same as the deformation gradient of the overall material,  $\mathbf{F}$ .

When the material is cooled (point C) it forms a new reference configuration for the frozen phase. At this point the deformation gradient of the frozen phase is equal to the identity matrix,  $\mathbf{F}_C = \mathbf{I}$  (i.e. there is zero strain in the frozen phase) and the deformation of the active phase is  $\mathbf{F}_{DEF}$ , the deformation gradient of the temporary shape. As the material is all in the frozen phase, the stress contribution from the active phase is zero, and as the strain in the

frozen phase is zero, the overall stress in the material is zero. Therefore the material will remain in this temporary shape until it is reheated.

Upon reheating the frozen phase begins to be replaced by the active phase and the stress contribution from the active phase becomes significant causing the material to contract. At point D the material is in an intermediate state between frozen and active. The deformation gradient of the frozen phase,  $\mathbf{F}_C$ , is calculated from

$$\mathbf{F}_C = \mathbf{F} \cdot (\mathbf{F}_{DEF})^{-1} \quad (6.9)$$

$\mathbf{F}_C$  is then used to calculate the stress contribution from the frozen phase. The stress in the frozen phase opposes the stress in the active phase which is trying to return the material to its original shape (point A). Therefore the original shape is not recovered until all of the material is in the active state.

## 6.4 Implementation of SMP models

The two SMP models were implemented in Abaqus FEA using a User Material (UMAT) subroutine. Abaqus passes the strain (and many other variables) at the start of the increment into the UMAT. The UMAT is required to output the updated stresses and the material Jacobian matrix,  $\Delta\sigma/\Delta\epsilon$ . Abaqus then updates the strains based on the updated stress and Jacobian provided by the UMAT the updated strain is then passed into the UMAT for the next increment.

For both of these UMATs the Jacobian matrix is updated first and then this is used to update the stresses.

### 6.4.1 Implementation of stored strain model

The constitutive equation for the small strain model is

$$\boldsymbol{\sigma} = \mathbf{C} (\boldsymbol{\epsilon} - \boldsymbol{\epsilon}_s - \boldsymbol{\epsilon}_T) \quad (6.10)$$

This equation was implemented in incremental form. In rate form the stress is updated by calculating the change in stress for a given increment and adding it to the previous stress.

$$\sigma_{new} = \sigma_{old} + \Delta\sigma \quad (6.11)$$

Using index notation, the incremental form of the constitutive equation for 3 dimensions is

$$\Delta\sigma_{ij} = \lambda\delta_{ij}\Delta\varepsilon_{kk}^{el} + 2\mu\Delta\varepsilon_{ij}^{el} + \Delta\lambda\delta_{ij}\varepsilon_{kk}^{el} + 2\Delta\mu\varepsilon_{ij}^{el} \quad (6.12)$$

Where  $\delta_{ij}$  is the Kronecker delta and where the elastic strain is given by

$$\Delta\varepsilon_{ij}^{el} = \Delta\varepsilon_{ij} - \Delta\varepsilon_{sij} - \alpha\Delta T\delta_{ij} \quad (6.13)$$

The Jacobian matrix,  $\partial\Delta\sigma/\partial\Delta\varepsilon$ , for this model is the same as that for simple 3-D elasticity

$$\frac{\partial\Delta\sigma}{\partial\Delta\varepsilon} = \begin{pmatrix} \lambda + 2\mu & \lambda & \lambda & 0 & 0 & 0 \\ \lambda & \lambda + 2\mu & \lambda & 0 & 0 & 0 \\ \lambda & \lambda & \lambda + 2\mu & 0 & 0 & 0 \\ 0 & 0 & 0 & \mu & 0 & 0 \\ 0 & 0 & 0 & 0 & \mu & 0 \\ 0 & 0 & 0 & 0 & 0 & \mu \end{pmatrix} \quad (6.14)$$

where  $\lambda$  and  $\mu$  are Lamé's constants.

$\lambda$  and  $\mu$  are related to the Young's modulus,  $E$ , through

$$\lambda = \frac{E\nu}{(1+\nu)(1-2\nu)} \quad (6.15)$$

and

$$\mu = \frac{E}{2(1+\nu)} \quad (6.16)$$

The Young's modulus is a function of temperature (equation 6.3) therefore the Jacobian matrix varies with temperature. Once  $\lambda$  and  $\mu$  are determined for the new step the Jacobian can be updated.

#### 6.4.2 Implementation of multiple natural configurations model

The Neo-Hookean material model is one of the simplest hyperelastic models and its strain energy density,  $\Psi$ , is defined as follows

$$\Psi = \frac{\mu}{2}(I_1^* - 3) + \frac{\kappa}{2}(J - 1)^2 \quad (6.17)$$

where  $\mu$  is the shear modulus and  $\kappa$  is the bulk modulus.  $J$  is the determinant of the deformation gradient  $\mathbf{F}$ , and is given by  $J = \text{Det}(\mathbf{F}) = \lambda_1\lambda_2\lambda_3$  where  $\lambda_i$  are the principal stretches.  $I_1^*$  is the first invariant of the left Cauchy-Green deformation tensor  $\mathbf{B}$  ( $\mathbf{B}=\mathbf{F}\mathbf{F}^T$ ) and is given by

$$I_1^* = J^{-2/3}(\lambda_1^2 + \lambda_2^2 + \lambda_3^2) \quad (6.18)$$

The stress is given by

$$\boldsymbol{\sigma} = \frac{\mu}{J} \text{dev}(\mathbf{B}^*) + \kappa(J - 1)\mathbf{I} \quad (6.19)$$

where  $\mathbf{I}$  is the identity matrix and  $\text{dev}(\mathbf{B})$  is the deviatoric part of  $\mathbf{B}$ , that is

$$\text{dev}(\mathbf{B}^*) = \mathbf{B}^* - \frac{1}{3}I_1^*\mathbf{I} \quad (6.20)$$

and

$$\mathbf{B}^* = J^{-2/3}\mathbf{B} \quad (6.21)$$

Once the deformation gradients for both phases have been calculated (as described in Section 6.3) these equations are used to calculate the stresses in each phase separately and these stresses are summed using Equation 6.8 to give the overall stress. The volume fraction was calculated using the same method as the Liu *et al* model as shown in Equation 6.4.

Thermal expansion was also included in the UMAT using the equation

$$\mathbf{F} = \mathbf{F}_E \mathbf{F}_{TH} \quad (6.22)$$

where  $\mathbf{F}$  is the overall deformation gradient,  $\mathbf{F}_E$  is the deformation gradient due to elasticity and  $\mathbf{F}_{TH}$  is the thermal deformation gradient given by

$$\mathbf{F}_{TH} = \begin{pmatrix} 1 + \alpha\Delta T & 0 & 0 \\ 0 & 1 + \alpha\Delta T & 0 \\ 0 & 0 & 1 + \alpha\Delta T \end{pmatrix} \quad (6.23)$$

Therefore when calculating the elastic strains we need to use  $\mathbf{F}_E$ . This can be calculated from

$$\mathbf{F}_E = \mathbf{F}(\mathbf{F}_{TH})^{-1} \quad (6.24)$$

$\mathbf{F}_{TH}$  is calculated at the beginning of the increment, and then its inverse is multiplied by the deformation gradient provided by Abaqus to give the elastic deformation gradient. This elastic deformation gradient is then used in the subsequent calculation of stress.

## 6.5 Verification

Verification involves comparing the results of the UMAT with an analytical solution. This is done to ensure there are no errors in the finite element implementation of the constitutive model.

### 6.5.1 Verification of implementation of stored strain model

To test the UMAT of the stored strain model, a single-element 3-D model was created in Abaqus FEA. This element was then put through a shape-memory cycle of heating, stretching, cooling and reheating. The stretching was performed by applying a uniaxial strain, and the resulting stress was compared to an analytical solution generated using the relevant equations in a spreadsheet. The analytical solution to the small-strain formulation can be calculated easily from the equations above in Section 6.2. The results below show the imposed temperature and the resulting stress as a function of time during a shape memory cycle.

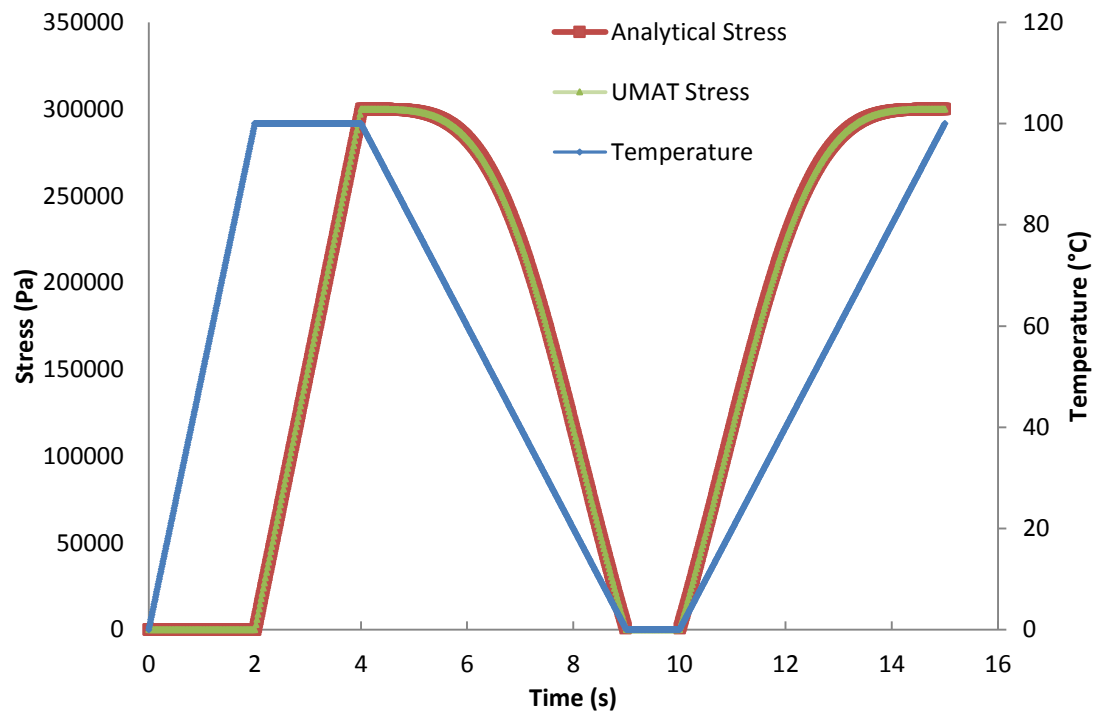


Figure 6.3 This graph shows the stress during a shape memory cycle for two models, an analytical model and a finite element model using the UMAT. Over the first two seconds the sample is heated then it is stretched. After 4 s the temperature is reduced while the strain is kept constant. The stress goes to zero as the frozen fraction increases. When the sample is reheated (after 10 s) the stress is recovered as the active phase increases. Thermal expansion is not included in this test.

Figure 6.3 above shows that the UMAT and the analytical solution agree well. This gives confidence that the UMAT has been coded correctly.

### 6.5.2 Verification of implementation of multiple natural configurations model

The analytical solution for the multiple natural configurations model is more complicated than that for the stored strain model due to the finite deformation. This was also implemented in a spreadsheet. For uniaxial tension  $\lambda_1 = \lambda$  and  $\lambda_2 = \lambda_3 = \sqrt{J/\lambda}$  and the stress is given by

$$\sigma_{11} = \frac{2\mu}{3J^{5/3}} \left( \lambda^2 - \frac{J}{\lambda} \right) + \kappa(J - 1) \quad (6.25)$$

To solve this equation it is necessary to know the value of J. To find an equation for J the stress in the lateral direction ( $\sigma_{22} = \sigma_{33}$ ) is set at zero.

$$\sigma_{22} = \sigma_{33} = \frac{\mu}{3J^{5/3}} \left( \frac{J}{\lambda} - \lambda^2 \right) + \kappa(J - 1) = 0 \quad (6.26)$$

This equation can then be solved numerically to provide a value for J which in turn can be used to calculate the stress and the lateral stretch.

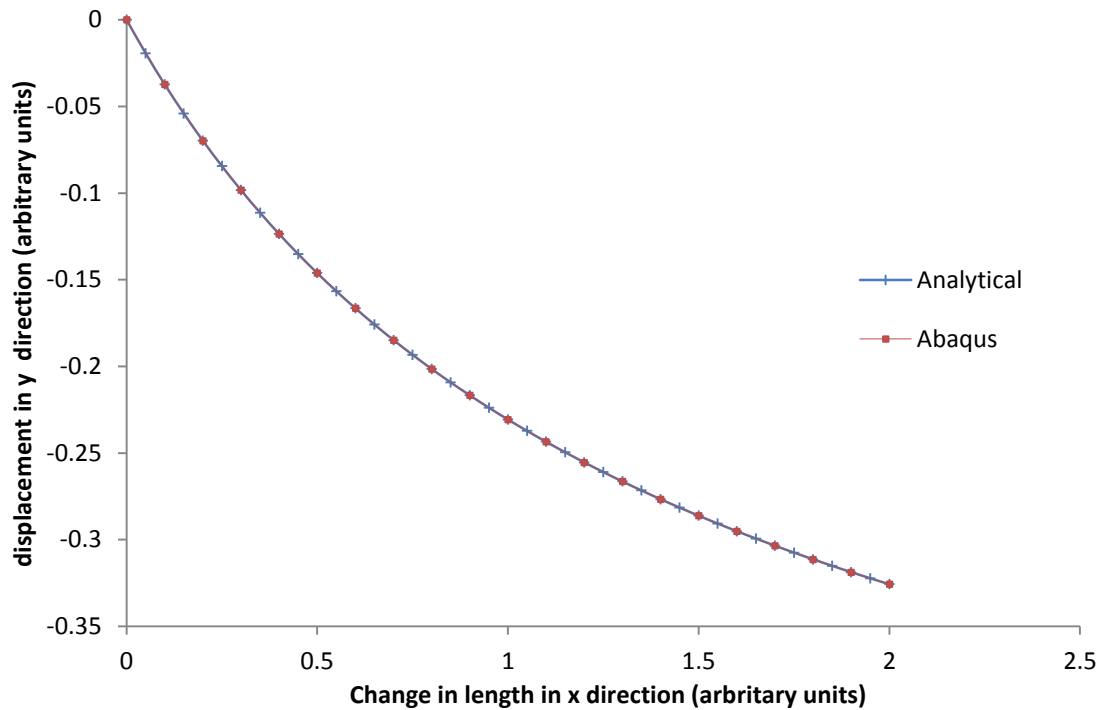
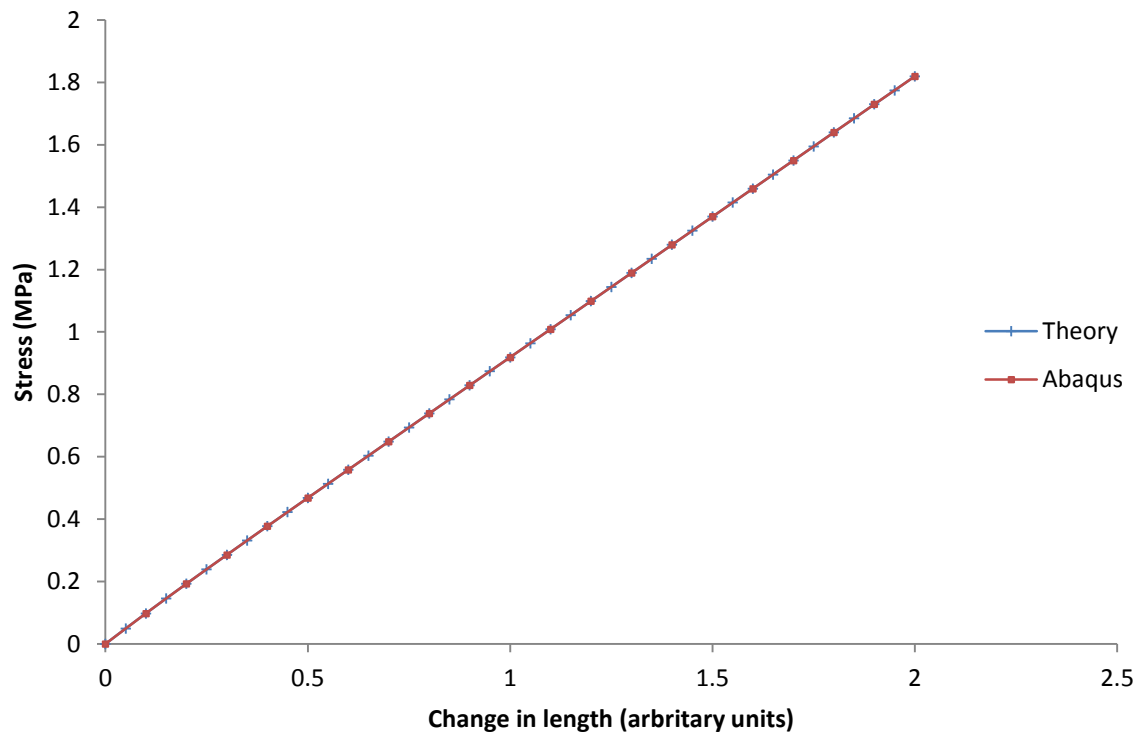


Figure 6.4 Comparison of lateral displacement for 2 models of a uniaxial tension test. One model is analytical and one is a finite element model using the built-in Abaqus model for Neo-Hookean hyperelasticity.



**Figure 6.5 Comparison of stress for two models of a uniaxial tension test. One model is analytical and one is a finite element model using the built-in Abaqus model for Neo-Hookean hyperelasticity. Poisson's ratio in this test is 0.4.**

Figures 6.4 and 6.5 above compare results from a single-element uniaxial Abaqus simulation with the analytical solution. These tests were performed to ensure the analytical model of Neo-Hookean hyperelasticity was implemented correctly. There is no shape-memory effect in these models.

The results of two models of a uniaxial test, conducted to very large strains and using a near incompressible Poisson's ratio (0.49999), are shown below in Figure 6.6.

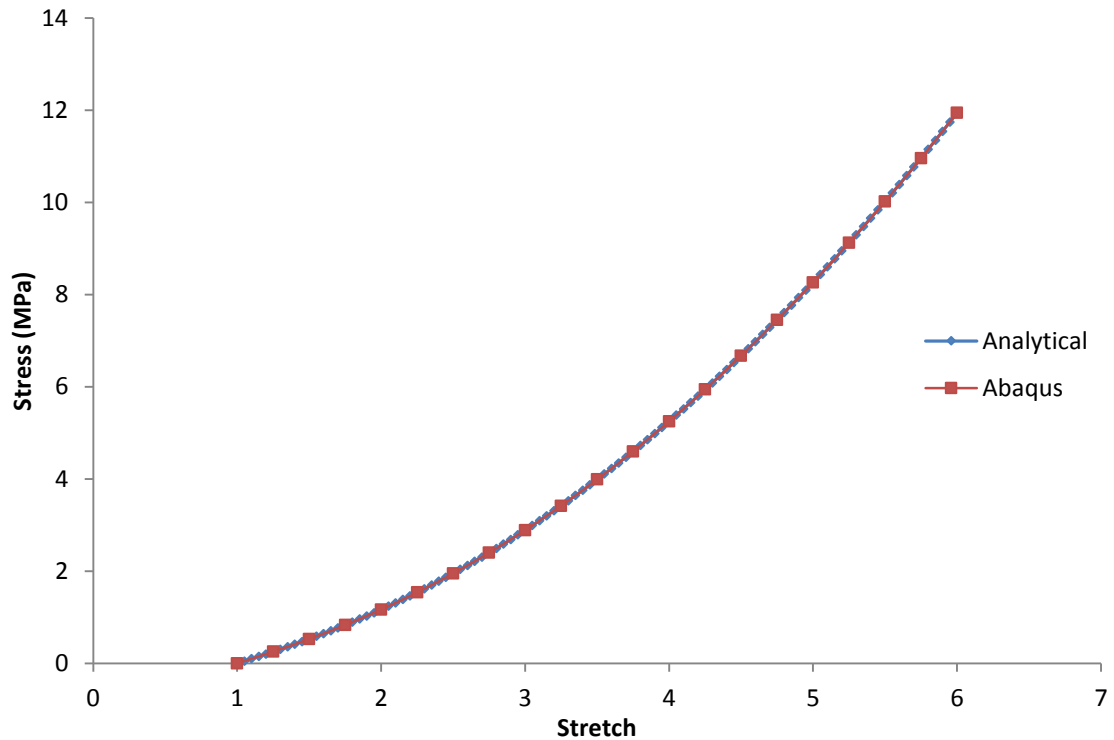


**Figure 6.6 Comparison of stress for two models of a uniaxial tension test. One model is analytical and one is a finite element model using the built-in Abaqus model for Neo-Hookean hyperelasticity. Poisson's ratio in this test is 0.49999.**

The analytical results are compared with the built-in Abaqus FEA model for Neo-Hookean hyperelasticity to ensure that the analytical model is solving the Neo-Hookean equations correctly. These results all agree well so this means the analytical solution has been implemented correctly. The analytical solution can now be used to verify that the UMAT has been implemented correctly.

Figures 6.7 and 6.8 below show how the stress varies during a shape memory cycle according to the model. These graphs compare the analytical solution with the finite element solution. Both of these graphs represent a sample going through a shape memory cycle of being heated, then stretched, then cooled, then reheated. Figure 6.8 includes the effect of thermal expansion.

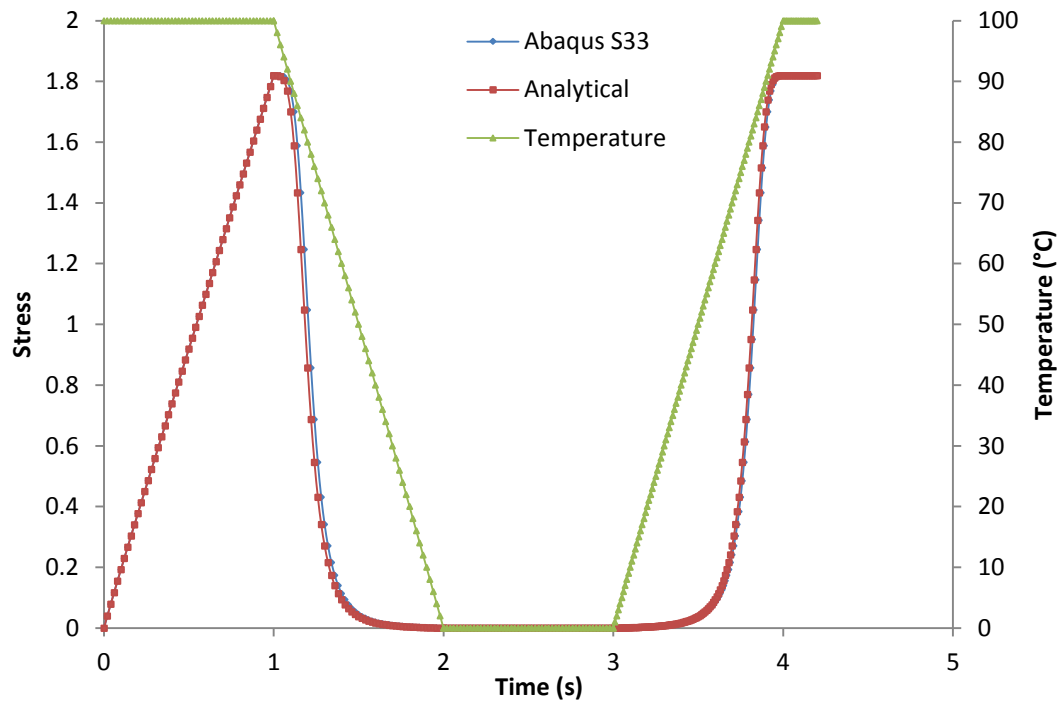


Figure 6.7 Stress during a shape memory cycle. Sample starts at a high temperature is stretched then cooled. As the sample is cooled the stress drops. When the sample is reheated (after 3 s) the stress is recovered. An arbitrary stiffness was used.

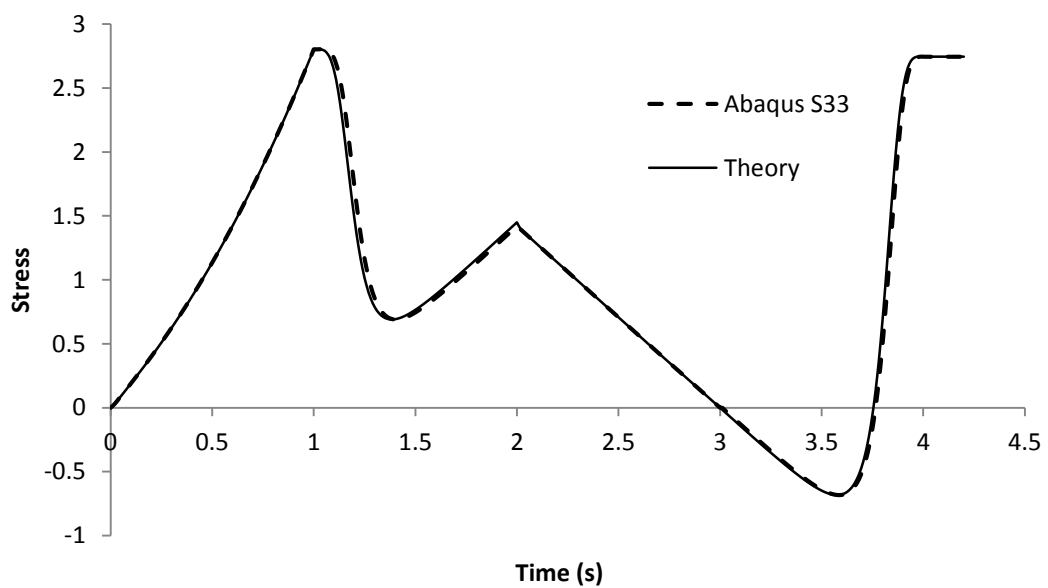
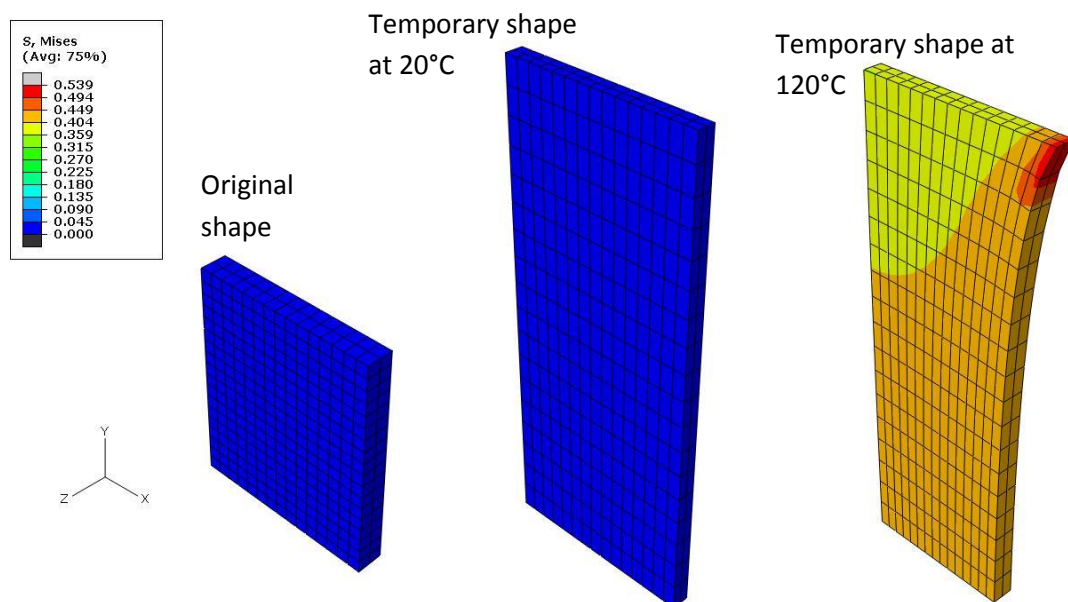


Figure 6.8 Stress during shape memory cycle including thermal expansion. Sample starts at a high temperature is stretched then cooled. Sample released gradually from 2 s then clamped again at 3 s. After 3 s the sample is reheated. The thermal expansion causes the stress to go negative (compressive) first, then the shape memory effect causes the stress to increase and the stress applied during the stretching is recovered.

Figures 6.7 and 6.8 above show that the large strain UMAT agrees with the analytical solution. This gives confidence that the UMAT has been coded correctly.

## 6.6 Comparison of UMATs with experiment

The two UMATs were tested by creating an Abaqus model of the recovery force experiment (described in section 3.2.7) and comparing the results of the simulated and experimental tests. The FE model is shown below in Figure 6.9. It consists of a thin material (same dimensions as used in the experiment) which is meshed with 3-D quadratic elements and stretched uniaxially (in the y direction) while at a high temperature. The material is then cooled and due to the shape memory retains this shape. Boundary conditions are then applied to prevent the material from contracting in the y direction and then it is reheated. Due to symmetry, it was only necessary to model one quarter of the sample.



**Figure 6.9** FE model of recovery force experiment. The sample on the left was heated, stretched, cooled and released. This left it in the stress-free elongated form shown in the centre. The sample is then constrained in the y direction and reheated result in the stressed shape shown on the right. The contours show the Von-Mises stress in MPa.

As the material heats up a stress is produced as the material tries to contract but is held by the applied boundary conditions. The reaction force in the y-direction for each element is then summed to produce the simulated shrink force which is then compared with experiment.

### 6.6.1 Stored strain model

The results of the simulations of the recovery force test using the stored strain UMAT are shown below. The test was done with a modulus of 0.44 MPa. This modulus was determined in Section 4.13. Figure 4.12 shows the graph which was used to determine the modulus.

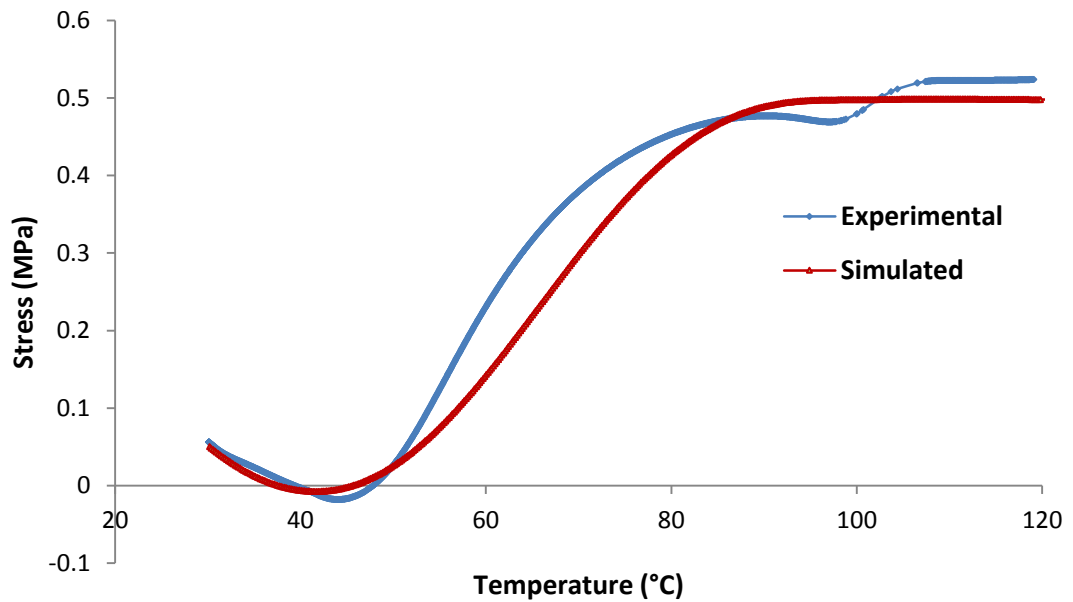


Figure 6.10 Recovery stress of heat-shrink during in uniaxial tension test. Comparison of the stored strain UMAT with experimental test.

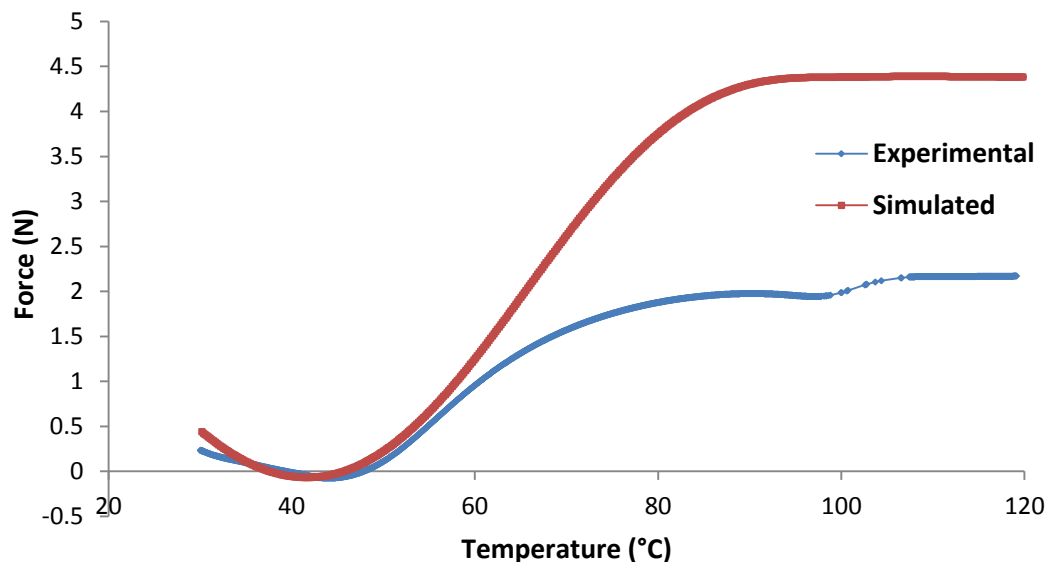
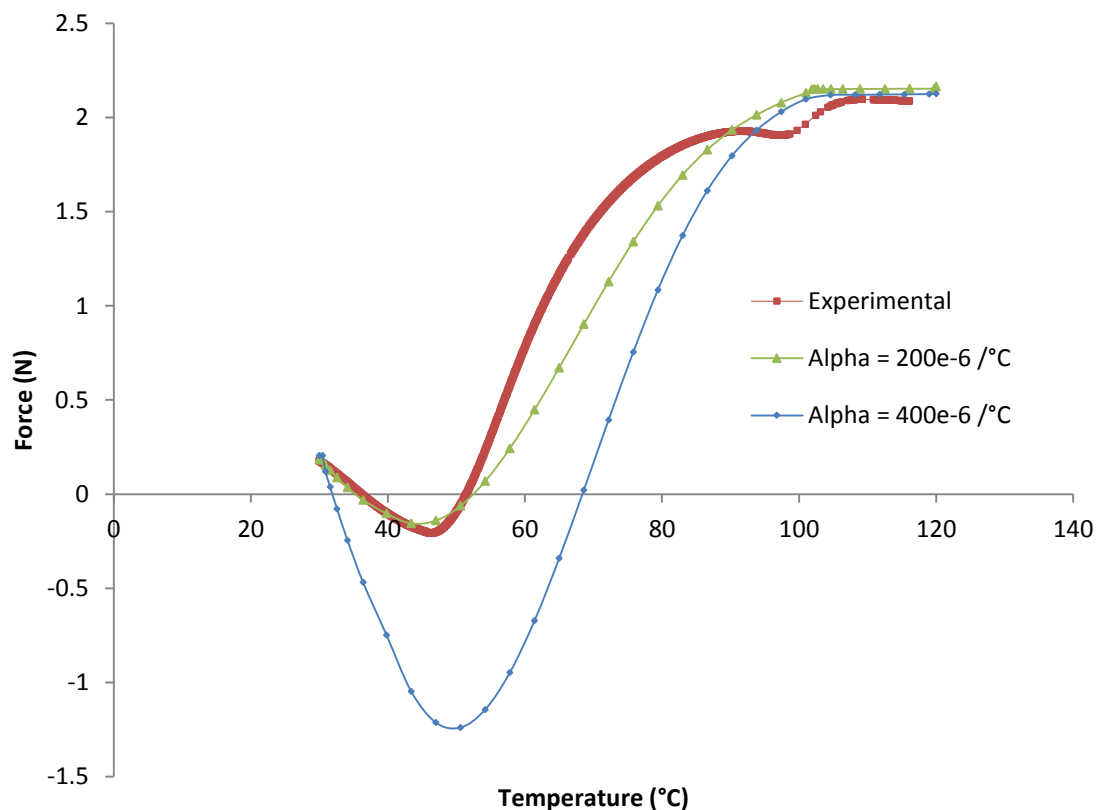


Figure 6.11 Recovery force of heat-shrink during in uniaxial tension test. Comparison of the stored strain UMAT with experimental test.

The stored strain model predicts the recovery stress quite well but the deformation of the cross sectional area is unrealistic. This produces a force which does not agree with the experimental results.

### 6.6.2 Multiple natural configurations model

The finite deformation UMAT was then used to model the same recovery force test used in the previous section. The modulus  $E = 0.44 \text{ MPa}$  was used as determined from Figure 4.12.



**Figure 6.12** Recovery force of heat-shrink during in uniaxial tension test. Comparison of multiple natural configurations UMAT with experimental test. Two thermal expansion coefficients have been used and the modulus used is  $0.44 \text{ MPa}$ .

The force at the end of the test ( $120^\circ\text{C}$ ) agrees well with experiment. The recovery force during the test is highly dependent on the thermal expansion coefficient used but the force at the end of the test is not. The measured thermal expansion coefficient of  $4 \times 10^{-4} \text{ }^\circ\text{C}^{-1}$  produces a negative force significantly larger than that observed in the experiment. With the thermal expansion set to  $2 \times 10^{-4} \text{ }^\circ\text{C}^{-1}$  the simulated and experimental tests agree well.

The multiple natural configurations UMAT was then used to model the behaviour of the heat-shrink tubing in a FE model of the hanger test described in Section 3.5. Due to the symmetry

of the hanger test it was possible to model just a quarter of the assembly. The heat-shrink tubing is modelled using the large strain UMAT with the modulus calculated from the pressure test section (Section 4.7). The model set-up is shown below in Figure 6.13. The image on the left shows the model after the heat-shrink has been stretched out and cooled. The image on the right shows the assembly at the end of the test after the heat-shrink has been reheated and has contracted onto the hanger.

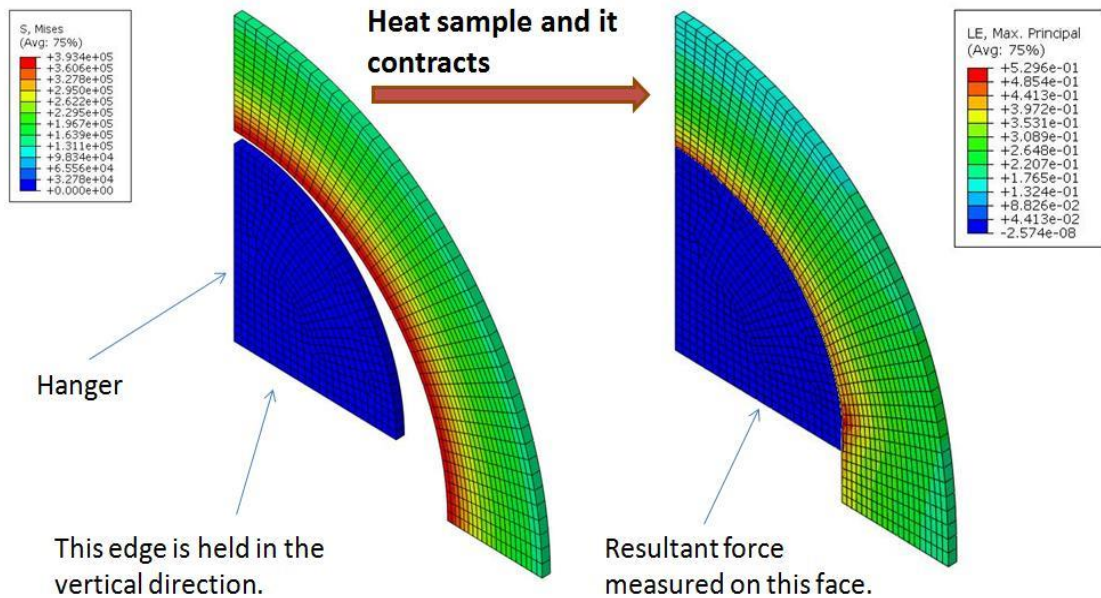


Figure 6.13 Schematic diagram of the finite element model of the hanger test.

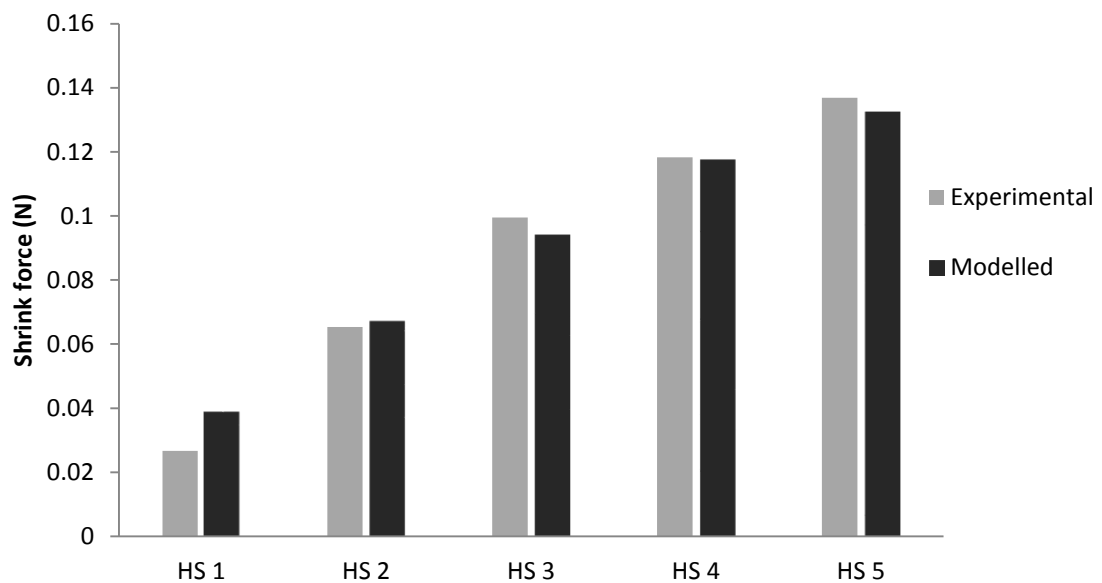


Figure 6.14 Comparison of shrink force predicted by Abaqus model and shrink force measured by hanger test experiment.

Comparison of the hanger test model and the experimental hanger test is shown above in Figure 6.14. The simulation agrees well with the experiment for 4 out of the 5 heat-shrink grades. However a higher shrink force was predicted than that measured by experiment for the first tube (HS1). It should be recognized that as the shrink force gets smaller the percentage error in both the pressure test and the shrink force test will increase. A comparison of the shrink force predicted by the model and that measured by experiment is given below in Table 6.1.

Shrink Force (N)	Experimental	Modelled	Error (N)	Error %
HS 1	0.027	0.039	0.0123	46.1
HS 2	0.065	0.067	0.002	3.1
HS 3	0.099	0.094	0.005	5.1
HS 4	0.118	0.117	0.001	0.85
HS 5	0.137	0.132	0.005	3.6

**Table 6.1 Comparison of shrink force predicted by FE model using multiple natural configurations UMAT and the shrink force measured by experiment.**

## 6.7 Material model for PEBAX®

The manufacturers of PEBAX®, Arkemia, have made a large amount of PEBAX® properties available online via the CAMPUS (computer aided material preselection by uniform standards) [85] database. This was used to obtain PEBAX® properties below the melting point and data for PEBAX® above the melting point was obtained from the literature [86].

The material model used to model the PEBAX® was a viscoelastic model using a Prony series along with the time-temperature superposition to capture the behaviour of the material with time and temperature.

### 6.7.1 Prony series

A Prony series [87] consists of a number of Maxwell elements connected in parallel and a spring connected in parallel with the whole array (Figure 6.15).

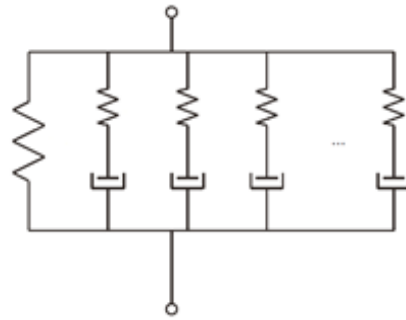


Figure 6.15 A Prony series.

The Prony series can be used to model the stress relaxation behaviour for a polymer. A large number of elements can be used to accurately capture the relaxation over an extended period of time. The equation for how the modulus changes with time is

$$E(t) = E_0 - \sum_{i=1}^N E_i \left[ 1 - e^{-\frac{t}{\tau_i}} \right] \quad (6.27)$$

Where  $E_0$  is the instantaneous modulus,  $N$  is the number of elements in the model and  $E_i$  and  $\tau_i$  are the moduli and relaxation constants of relevant Maxwell element. Abaqus assumes that the viscoelastic material is defined by a Prony series expansion of the dimensionless relaxation modulus  $g(t)$

$$g(t) = \frac{E(t)}{E_0} = 1 - \sum_{i=1}^N g_i \left[ 1 - e^{-\frac{t}{\tau_i}} \right] \quad (6.28)$$

where  $g_i$  range from 0 to 1 and the sum of  $g_i$  over  $N$  must be less than 1. The relaxation modulus terms,  $g_i$ , define how much that element relaxes. For example if  $g_i = 0$  then this element causes no reduction in the overall modulus of the material and if  $g_i = 0.9$  there will be a 90% reduction in the overall modulus of the material. The time at which these relaxations occur is determined by the relaxation constants,  $\tau_i$ . To implement the Prony series in Abaqus FEA, the two parameters required for each element are  $g_i$  and  $\tau_i$ .

### 6.7.2 Time-temperature superposition

The time-temperature superposition (TTS) principle [88] can be used to determine the mechanical properties of temperature-dependent linear viscoelastic materials from known properties at a reference temperature. The time-temperature superposition uses a reduced time concept where the effect of increasing the temperature is assumed to be the same as the effect of decreasing the time. The modulus as a function of time for three temperatures is shown in Figure 6.16. If the modulus is known at one reference temperature ( $T_{REF}$ ) then

the modulus at higher temperatures ( $T_1$ ,  $T_2$ ) can be estimated by shifting the reference curve to the left. This shift factor,  $a_T$ , is illustrated in Figure 6.16. The modulus curve can also be shifted to the right for lower temperatures if required. The TTS is usually used for amorphous polymers whereas the PEBA<sup>®</sup> is a semi-crystalline polymer. However as the material is above its crystalline melting point it is all in the amorphous phase and so it was considered acceptable.

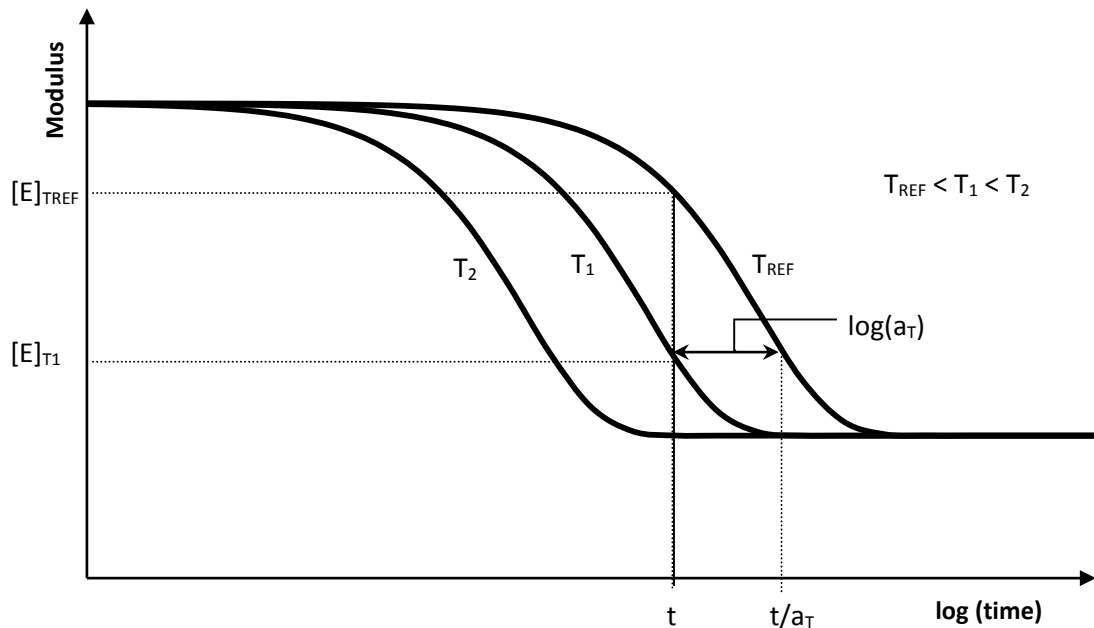


**Figure 6.16** Modulus as a function of time for three temperatures. The time-temperature superposition uses a reduced time to represent the behaviour of the material at higher temperatures.

There is a uniform distance ( $\log(a_T)$ ) between the  $T_{REF}$  curve and the  $T_1$  curve. If the modulus as a function of time is known at the temperature  $T_{REF}$  then the modulus at  $T_1$  can be calculated by using a time ( $t/a_T$ ) as shown in Figure 6.16. This means the modulus at a time  $t$  and temperature  $T_1$  can be calculated using Equation 6.29.

$$[E(t)]_{T_1} = \left[ E \left( \frac{t}{a_T} \right) \right]_{T_{REF}} \quad (6.29)$$

The time-temperature superposition was implemented in Abaqus FEA using a user subroutine (UTRS) to control how much the curve was shifted. This reduced time concept for temperature dependence is usually referred to as thermo-rheologically simple (TRS) temperature dependence. The modulus calculated from the TTS is then used as the instantaneous modulus  $E_0$  for the Prony series Equation 6.27.

### 6.7.3 PEBAX® data

The data needed to create a material model for PEBAX® was obtained from the literature and from the manufactures' (Arkema) website [89]. The manufactures website has DMTA data up to 166°C and is shown in Figure 6.17 below. This was used to calibrate the PEBAX® model while it was in the solid phase. Rheometry data obtained from the literature [86] was used to calibrate the model in the molten phase.

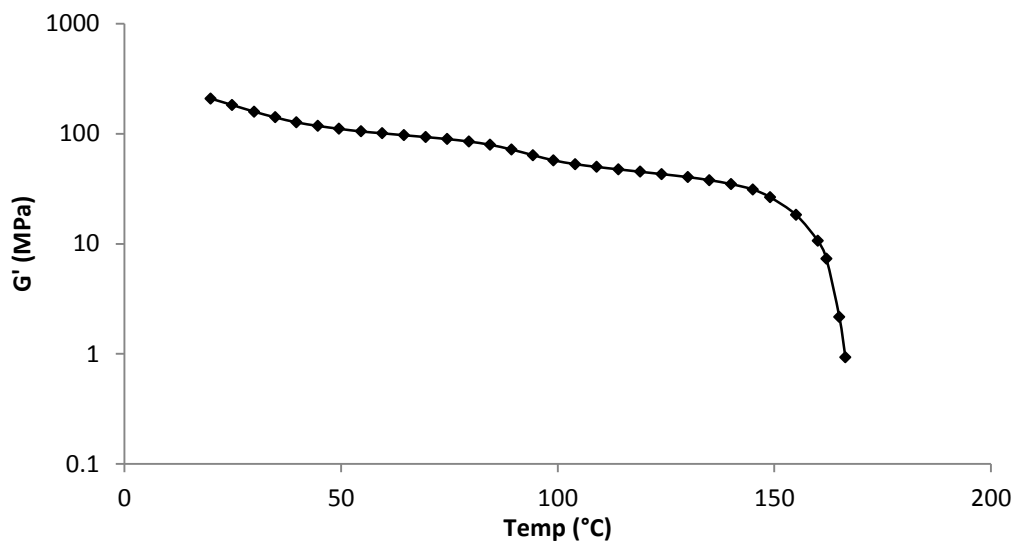


Figure 6.17 Variation of the shear storage modulus,  $G'$ , with temperature [89].

The rheometry data from the literature [86] is shown below in Figure 6.18. This data was for PEBAX® 5533 while the PEBAX® used in the welding process is 7033. Viscosity data is available for PEBAX® 7033 (and PEBAX® 5533) from Arkema but only for temperatures above 200°C. The viscosities of PEBAX® 5533 and PEBAX® 7033 above 200°C are very similar (as seen in Figure 6.18) and it was assumed therefore that the rheometry data for PEBAX® 5533 could be applied to PEBAX® 7033.

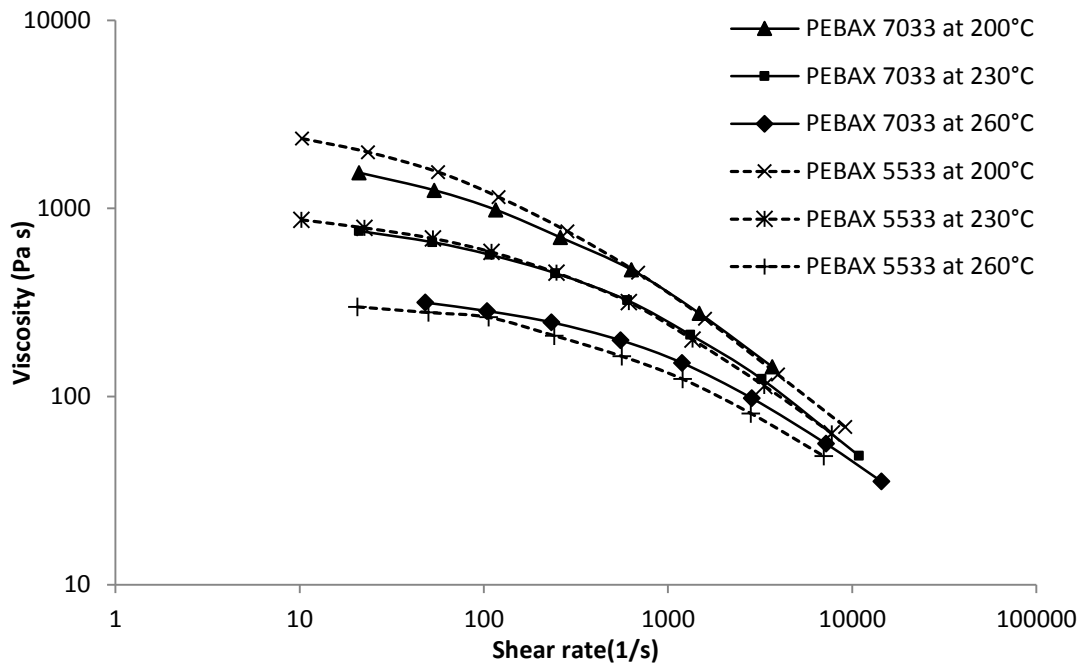


Figure 6.18 Viscosity as a function of shear rate for two grades of PEBAx® at three different temperatures. Data obtained from Campus database [85].

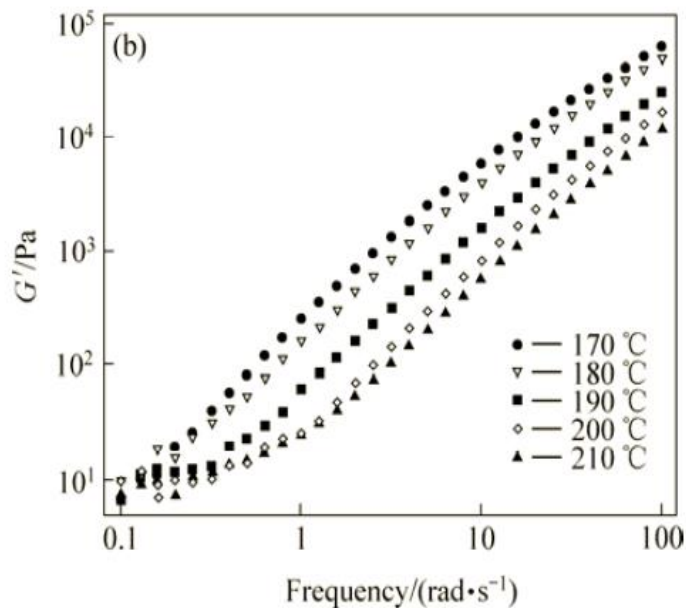
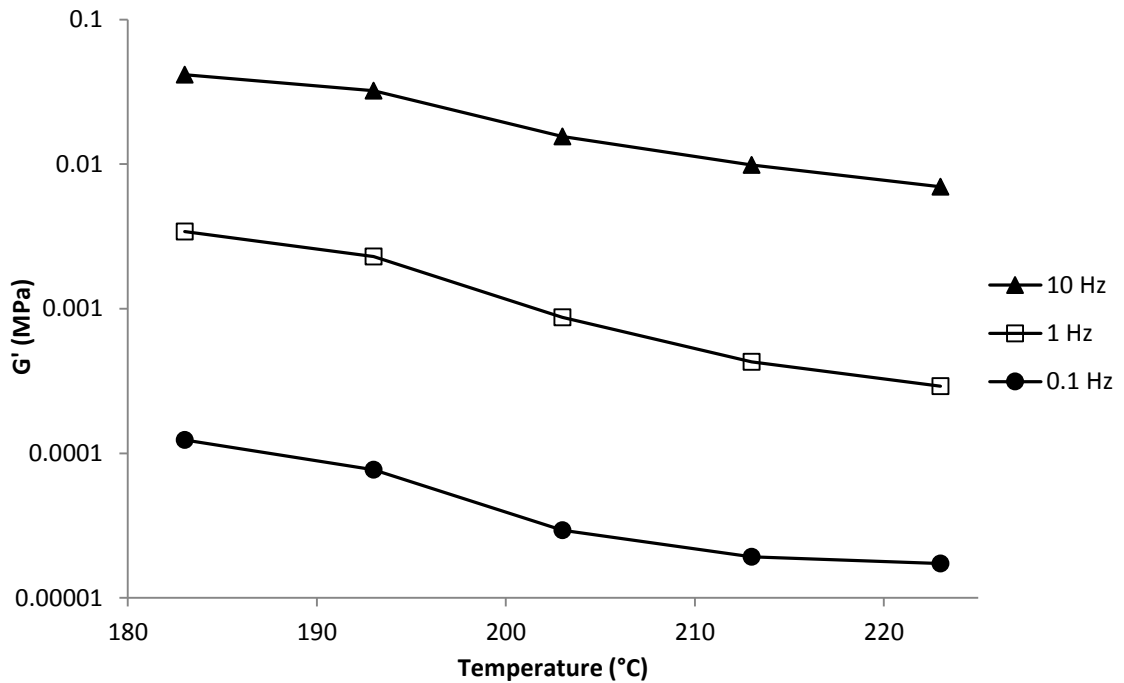


Figure 6.19 Rheometer data for PEBAx® 5533 showing modulus increasing rapidly with frequency and decreasing with temperature [86]

The rheometer data in Figure 6.19 was converted to a modulus as a function of temperature graph to allow comparison with DMTA data. To do this the frequency was converted to Hz from rad/s and then the modulus at three frequencies (0.1 Hz, 1 Hz and 10 Hz) was plotted for each of the five temperatures in Figure 6.20. The different grades of PEBAx® have different melting temperatures with the PEBAx® 5533 melting 13°C lower than the PEBAx® 7033. It was assumed that shifting the temperature by 13°C would allow the PEBAx® 5533

data to be used to approximate the PEBA<sup>®</sup> 7033. Therefore, the modulus of PEBA<sup>®</sup> 5533 at 170°C was used to approximate the modulus of PEBA<sup>®</sup> 7033 at 183°C and so on for the other temperatures. The modulus as a function of temperature is shown below in Figure 6.20.



**Figure 6.20** Data used to approximate the shear modulus of PEBA<sup>®</sup> 7033 above its melting temperature. Data converted from [86].

The properties in the molten state can now be compared with the properties in the solid state. However, there is a gap in data between 166°C and 183°C. As no data was available for this region, interpolation was used to generate data. The modulus as a function of temperature at 1 Hz is shown below in Figure 6.21 over the temperature ranges of interest.

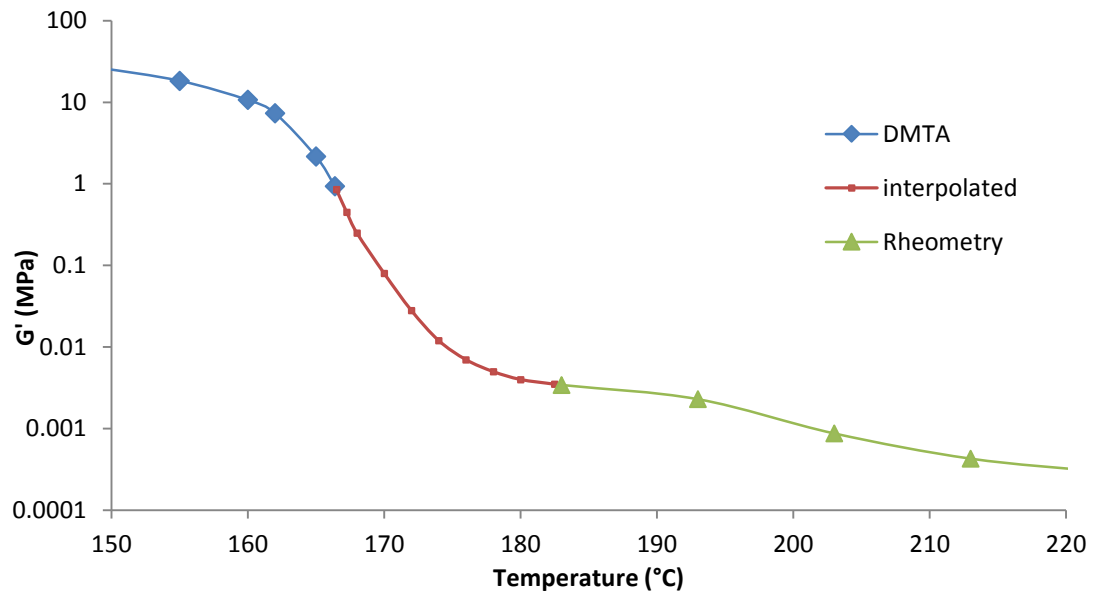


Figure 6.21 Curve showing interpolated data around the melt temperature.

This graph was used to create a material model for the PEBAx<sup>®</sup>. First a Prony series was fit to this data as shown in Figure 6.22.

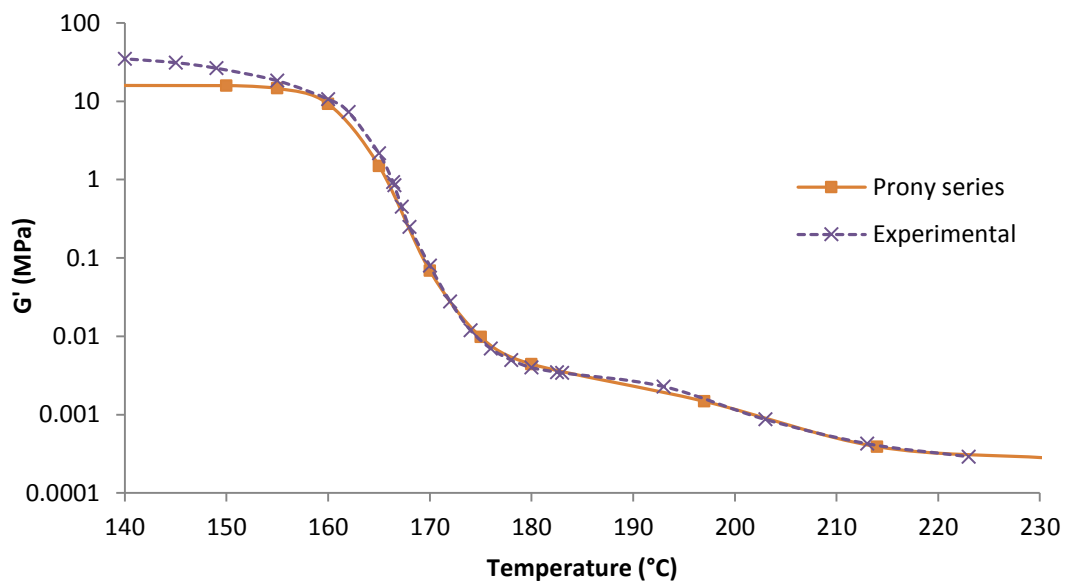


Figure 6.22 Fitting of Prony series to experimental data.

This Prony series used six terms and they are given below in Table 6.2

Prony series term	$g$ (relaxation modulus)	$\tau_i$ (relaxation constant)
1	0.899999	0.005
2	0.089999	0.005
3	0.0089999	0.1
4	0.00089999	0.5
5	$8.9999 \times 10^{-6}$	10
6	$8.9999 \times 10^{-6}$	10

Table 6.2. Terms uses for fitting Prony series to experimental data.

The time-temperature superposition (TTS) was used to implement the dependence of the modulus on both time and temperature by shifting the curve in Figure 6.22 to the left or right depending on time.

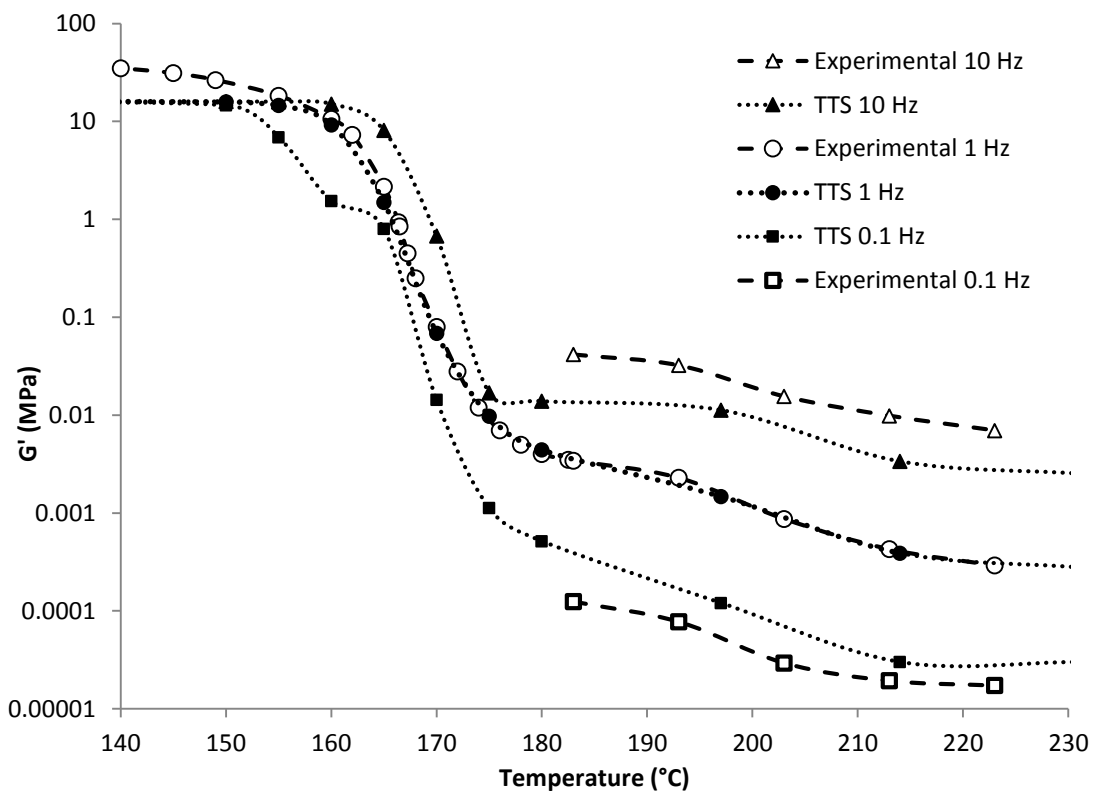


Figure 6.23 Fitting of material model to experimental data.  $G'$  is the shear modulus.

A Prony series with six terms was used in conjunction with the TTS to fit a curve to the experimental data (Figure 6.23).

As can be seen from Figure 6.23, when the material is below 155°C, the modulus is above 10 MPa. As the pressure applied by the heat-shrink is only on the order of 0.2 MPa, this means that very little deformation will occur. Therefore it was assumed that the modulus below

155°C did not need to be accurately modelled. This made the process of fitting the Prony series and TTS parameters easier.

## 6.8 Discussion

Two shape memory polymer models have been implemented in the finite element code Abaqus FEA using two subroutines. The stored strain model is for small strains only while the multiple natural configurations model can be used to model large strain problems. The two models have been tested by comparing the shrink force produced in an experimental test with the shrink force produced by a FE model of that test. These results show that the multiple natural configurations model is able to replicate the behaviour of the heat-shrink tubing while the stored strain model is not suitable for the deformation levels present in the heat-shrink tubing. Also, data from literature has been used to create a material model for the PEBAX®.

Only the multiple natural configurations model will be used in the full thermomechanical model of the laser bonding process. Using the modulus determined from the pressure test in Section 4.7, this model can reproduce the experimental shrink force from the hanger test to within 5% for most cases. As described in Chapter Four, the effects of viscoelasticity, plasticity and anisotropy are relatively small and are not modelled for ease of implementation. Attempts to minimise the error introduced by these simplifications are discussed below.

In Section 4.1.2 it was shown that the viscoelasticity of the heat-shrink tubing causes the modulus to increase by 20% when the strain rate is increased by a factor of 10. This rate dependent behaviour is not captured by this model but the modulus used in the model is measured at approximately the same time scales as present in the welding process in an attempt to minimize the error.

The plasticity of the heat-shrink also affects the accuracy of the model. The plastic properties of heat-shrink are documented in Section 4.1.4. For this work the heat-shrink tubing was received in its expanded state. All measurements of the tube were taken after this initial expansion and the diameter of the tube before its initial expansion is not known. The initial diameter of the tube used in the model is obtained by measuring the tube after shrinking. This diameter will be slightly larger than the actual initial diameter due to the plasticity of the tube. This means that while the model does not include plasticity the diameter of the tube after shrinking is accurate.

A material model was developed to model the PEBA<sup>®</sup> as it melts. A Prony series was used along with the time-temperature superposition to model the viscoelastic behaviour of the PEBA<sup>®</sup>. In Figure 6.23 the fitting of the model to the experimental data is shown. As the PEBA<sup>®</sup> melts, the modulus drops very rapidly. When the temperature increases from 150°C to 200°C, the modulus decreases by a factor of approximately 10,000. Also the behaviour of the molten PEBA<sup>®</sup> is very frequency dependent as it is effectively a viscous liquid. This makes modelling this material as a solid model with a Lagrangian mesh very difficult.

## **7 Thermo-mechanical modelling of balloon catheter laser welding process**

### **7.1 Introduction**

The purpose of this work was to investigate the laser welding of balloon catheters and to gain insights into the deformation and flow characteristics, as well as the stresses and strains associated with the process. In the previous chapters, various aspects of the welding process were investigated. These include the thermal profile through the various layers of the assembly (Chapter 5) to the behaviour of the heat-shrink used to induce pressure on the PEBAX® layers to be welded (Chapter 6). In this chapter, these different aspects are integrated to produce a full thermomechanical model of the laser welding process.

The particular bond that is modelled is the proximal bond of a catheter from a product line called Sterling™. This bond was chosen as the most data was available and experiments could be performed on this product more easily given the resources available at the time. It is intended that the methods used here could be applied to model many other bonds across different product lines.

In this chapter, full simulations of the entire welding process are described and performed. Results of the laser welding model are presented with an emphasis on the melt flow length of the PEBAX®. The melt flow length of the PEBAX® is defined as the distance from the distal edge of the outer tube before welding to the distal edge of the outer tube after welding. The melt flow length of the PEBAX® is chosen because it is the variable which is easiest to quantify in experimental testing and hence as a means of validating the modelling approach used in this work.

The impact of different parameters (friction, heat-shrink modulus and initial deformation) on melt flow was investigated by performing simulations while varying the values of these parameters. In the case of friction, no experimental data was available, and so a range of values was chosen to produce a large variation of melt flow values as a means of determining the sensitivity of friction values on the overall results. The pressure applied by the heat-shrink tube on the assembly depends on the modulus of the heat-shrink. Therefore, the heat-

shrink modulus is an important parameter and its effect on the process was investigated by performing computational simulations with different values.

To assess the accuracy of the models, experimental testing was performed. These experiments involved welding catheters while varying the shrink force of the heat-shrink tubing. These bonds were then imaged using optical coherence tomography (OCT) and the melt flow measured. The experimental results were then compared with the predictions of the simulations.

## 7.2 Thermo-mechanical model development

The full simulation of the laser bonding process incorporates all the processes discussed previously in this work. The thermal profile during the laser welding process was described in Chapter 5. In Chapter 4, the properties of the heat-shrink tubing were investigated and in Chapter 6 the heat-shrink tubing was modelled with the development of a shape memory polymer UMAT. This UMAT was validated in Chapter 6 and is incorporated into the thermo-mechanical simulation in this work. The role of the heat-shrink material is to impose radial pressure on the weld assembly with increasing temperature without itself forming part of the balloon catheter weld. The constitutive behaviour of the Polyethylene material (PEBAX®) used in the construction of both the catheter and the balloon was considered in Chapter 4. The complexity in modelling this material behaviour was considered as it transitions from a solid extrusion to a viscous flowing 'liquid'. The overall material model used a temperature dependent viscoelastic solid material to characterise the material behaviour. This material model is used in the full simulations of the laser welding process in this chapter.

### 7.2.1 Laser weld assembly geometry

The basic construction of the geometry is shown in Figure 7.1, below. The geometry is axisymmetric and the model is made up of four parts:

- the stainless steel cylindrical mandrel with a diameter of 0.8 mm
- the polyethylene (PEBAX®) balloon, with an internal diameter of 0.8 mm and wall thickness of 0.046 mm
- the outer polyethylene (PEBAX®) tube, with an internal diameter of 0.89 mm and a wall thickness of 0.114 mm

- and the EVA copolymer heat-shrink tubing, whose dimensions change upon reaching a critical (phase transforming) temperature of approximately 100°C.

The length of the overlapped joint is 1.75 mm and the overall length of the assembly modelled is 50 mm with an overall radius of approximately 1 mm.

In the finite element model constructed to reflect the assembly, the heat-shrink tubing is initially represented in its 'as formed', stress free configuration. A temperature load is then imposed on the heat-shrink material and simultaneously stretched to its nominal diameter at which stage it is cooled so the shape memory has already been programmed into the material at the point shown in Figure 7.1 below. This method of modelling the processing of the heat-shrink material is described in more detail in Chapter 6.

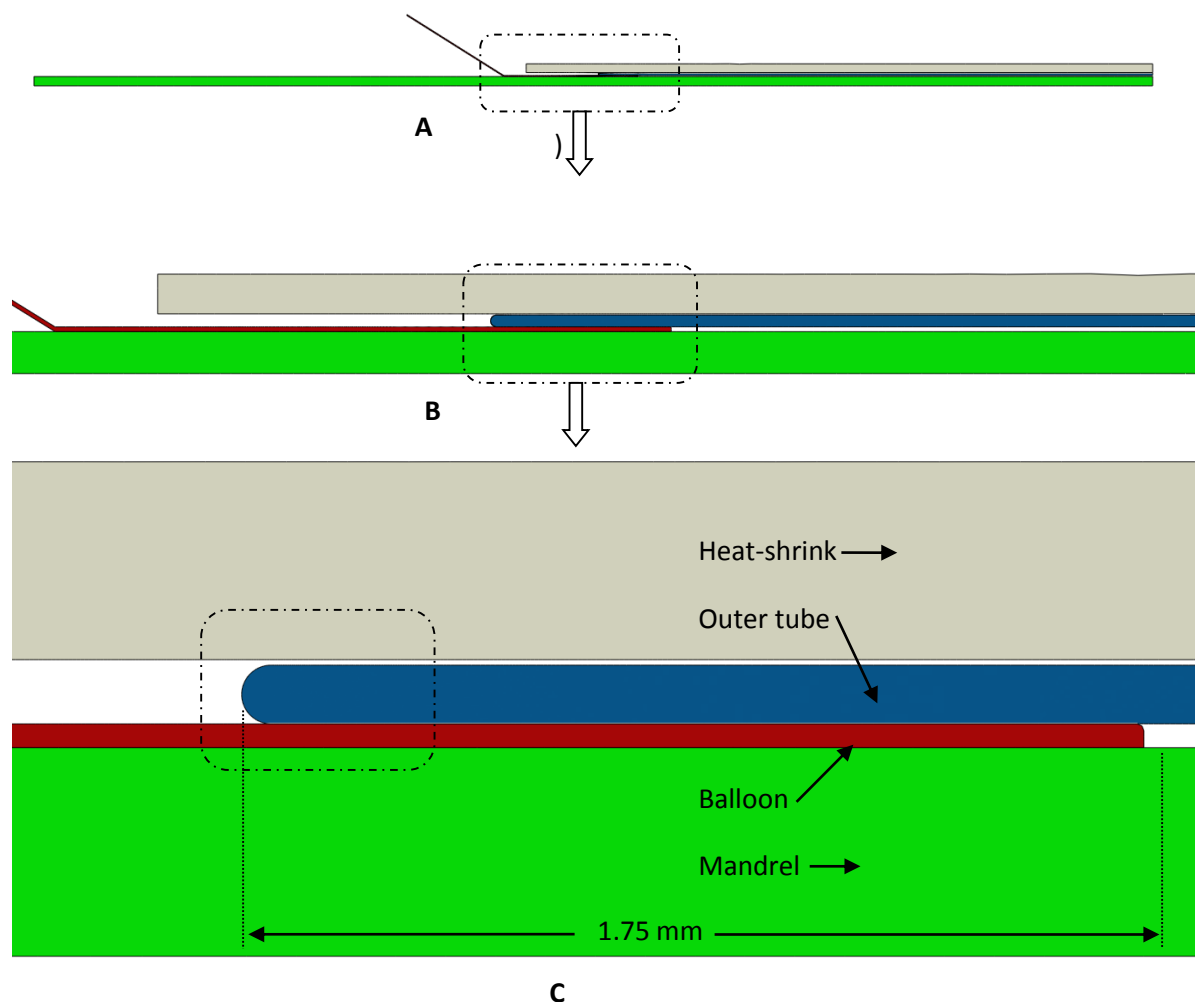


Figure 7.1 Axisymmetric geometry of model for simulation of laser welding of Sterling™ balloon catheter. Figures (A)-(C) show the assembly with increasing detail. The in-built small gap between the heat-shrink and the outer tube is shown. When the heat-shrink is heated, it contracts and comes into contact with the outer.

For some of the simulations, the outer PEBA<sup>®</sup> tube started off in a state with an assumed initial deformation. This is described in more detail in section 7.3.3.

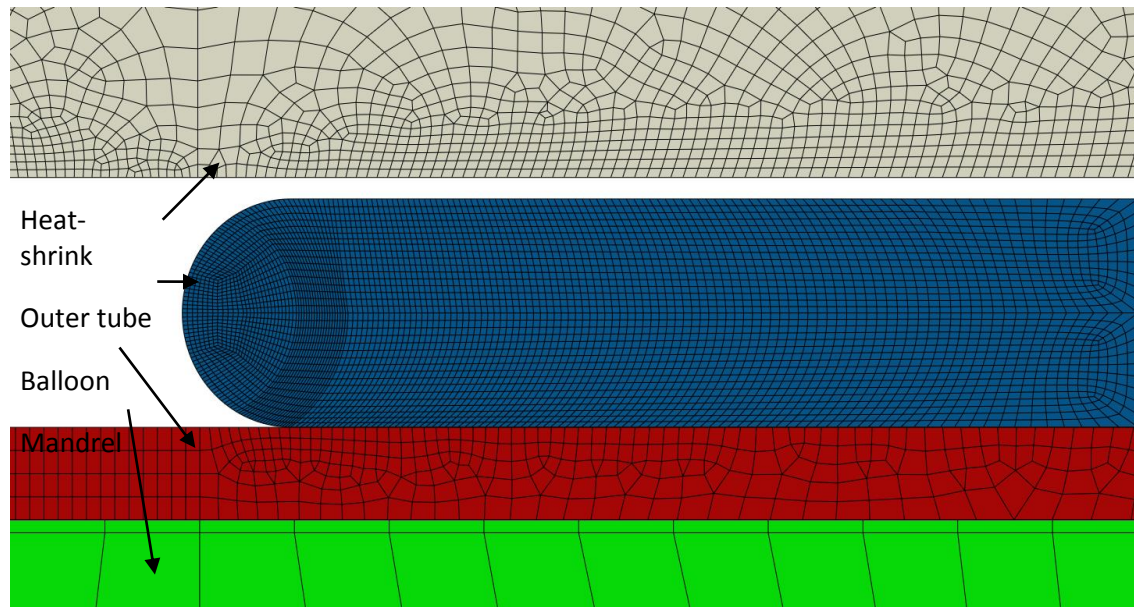


Figure 7.2 Part of the axisymmetric mesh used for a model of Sterling™ bonding process.

### 7.2.2 Mesh

The finite element mesh constructed had approximately 12,000 2D axisymmetric quadrilateral and triangular (CAX4T and CAX3T) linear elements. The mesh density is highest at the tip of the PEBA<sup>®</sup> (shown in Figure 7.2) as this is the region where the most deformation is predicted to occur. The outer tube was assumed to have a rounded geometry, as representing the end of the outer tube with a ‘squared’ corner caused excessive deformation at the corner elements, upon loading. A curved mesh was used to reduce this excessive mesh deformation.

### 7.2.3 Boundary conditions

The left and right edges of the mandrel, balloon and heat-shrink are constrained in the axial direction, while just the right edge of the outer tube is constrained axially. In these models the mechanical load is not applied directly to the outer tube. Instead the heat-shrink is subjected to a simulated temperature load of 100°C, then stretched using a displacement boundary condition of 0.159 mm (to the position shown in Figure 7.2 above) and then cooled back to room temperature while the displacement is maintained. This is the method used to

induce the shape memory polymer internal stress, as described in the development of this thermo-mechanical behaviour of the heat-shrink in Chapter 6. Following the simulation of the forming of the heat-shrink material - the laser then heats the assembly and the heat-shrink tubing contracts onto the assembly. This produces the mechanical loading for the model.

#### **7.2.4 Thermomechanical loading**

The thermal load applied to the geometry above in Figure 7.2 is the same as that described in Section 5.3. This thermal load reflects the temperatures experienced by the materials during the welding process. In this model, the conductivity of the PEBAX® in the outer tube is set at a relatively high value of  $1.0 \text{ Wm}^{-1}\text{K}^{-1}$ . The thermal conductivity value used by Boston scientific is  $0.2 \text{ Wm}^{-1}\text{K}^{-1}$ . The higher value of 1.0 was chosen as it greatly aids the generation of a converged finite element solution through reducing the thermal gradient (and hence the deformation gradient) within the melted PEBAX® layer. A realistic value of  $0.2 \text{ Wm}^{-1}\text{K}^{-1}$  causes the top of the outer tube to become much hotter than the lower part of the PEBAX® and this causes the top to excessively shear and produce excessive deformation. The higher conductivity value of 1.0 changes the thermal solution and this is a limitation of this technique but it was deemed necessary to get the model to converge.

#### **7.2.5 Contact**

In this model, contact between the various layers of the assembly need to be simulated. This is modelled using the built-in penalty contact model in the finite element code Abaqus Version 6.11. This model assumes the pressure between the two surfaces to be zero when the surfaces are more than  $0.2 \mu\text{m}$  apart and it begins to increase linearly once the gap becomes less than  $0.2 \mu\text{m}$ . As the gap approaches zero, the pressure approaches 1 MPa. If the gap becomes less than zero, a situation known as overclosure, the pressure continues to increase linearly. However in this model the pressure does not exceed 1 MPa so overclosure does not occur. The 1 MPa pressure was chosen to prevent overclosure as this often causes convergence problems. The effect of the coefficient of friction was investigated over a range of values to determine the sensitivity of the solution to frictional values.

## 7.2.6 Materials

The heat-shrink is modelled using the user defined material model (UMAT) for shape memory polymers (SMP) described in Section 6.4. The modulus used for the majority of the tests was 0.5 MPa as measured in Section 4.1.3. For some of the tests, the effect of modulus was investigated to determine its effect on the melt flow. For these tests the modulus ranged from 0.3 MPa to 1.3 MPa as this was the range used in an experimental investigation of melt flow dependence on shrink force.

The PEBAX<sup>®</sup> is modelled as a temperature-dependent viscoelastic material as described in Section 6.7. However, a boundary condition is placed on the lower PEBAX<sup>®</sup> layer (the balloon) to prevent it from moving in order to simplify the computational analysis.

The mandrel is made of stainless steel with a thin coating of Teflon and both are modelled as linear elastic materials with a Young's modulus of 300 GPa. The thermal properties are described in Section 5.3.

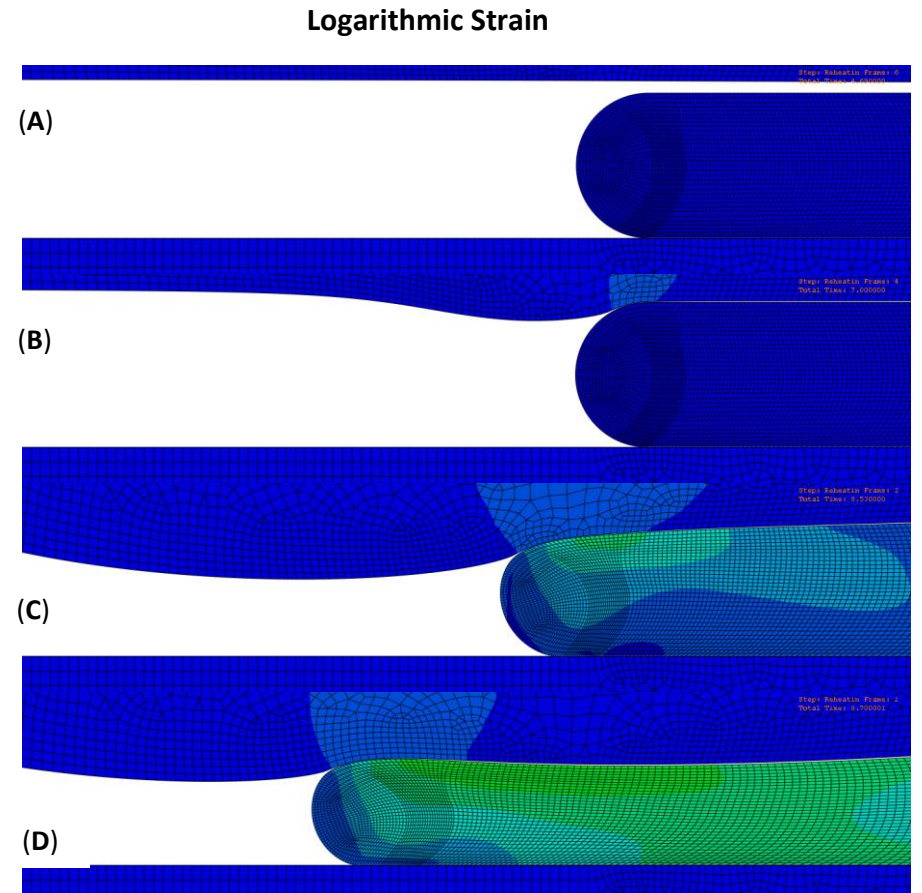
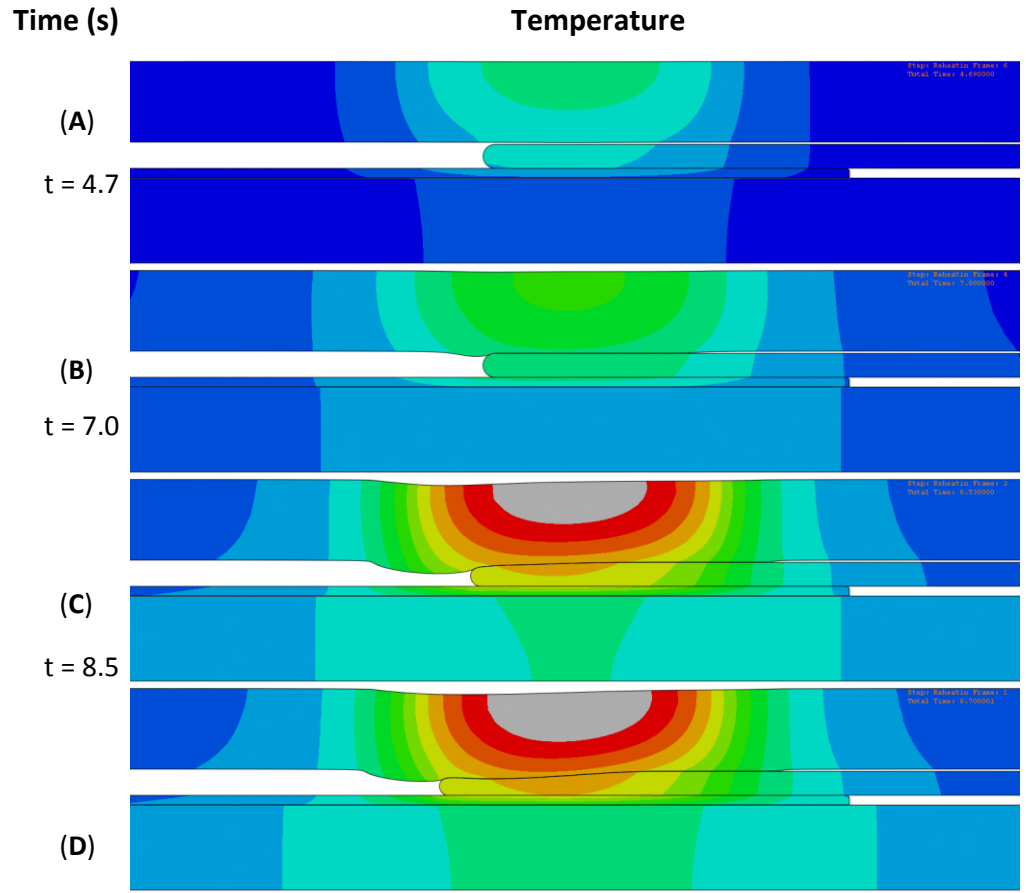
## 7.3 Results

### 7.3.1 Melt flow results

Figures 7.3, 7.4, 7.5 and 7.6 show the results of a melt flow model at specific time points. This model uses a frictional value of 0.05 and a heat-shrink modulus of 0.5 MPa and is presented here as an example of a melt flow simulation where the outer tube transitions between a solid below the melt point to a viscous solid with a low modulus above the melt temperature while being subjected to the pressure from the user defined heat-shrink material model. The time points were selected to show the evolution of flow during the laser welding process. The contour plot on the left, Figure 7.3 (A-D) and Figure 7.5 (A-D), shows the temperature and the contour plot on the right, Figure 7.4 (A-D) and Figure 7.6 (A-D), shows the logarithmic strain.

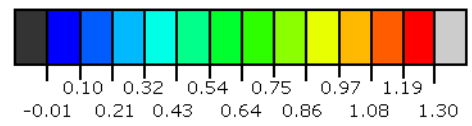
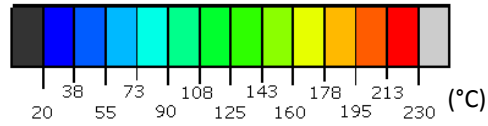
The first pair of images shows the assembly at a time of 4.7 s. At this stage the materials have begun heating but the heat-shrink has not contracted yet. At a time of 7.0 s, enough of the heat-shrink has been heated to a temperature above its crystalline melting point to allow it to contract and come into contact with the PEBAX<sup>®</sup>. At this time point - the PEBAX<sup>®</sup> is still below its melting point and hence there is minimal deformation. As the temperature in the

assembly rises, the PEBA<sup>X</sup>® begins to deform. By 8.7 s the PEBA<sup>X</sup>® has deformed significantly. The laser power is reduced at this point as illustrated in Figure 5.11 and so the temperature drops slightly and the PEBA<sup>X</sup>® deformation rate slows between 9 and 13 s. After 14 s the tip of the PEBA<sup>X</sup>® begins to soften and deform due to thermal conductivity through the PEBA<sup>X</sup>® layer with time. It is interesting to observe at this point that the heat-shrink tubing comes into contact with the balloon (lower PEBA<sup>X</sup>® layer) in front of the deforming outer tube and forms a barrier which prevents the type of rapid deformation / melt flow that occurred at 8.5 s. As the laser moves to the left the temperature of the PEBA<sup>X</sup>® tip increases allowing further melt flow and from 16 s until the finish at 21.4 s the melt flow increases steadily.



t = 8.7 Figure 7.3 (A-D) Temperature in assembly during first 8.7 s of welding.

Figure 7.4 (A-D) Logarithmic strain in assembly during first 8.7 s of welding.



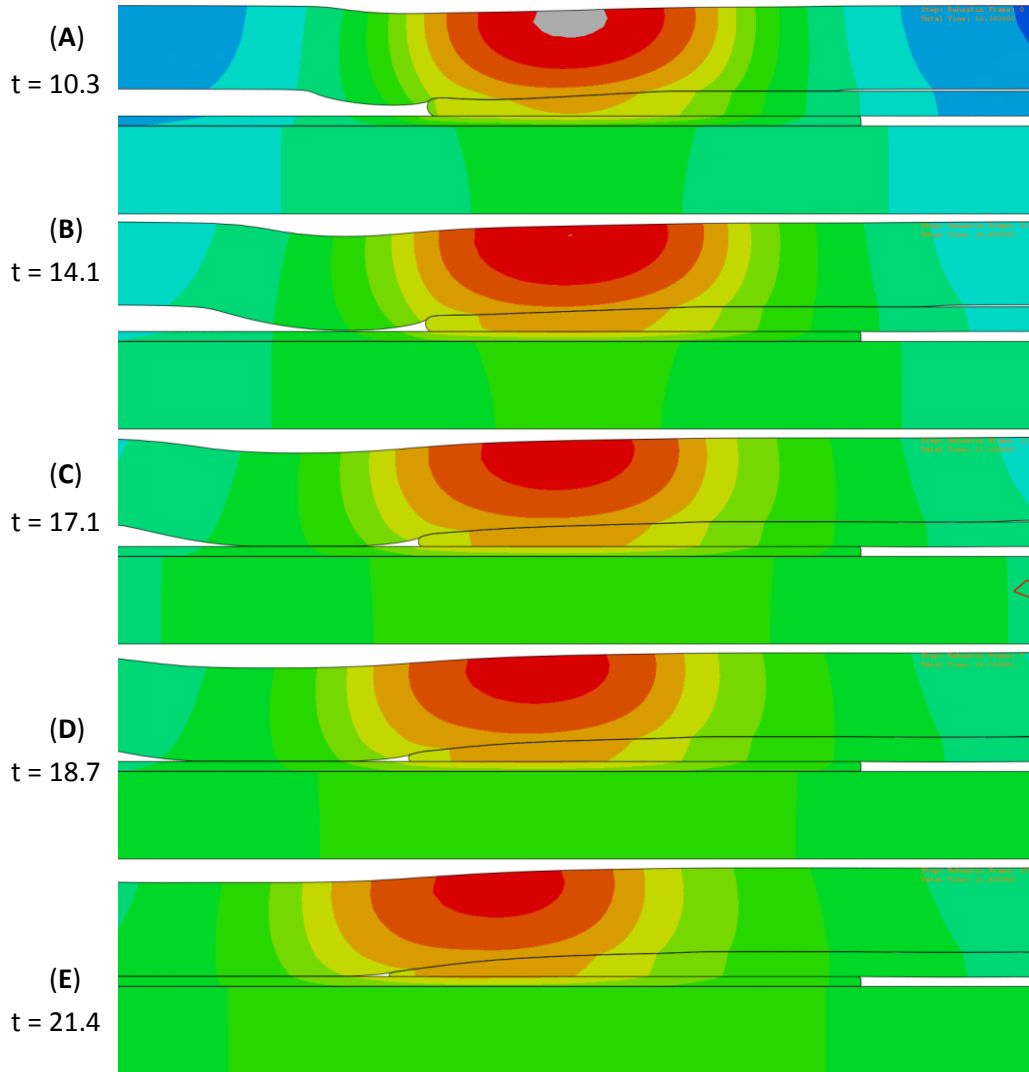


Figure 7.5 (A-E) Temperature in assembly during welding from 10 s until finish at 21.4 s, continued from figure 7.3.

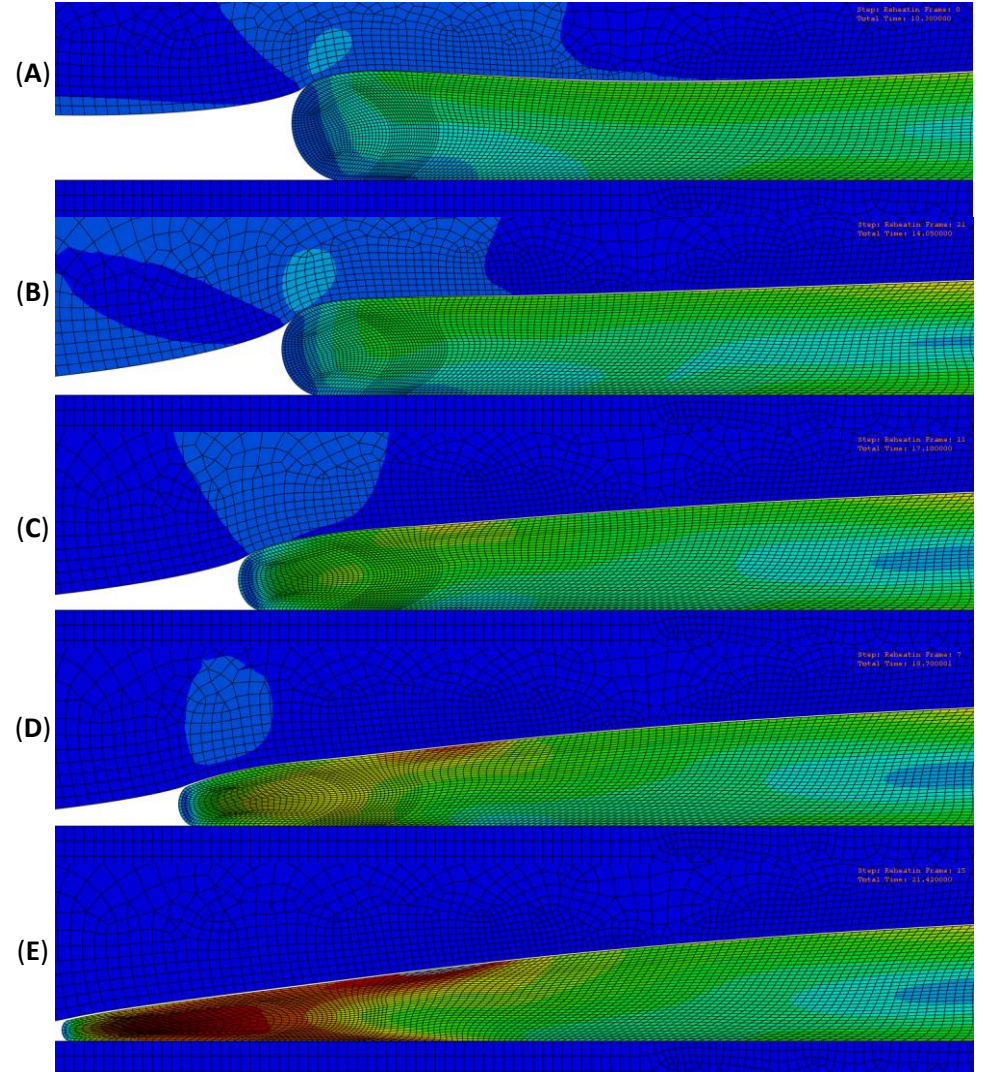
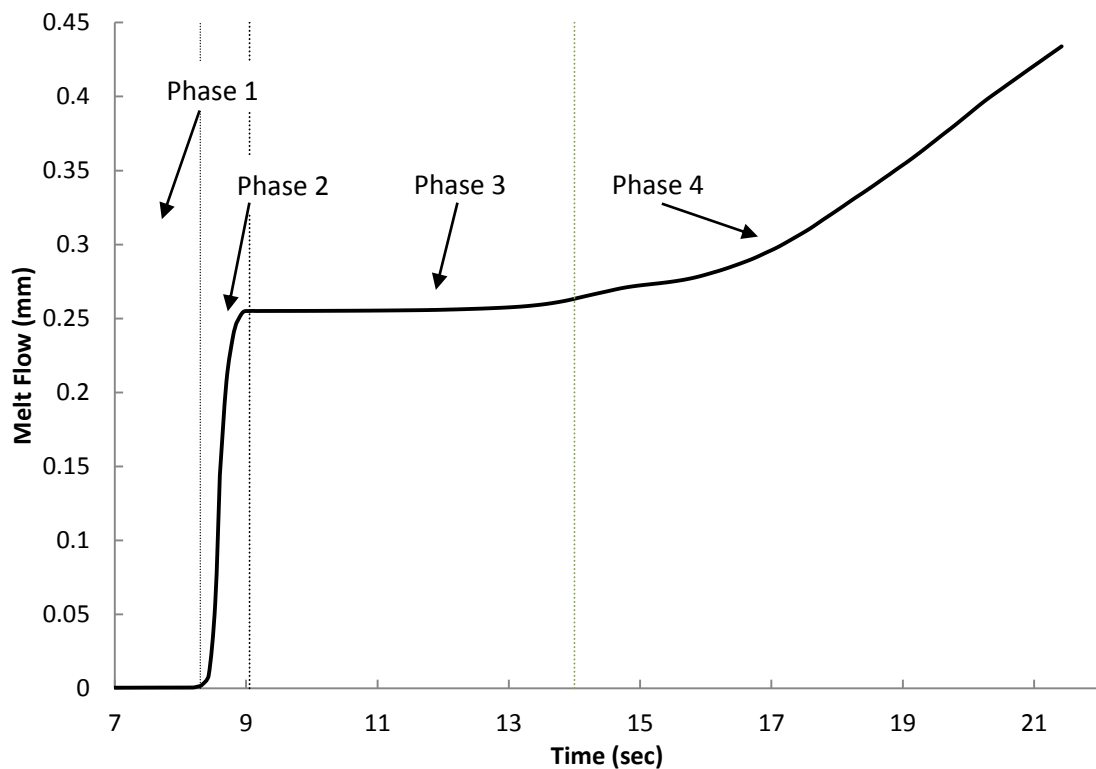


Figure 7.6 (A-E) Logarithmic strain in assembly during welding from 10 s until finish at 21.4 s, continued from figure 7.4.

The above deformation mechanisms are mapped in terms of melt flow against time in Figure 7.7 below.



**Figure 7.7** Melt flow of PEBAX® during laser bonding simulation as a function of time. A coefficient of friction of 0.05 was used and the heat-shrink modulus was 0.5 MPa. These results are from the same model as the results in Figures 7.4 - 7.7.

As illustrated in Figure 7.7, the melt flow process can be classified into four different phases of deformation as a function of time:

- Phase 1: No significant deformation / flow occurs, as the PEBAX® layer is below its melting point.
- Phase 2: PEBAX® flows rapidly, as the temperature induced by the laser causes the PEBAX® to melt.
- Phase 3: Little or no flow of the PEBAX® as the outer PEBAX® layer tip cools slightly and the heat-shrink deforms ahead of the tip causing an obstacle to the flow of the polymer melt pool.
- Phase 4: PEBAX® flows again as the PEBAX® tip melts.

In the example above the PEBAX® slides between the heat-shrink and the outer tube quite easily due to the low coefficient of friction (0.05). This results in a simulated melt flow length of 0.43 mm.

### 7.3.2 Effect of friction

In order to investigate the effect of friction on the melt flow, simulations were performed with various values of friction coefficients. The previous section showed how the PEBAX® slides between the heat-shrink and the outer PEBAX® layer when the friction is assumed to have a low value of 0.05. The example in Figure 7.8 below shows a melt flow simulation with the same setup but using a coefficient of friction of 0.2.

In this case the PEBAX® slips very little between the heat-shrink and the inner PEBAX® layer. The edges of the PEBAX® largely 'stick' to the heat-shrink and the outer tube, as the friction is at the higher level of 0.2. As the material gets hotter as a direct result of the laser absorption, the PEBAX® begins to demonstrate a boundary layer of flow as the polymer displaces and flows through the centre while the edges remain stationary. This type of flow results in a large amount of strain at the edges and relatively little in the centre as can be seen in the contour plot in Figure 7.8. While the high friction flow produces more strain than the low friction flow, it produces a considerably reduced overall melt flow length, despite the simulations failing before completion.

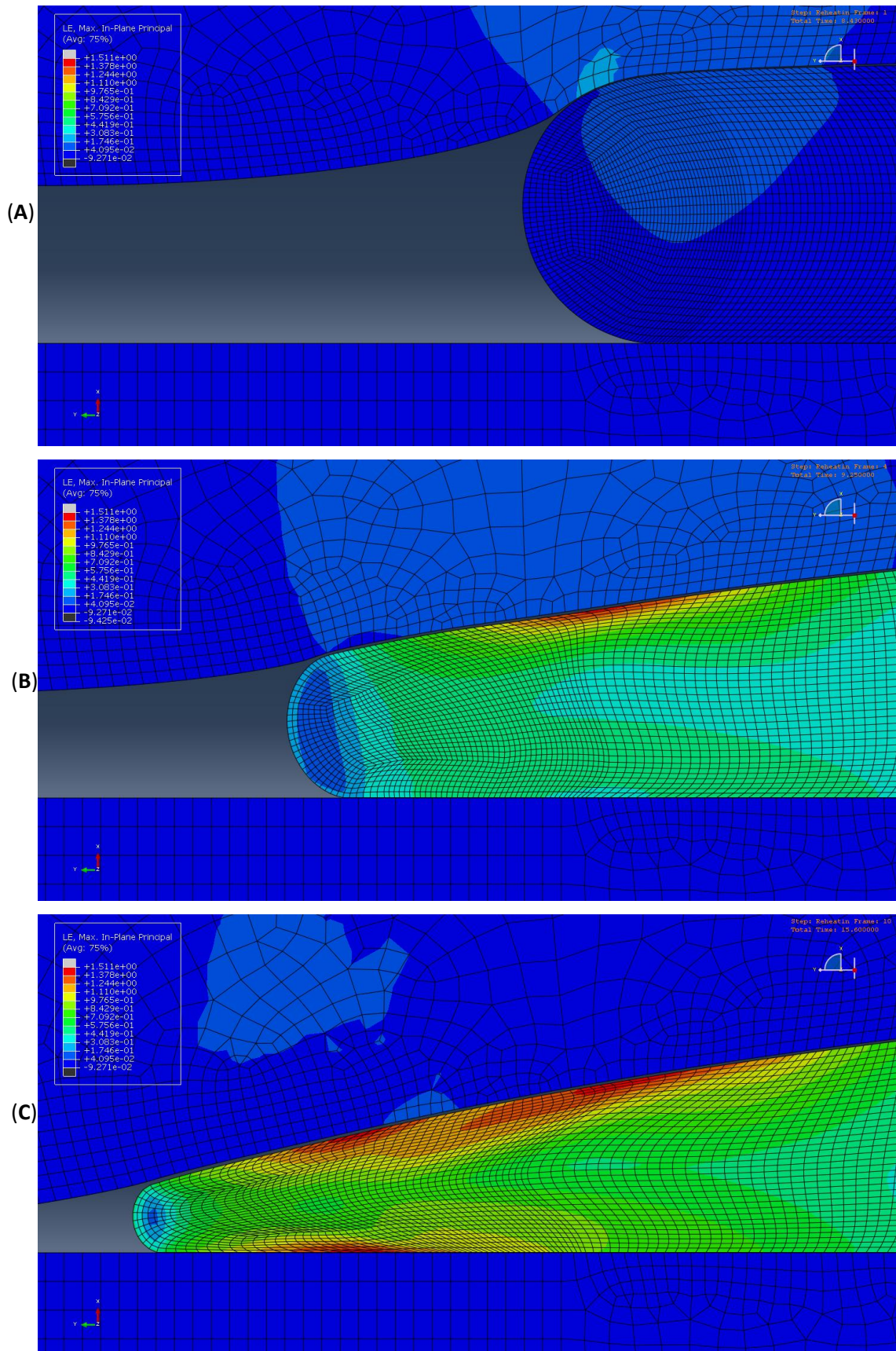
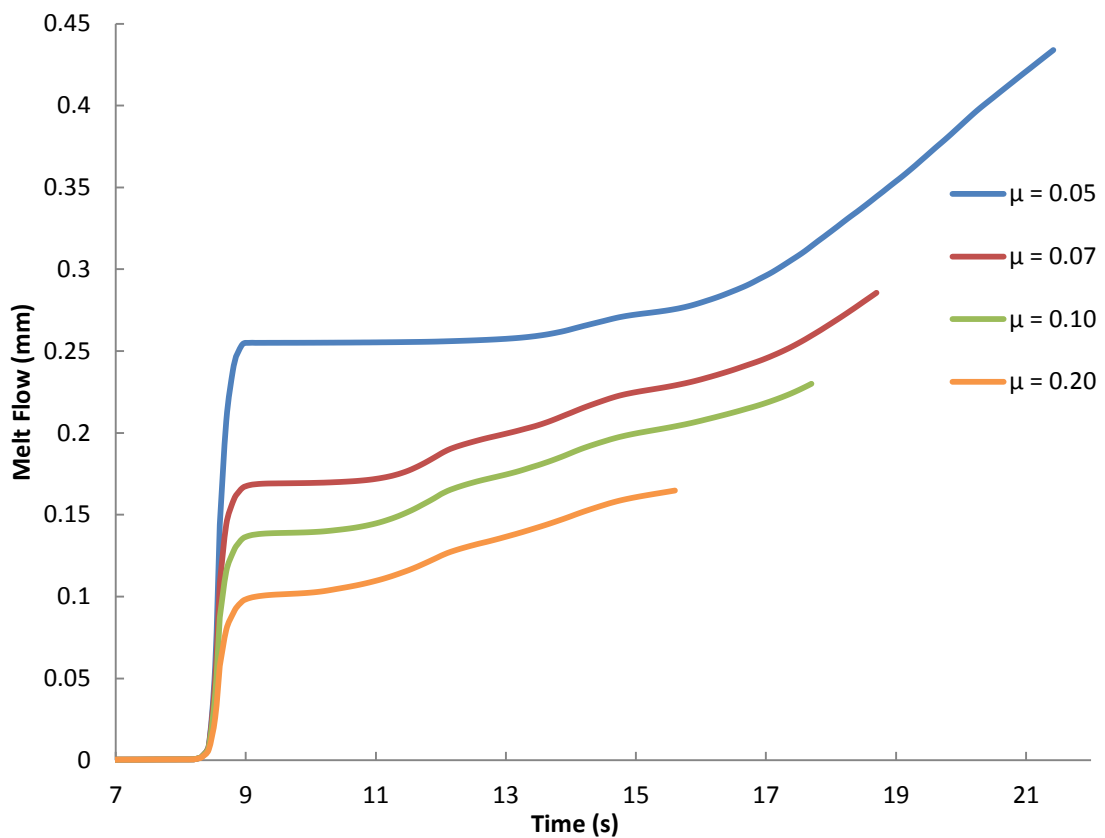


Figure 7.8(A-C) Contour plot of logarithmic strain in assembly during simulation with a friction coefficient of 0.2. Figure 7.8A is the strain at 8.4 s, Figure 7.8B is the strain at 9.25 s and figure 7.8C is the strain at 15.6 s at which point the simulation crashes due to excessive deformation.

Figure 7.9 below shows the effect of friction on melt flow for 4 different friction values ranging from 0.05 to 0.2.



**Figure 7.9 Melt flow of PEBA<sup>X</sup>® over time for four different coefficients of friction (0.05, 0.07, 0.1 and 0.2). The simulation ran to the end point of 21.4 s when the coefficient of friction was 0.05 but it failed due to excessive deformation for the other three values of coefficient of friction.**

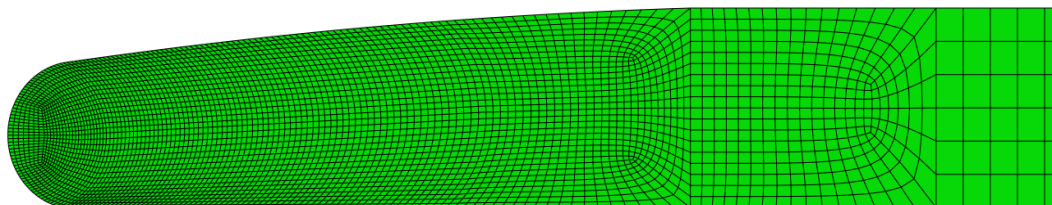
It can be seen from examining Figure 7.9 above, that the initial heating phase (Phase 1) is largely unaffected by the friction value as the temperature is too low for the PEBA<sup>X</sup>® to flow or deform significantly under the heat-shrink pressure. The rapid deformation of the second phase causes much more melt flow in the cases with lower friction. The extent of melt flow depends heavily on the level of friction, highlighting the importance of friction in the melt flow simulations. The duration of the third phase, which consists of little or no flow due to the PEBA<sup>X</sup>® tip cooling as it get further from the heat source, also varies significantly with friction. With a friction of 0.05 the third phase lasts approximately 5 seconds and with a friction of 0.2 the third phase lasts approximately 1.5 seconds. This occurs because with a friction value of 0.05, the PEBA<sup>X</sup>® tip cools more as it moves further from the heat source than with a friction of 0.2.

It is also noted from Figure 7.9 that the simulation predictions above give data until different time points. The data for the frictional values of 0.2, 0.1 and 0.07 represent simulation results after 15.6, 17.7 and 18.7 seconds respectively. The only simulation to run to the end time-point of 21.4 seconds was the one with the lowest coefficient of friction ( $\mu = 0.05$ ). The other three simulations failed to complete due to the excessive deformation and strain caused by the shear between the interface of the heat-shrink and the PEBA<sup>X</sup><sup>®</sup>. This was determined to occur when the logarithmic strain approached 1.5.

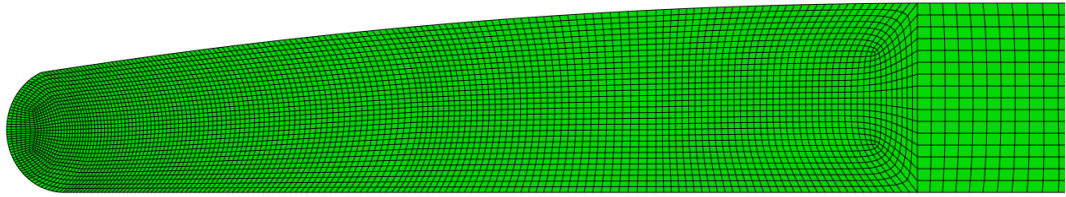
### 7.3.3 Effect of initial geometry

As there was considerable deformation and melt flow experienced, and as the material model utilised a solid modelling approach to simulate the deformation of the PEBA<sup>X</sup><sup>®</sup> as it transitioned between a solid at temperatures below 172°C and a viscous liquid above this temperature, considerable difficulties were experienced in completing the simulations over the 21 second laser welding process.

To investigate if it was possible to run the simulations to the end without solution convergence issues, the starting geometry was assumed to include some initial deformation. The purpose of this initial deformation was to reduce the high localised strain levels in the model. The figures below show the two deformed initial geometries examined. Figure 7.10(a) represents an initially deformed geometry that represents melt flow of 0.05 mm from its initial axial position and Figure 7.10(b) represents an initially deformed geometry that represents melt flow of 0.1 mm. Both initial geometries assumed an in initial residual stress state of zero.



(a)



(b)

**Figure 7.10** Two geometries used to reduce strain levels in the model. Figure (a) shows an assumed initial deformation of 0.05 mm and (b) shows an assumed initial deformation of 0.1 mm.

Simulations were performed on these two geometries in the same way as described previously. The results are shown below in Figure 7.11 and Figure 7.12 for the two different geometries respectively.

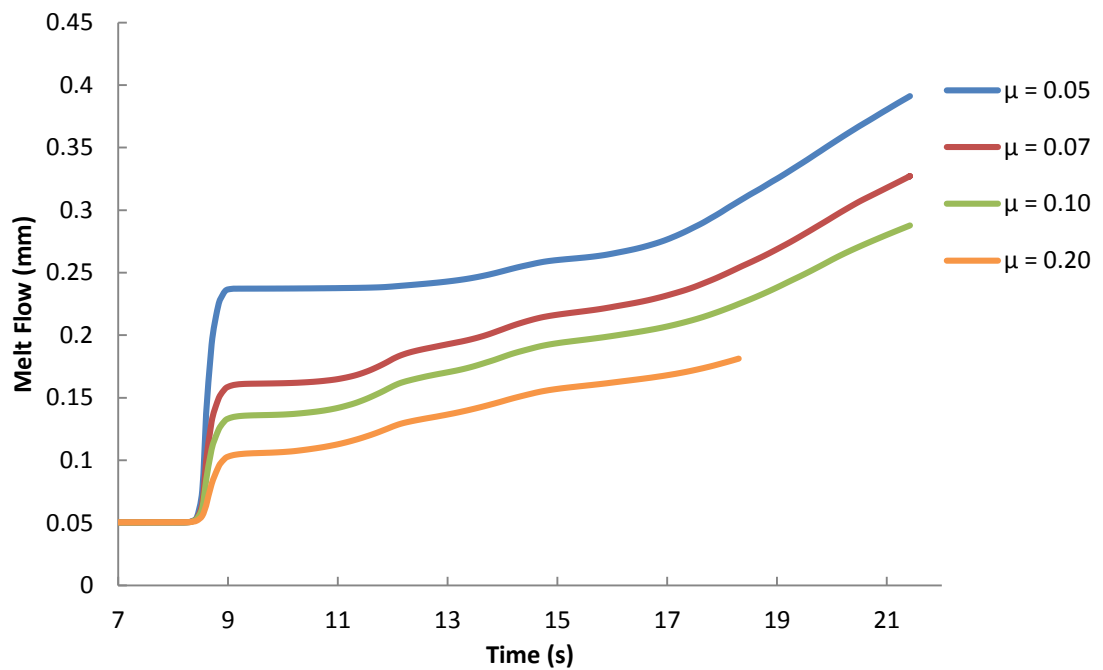


**Figure 7.11** Melt flow of PEBAx® over time for four different coefficients of friction using a geometry with an initial deformation of 0.05 mm.

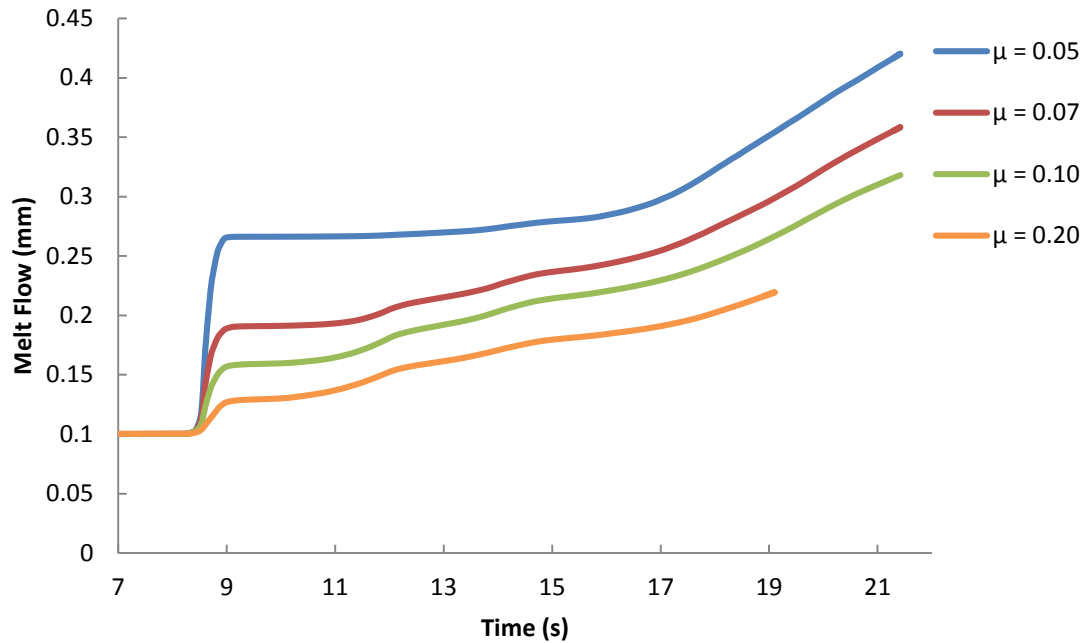


**Figure 7.12** Melt flow of PEBAx® over time for four different coefficients of friction using a geometry with an initial deformation of 0.10mm.

In both of the above cases the simulation ran to completion for the three lower coefficients of friction (0.05, 0.07 and 0.1) and experienced non-convergence issues associated with significant mesh deformation for the highest coefficients of friction (0.2). The trends are very similar in both graphs with the melt flow decreasing as the coefficient of friction increases.

The results below show how the assumption of including an initial stress-free geometry affects the melt flow. The first set of curves (red curves in Figure 7.13) with a friction of 0.05 run to completion. It can be seen that the initial deformation does not have a significant effect on melt flow length. With zero initial deformation the melt flow is 0.43 mm, whereas assuming an initial stress free geometry representing 0.05 mm axial deformation predicts an overall melt flow of 0.39 mm. Similarly, the simulations that assume an initial stress free geometry representing 0.01 mm of axial deformation predict an overall melt flow of 0.42 mm.

This trend is repeated for the other coefficients of friction.

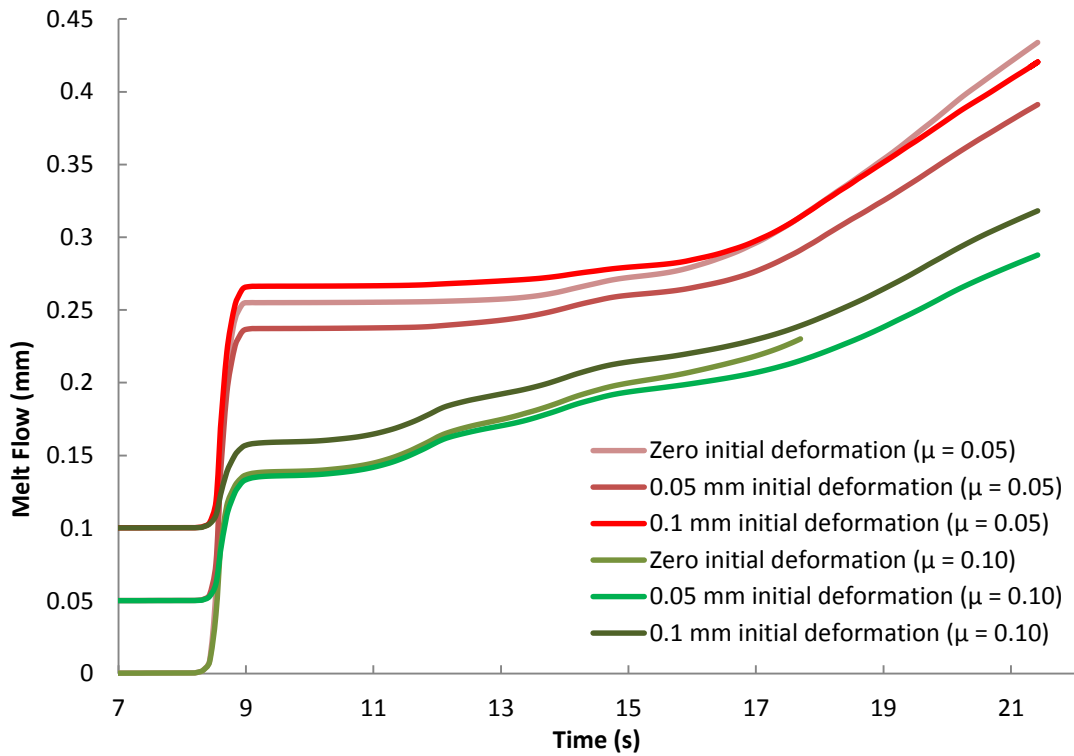


Figure 7.13 Melt flow of PEBAx® over time for three different geometries and two different coefficients of friction (0.05 and 0.10).

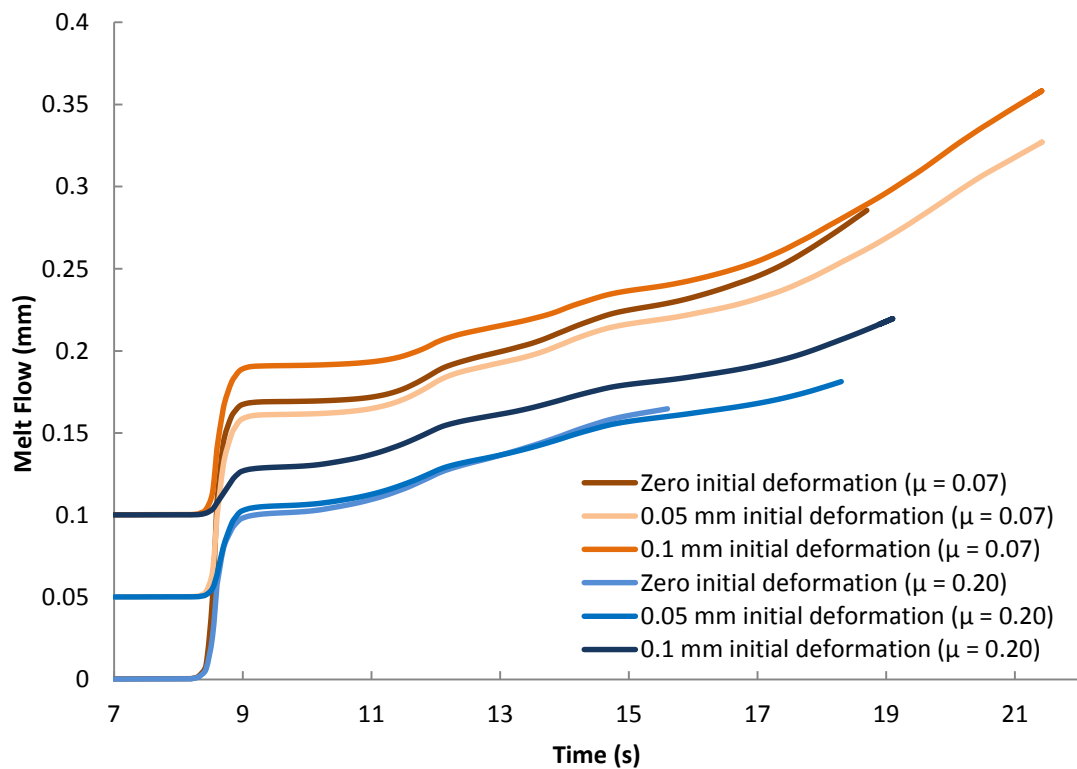


Figure 7.14 Melt flow of PEBAx® over time for three different geometries and two different coefficients of friction (0.07 and 0.20).

### 7.3.4 Effect of heat-shrink modulus

In investigating the effects of the heat-shrink modulus (and hence the level of stress imposed by the heat-shrink) on the amount of melt flow of the outer tube, it was determined that the heat-shrink with a higher modulus produced a larger shrink force, as would be expected. The effect of changing the modulus was investigated using 4 different heat-shrink modulus values. The melt flow length as a function of time, for the 4 different moduli, is shown below in Figure 7.15.

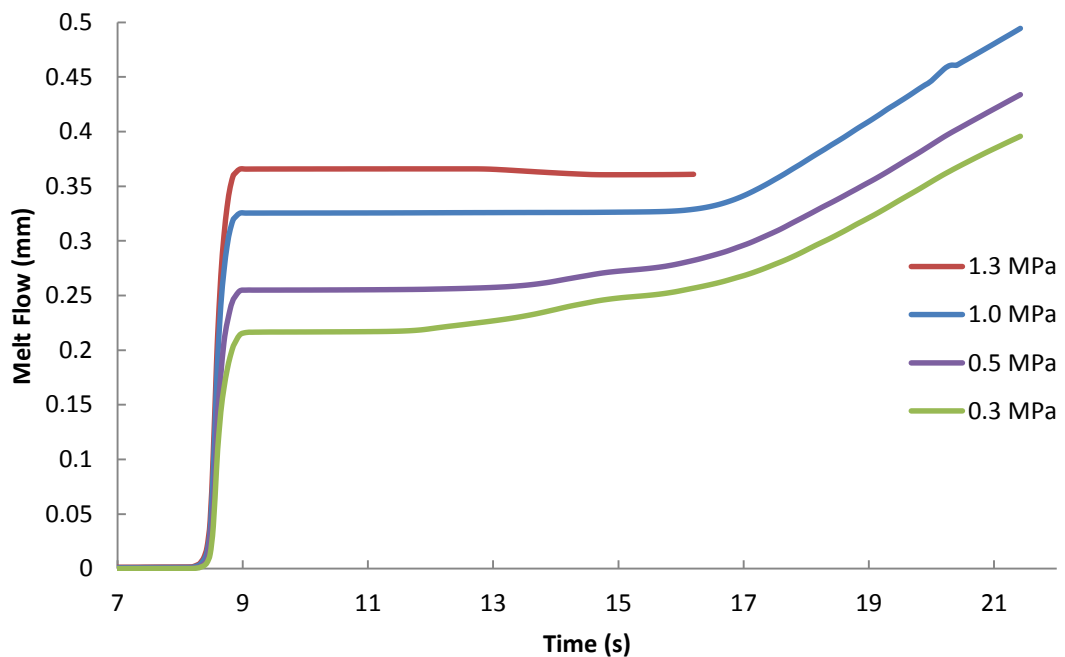


Figure 7.15 Melt flow of PEBA<sup>X</sup>® over time for four different heat-shrink moduli. These simulations used a coefficient of friction of 0.05 and a geometry with no initial deformation.

Three of these simulations ran to completion while the one with the largest heat-shrink modulus did not complete due to excessive mesh deformation. It is clear that the melt flow increases with increasing modulus but the increase is relatively small. A heat-shrink modulus of 0.3 MPa produces a melt flow of 0.39 mm while a heat-shrink modulus of 1.0 MPa produces a melt flow of 0.49 mm. Therefore a greater than threefold increase in modulus increases melt flow by approximately 25%.

## 7.4 Experimental results

In order to attempt to validate the predictions of the model, a number of Sterling™ 3 mm balloon catheters were welded and examined. Various heat-shrink tubing with different

moduli were used in these experimental tests to determine the validity of the computational model predictions. The melt flow was measured experimentally using optical coherence tomography (OCT) as described in section 3.2.3.

A total of 40 tests were performed, 10 each for 4 different heat-shrinks.

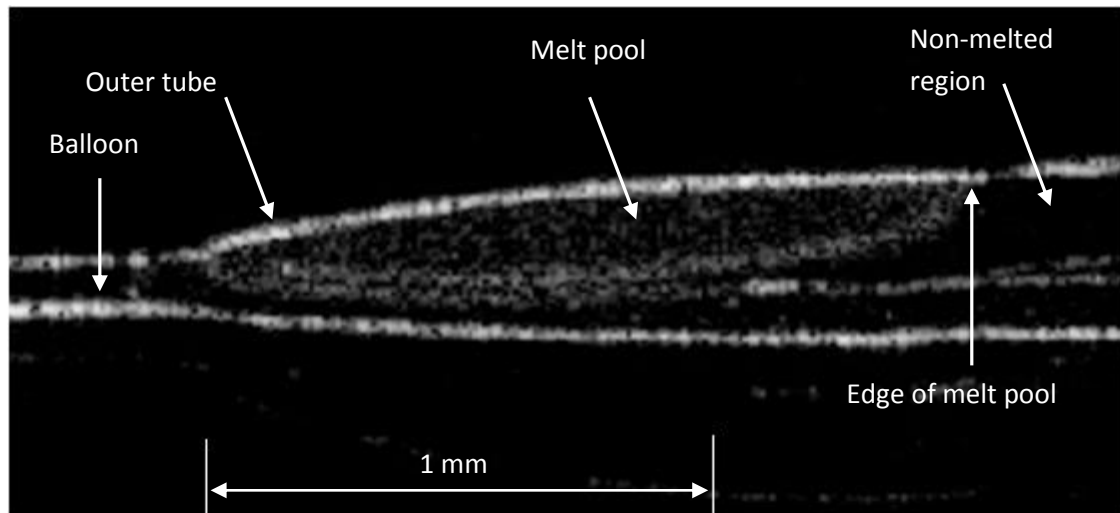
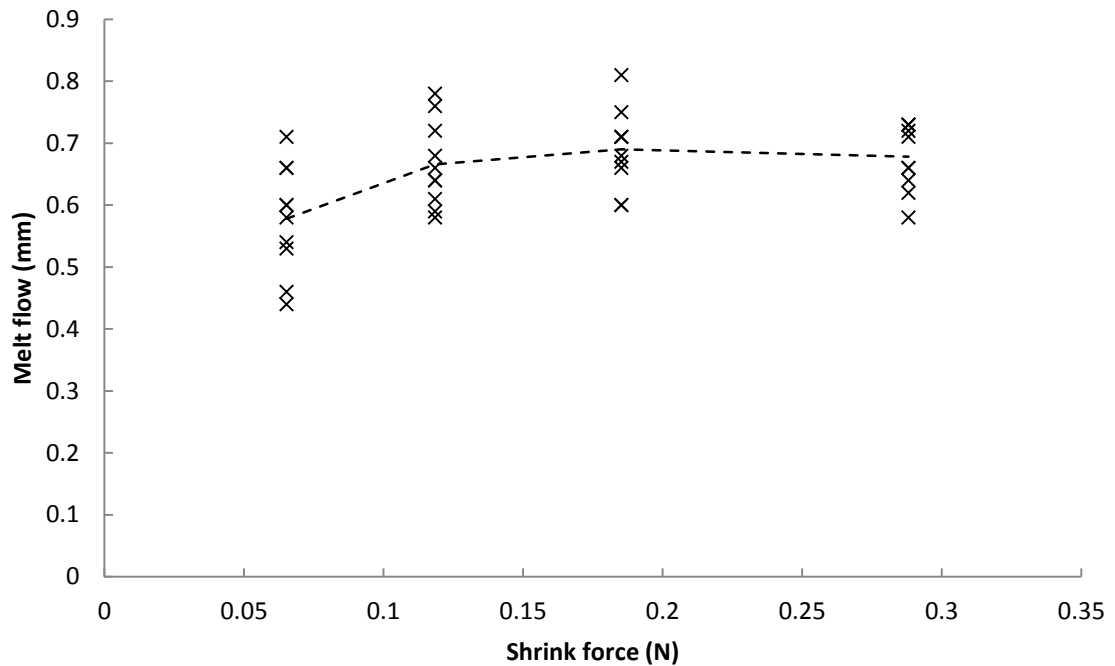


Figure 7.16 OCT images of a Sterling™ balloon catheter welded using heat-shrink with a shrink force of 0.12 N.

The table below gives a summary of the results of the experimental results. The melt flow length is defined as the distance from the tip of the PEBA<sup>X</sup>® after welding to its original position. The melt pool length is defined as the distance from the tip of the PEBA<sup>X</sup>® after welding to the proximal edge of the melt pool (right-hand edge highlighted in figure 7.16 above). The melt pool depth is included for information but the OCT data cannot measure this accurately due to refraction effects.



**Figure 7.17** Experimental measurements of melt flow of PEBAx® during welding for four different grades of heat-shrink tubing. The shrink force is the value measured in the hanger test described in section 3.5. A total of 10 experiments were performed for each of the 4 heat-shrink grades. The dashed line represents the average values.

Shrink force (N)	Melt flow Length (mm)	Melt Flow Std. Dev. (mm)	Melt Pool Length (mm)	Melt Pool Depth (mm)
0.065	0.58	0.09	1.48	0.14
0.118	0.67	0.07	1.69	0.15
0.185	0.69	0.06	1.69	0.14
0.288	0.68	0.05	1.75	0.15

**Table 7.2** Summary of experimental results.

The experimental results shown in Figure 7.17 indicate that the pressure applied by the heat-shrink tubing has a relatively small effect on the melt flow length. There is a 15 % increase in melt flow from the first heat-shrink sample to the second. This is approximately the same as the standard deviation from the experimental tests but after that there is only a small change which is much less than the standard deviation of the tests. The first change is marginally statistically significant but the subsequent changes are not.

As the shrink force increases the standard deviation of the melt flow length decreases. Also, as the shrink force increases, the melt pool length increases slightly more than the melt flow length, which indicates that the shrink force has a slightly larger effect on the temperature profile in the bond than on the melt flow length.

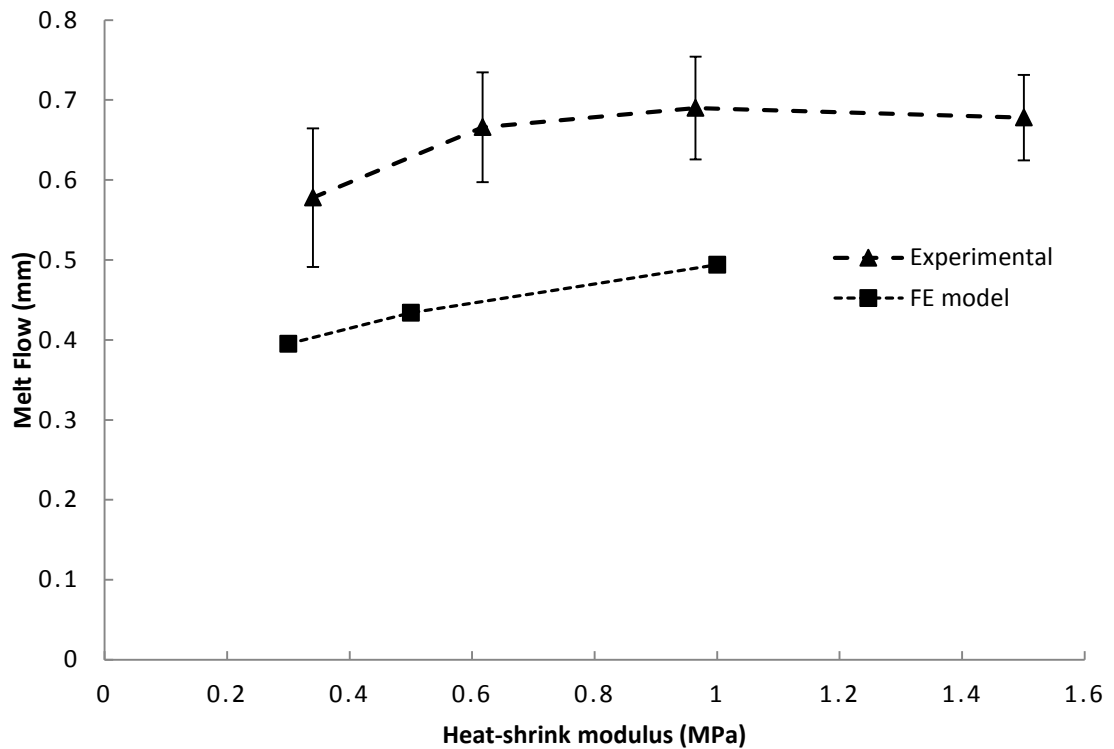


**Figure 7.18** Melt flow as a function of modulus as predicted by the model and measured by experiment. The error bars show the standard deviation of the experimental results.

In Figure 7.18, the melt flow predicted by the model is compared with the melt flow measured experimentally. The melt flow predicted by the model is approximately 30 % less than that measured experimentally. The model predicts that the melt flow length increases approximately linearly as the heat-shrink modulus increases, but the experimental data shows the melt flow increasing initially then levelling off. To further examine these trends the results in Figure 7.18 are normalized. The normalized results are plotted in Figure 7.19 and are rescaled and plotted again in Figure 7.20. The results are normalized by dividing all the melt flow length values by the melt flow of the first sample and similarly, the modulus is normalized by dividing the moduli values by the modulus of the first sample.

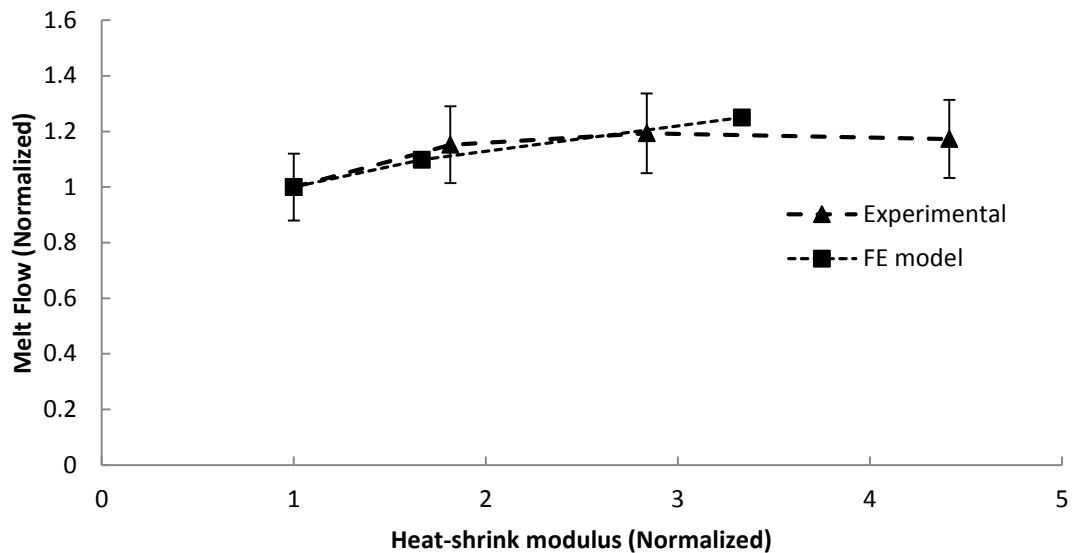


Figure 7.19 Normalized melt flow as a function of normalized modulus as predicted by the model and measured by experiment.

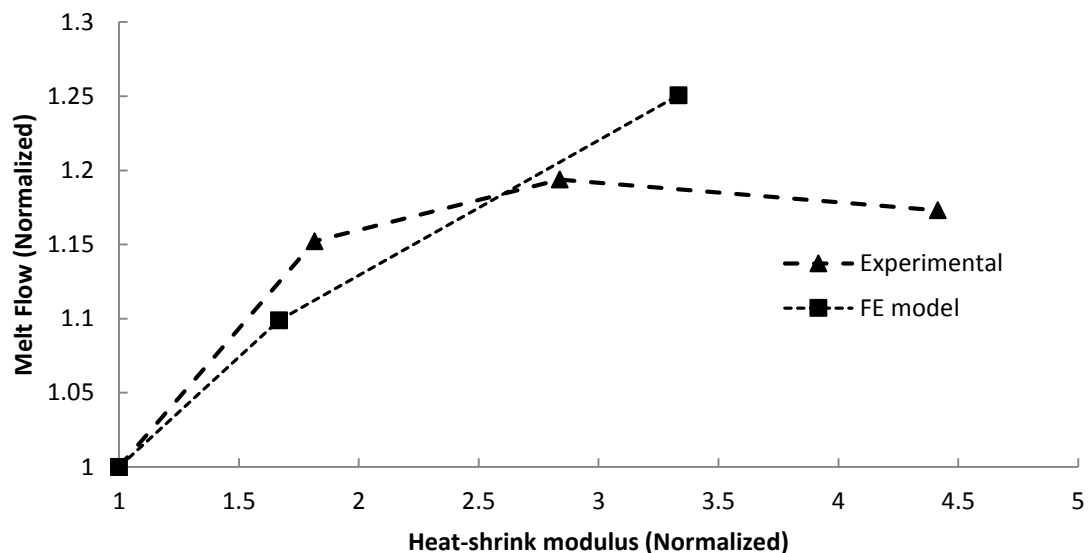


Figure 7.20 Normalized melt flow as a function of normalized modulus as predicted by the model and measured by experiment. Graph scaled to highlight trends.

In Figure 7.19 the normalized results show that there is quite a good agreement in the trends between the model and experiment, as both curves show a small increase in melt flow with heat-shrink modulus. The rescaled graph in Figure 7.20 highlights the differences in the trends between the model and the experimental results. The model predicts melt flow increasing approximately linearly as the modulus increases but the experimental results show an initial increase in melt flow followed by relatively little change in melt flow as the modulus is increased further.

The overall effect of the heat-shrink modulus on melt flow length is quite small for both model and experiment. The model predicts that increasing the modulus by a factor of 3.3 increases melt flow by a factor of 1.25 and the experiment data shows that increasing the modulus by a factor of 4.4 increases melt flow by a factor of 1.17.

## 7.5 Discussion

A finite element model of the laser bonding process of balloon catheters has been presented in this chapter. The purpose of this model is to predict the thermomechanical behaviour of the materials as they heat up and deform. The melt flow is the metric used to quantify the amount of deformation that occurs. This is used to compare simulations with experiments as well as to assess the effect of changing different parameters in the simulations.

The melt flow simulations all follow a similar pattern. A rapid increase in the melt flow length is observed as the material reaches its melting temperature followed by a period with little or no melt flow and then a final stage of steadily increasing melt flow as the tip of the outer tube melts.

The effect of starting the simulation with the outer tube in a pre-deformed state was also investigated. Starting with a pre-deformed geometry reduces mesh deformation and strain in the model making it more likely the simulation will run to completion. By assuming an initial stress free 'deformed' geometry, a very small effect on the predicted melt flow length was observed. This implies that the stresses built up during the initial deformation do not have a large impact on the melt flow length.

The effect of friction was determined to have an important role in predicting the melt flow length. Altering the value of friction not only alters the melt flow length but also the characteristics of the melt flow. With a low value of friction, the molten outer tube slides easily between the balloon and the heat-shrink and this causes an increase in the predicted melt flow length. Interestingly, for low coefficients of friction (0.05), the maximum strain occurring in the outer tube is lower than the maximum strain for higher coefficients of friction (0.2). With a high value of friction, the molten tube cannot slide between the balloon and the heat-shrink and therefore the melt flow is significantly lower than in the low friction case. Also as the surfaces of the outer polymer tube 'stick' to the heat-shrink and the balloon, the material begins to flow through the centre of the outer tube representing boundary layer

flow. This causes a large amount of strain concentrated near the surfaces of the outer tube (Figure 7.8C) even when the melt flow length is relatively small.

The effect of pressure (as imposed by the heat-shrink tubing) on the melt flow was also investigated in this chapter. This was investigated by altering the value of the heat-shrink modulus. As expected, it was found that the melt flow increased as the modulus of the heat-shrink increased but not by a large amount. This is probably due to the fact that once the heat-shrink diameter reduces in front of the outer tubing, it forms a barrier, restricting the melt flow. Therefore, increases in the modulus of the heat-shrink not only results in increases in the pressure pushing the PEBAX<sup>®</sup> forward but also in an axial pressure holding it back. This would explain why, in Figure 7.15, there is a significant difference in the melt flow for the different heat-shrink moduli during Phase 2 (the rapid deformation phase and before the heat-shrink has come down in front of the deforming PEBAX<sup>®</sup> tip) but very little difference in melt flow for Phases 3 and 4 (after the heat-shrink comes down in front of the deforming PEBAX<sup>®</sup>). At the end of Phase 2 (approximately 9.1 s) the simulated melt flow lengths for the three heat-shrink moduli (0.3 MPa, 0.5 MPa and 1.0 MPa) are 0.21 mm, 0.25 mm and 0.33 mm respectively. The melt flow during Phase 2 with a heat-shrink modulus of 1.0 MPa is 50 % larger than the melt flow with a heat-shrink modulus of 0.3 MPa. However, for Phases 3 and 4 the three simulations predict a further melt flow of approximately 0.18 mm independent of the heat-shrink modulus.

Simulation results are in broad agreement with experimental measurements of melt flow length in both trends and in quantitative predictions. However, the computational simulations underestimate the melt flow length by approximately 30 %. There are a number of factors which could explain this.

The higher thermal conductivity used in these simulations could affect the melt flow. The higher conductivity was introduced to reduce the temperature gradient occurring across the outer tube as this was causing excessive shear. As the mechanical properties of the PEBAX<sup>®</sup> are very dependent on temperature, any change to the temperature profile could have a significant effect on the melt flow.

Also, the value of the coefficient of friction was determined to have a large influence on the simulated melt flow. In this work, the coefficients of friction varied from 0.05 to 0.20 and as can be seen from Figure 7.9, the melt flow length decreases significantly as the coefficient of friction is increased. As no experimental data for the coefficient of friction was available, a

value was chosen to produce a melt flow closest to that observed experimentally. The coefficient of friction used in the comparisons with experimental data (Figures 7.18, 7.19 and 7.20) was 0.05. A lower value would have resulted in more melt flow, but attempts at these simulations failed due to excessive mesh deformation.

The trend in the simulations is for the melt flow to increase slightly with increasing modulus but the trend in the experimental results is for a small increase then a levelling off. However, it should be emphasized that difference in trends is a relatively small difference on a relatively small trend.

## CHAPTER 8      **Concluding remarks**

The aim of this work was to create a model of the laser bonding process used by Boston Scientific in the manufacturing of balloon catheters so that greater understanding of the flow characteristics and hence quality of bonding of the balloon to the catheter could be achieved. The laser bonding process uses a laser to heat an assembly containing the catheter parts to be welded and a heat-shrink tubing. The heat-shrink tubing surrounds the catheter and applies pressure to the assembly when heated. The catheter is made of an elastomeric copolymer called PEBA<sup>X</sup>®. When the PEBA<sup>X</sup>® reaches its melting point it flows due to the pressure applied by the heat-shrink. This flow results in a bond with a tapered profile. The model developed provides a tool which can be used in future studies of the laser bonding process so that the quality of bonding can be understood.

Prior to engaging on this research, there were many aspects of the bonding process which were not well understood, including the thermo-mechanical behaviour of the heat-shrink tubing, the thermo-mechanical deformation that occurs during the process and which parameters have the largest effect on the bonding process. This thesis contributes understanding to these through a combination approach of experimental testing and computational modelling.

### **8.1 Conclusions**

A large amount of research has been published on characterizing and modelling shape memory polymers (SMPs). As shown in Chapter 2 there are many SMP models which are appropriate for implementation into a computational FE code. However, there is an absence of literature investigating SMP for industrial applications such as laser bonding processes and this was also highlighted in Chapter 2. The two models implemented in this work are the stored strain model of Liu *et al.* [64] and the multiple natural configurations model of Barot *et al.* [77].

The thermo-mechanical properties of large-size heat-shrink tubing were characterised using dynamic mechanical thermal analysis and the results are presented in Chapter 4. Various properties were quantified including the elastic modulus as a function of temperature,

viscosity, plasticity, anisotropy and shrink force. It was found that the stress-strain characteristics at high temperatures could be modelled with the Neo-Hookean hyperelastic model.

A pressure test was designed and developed to measure the shrink pressure of the small heat-shrink tubes as it transitions through its phase change temperature. This was a novel experiment which was simple to perform and produced repeatable results. The pressure test data was then used to determine the modulus of the small heat-shrink tubes, as their small size made testing in a tensile tester very difficult.

Modelling the PEBAX<sup>®</sup> above and below its melt temperature using a solid modelling approach proved difficult due to the very large difference in the stiffness between the solid and molten PEBAX<sup>®</sup>. However, a model was successfully created using a Prony series and the time-temperature superposition. This model was proved to be reasonably accurate over the relevant time and temperature ranges.

A thermal model was described in Chapter 5 which predicts the temperature throughout the assembly. The model was validated by comparing the predicted melt pool with experimental data. It was found that the model predicted the melt pool quite accurately. It was necessary to do this to determine the temperature profile as a basis for investigating the thermo-mechanical behaviour in Chapter 7.

The two SMP models implemented into UMATs within ABAQUS were used to model the shrink force experiments. The Barot *et al.* model of SMPs was able to accurately model the shrink force of the heat-shrink, including the effects of thermal expansion. Thermal expansion affects the force as a function of time curve but has a negligible effect on the final force value. The Liu *et al.* model was not suitable for the large strains present in the heat-shrink as it is deformed and recovers with imposed temperature.

The large thermal gradients across the PEBAX<sup>®</sup> caused a very large variation in stiffness. This proved very difficult to model as it resulted in large localized shear strains which caused convergence problems. The thermal conductivity of the PEBAX<sup>®</sup> was increased to reduce the thermal gradients.

To deal with the large strains, there are a number of methods available within Abaqus. These include remeshing, explicit analysis and coupled Eulerian Lagrangian analysis. The remeshing technique was attempted but was ineffective because the remeshing cannot move the nodes that are in contact. The explicit technique was also attempted but was unstable and also the

time-steps required were extremely small and this made the analysis very computationally expensive. The coupled Eulerian Lagrangian technique is designed for fluid-solid interactions and is often used for many large strain problems. However in this case the PEBAX® is modelled as a solid and so this technique is not suitable. These techniques could be potentially useful in future work if these limitations were overcome.

The large strains present in the thermo-mechanical model often caused convergence problems. To reduce the strain levels some of the simulations were started with the PEBAX® in a deformed state. It was found that this technique enabled the simulation to run for longer, and it did not significantly affect the final melt flow prediction. This novel approach worked reasonable well as a means of reducing strain levels and resulted in similar predictions of melt flow with time.

The melt flow predicted by the thermo-mechanical model described in Chapter 7 is reasonably accurate with the model predicting approximately 65% of the experimental melt flow length. The coefficient of friction was found to be a very important parameter in the melt flow model. The heat-shrink modulus did not have a large effect on the melt flow length. This is due to the fact that the heat-shrink tube restricts the flow of the PEBAX® after it contracts onto the assembly in front of the advancing melt pool. The experimental data generated confirmed that the heat-shrink modulus had a modest impact on the melt flow length, and this trend was accurately predicted by the computational model.

## **8.2 Limitations of this work**

The thermo-mechanical model of the laser bonding process has a number of limitations. Some of these limitations arise from assumptions, others from a lack of data and others from the limits of the approach taken. Some of the main limitations of this work are outlined below.

This model attempted to use a solid modelling approach to represent the PEBAX® as it melts and flows. The validity of this is an open question. In reality the molten PEBAX® is a viscous liquid but as the majority of the PEBAX® is solid for the majority of the time and as the melt flow rates and times are low, a solid model approach was taken.

The model used for the PEBA<sup>X</sup>® was calibrated but not validated. Also, the calibration only produced a reasonable degree of accuracy over a relatively small range of temperatures and frequencies (but the most important range for the welding process). Inaccuracies in the model predictions are possible due to these assumptions.

The coefficient of friction was found to have a large impact on the solution but no experimental data on it was available. It had a very significant effect on both the qualitative melt flow behaviour and the quantitative melt flow length and therefore the lack of experimental data is a major limitation of this work.

The thermal conductivity of the outer tube was increased above values quoted in the literature in order to reduce the thermal gradient across the tube which was causing excessive distortion. This altered the initial flow behaviour of the PEBA<sup>X</sup>® in the model to reduce the large amounts of shear which were occurring. The effect of this on the final melt flow length is not known.

The strain levels observed in the computational model are very high and this often causes convergence problems. This limited the number and range of the parameter studies that could be undertaken with this complex model.

There is no experimental data of how the PEBA<sup>X</sup>® flows during the process. The only data is the position of the edge of the melt pool after welding. The behaviour of the molten PEBA<sup>X</sup>® may be significantly different to that predicted by the model.

The heat-shrink model implemented here does not include viscoelasticity, plasticity or anisotropy, but these probably are considered to not have a significant effect on the melt flow of the PEBA<sup>X</sup>®.

### **8.3 Discussion**

The main objective of this work was to create a computational model of the catheter bonding process and this has been achieved. The full thermomechanical model of the bonding process is qualitatively accurate in that it predicts the shape of the bond after welding reasonably accurately. The quantitative accuracy was assessed by comparing the melt flow length predicted by the model with that measured experimentally. The model under predicts

the amount of melt flow by approximately 30% and possible reasons for this have been discussed.

In order to create the thermo-mechanical model of the bonding process it was necessary to model the thermo-mechanical behaviour of the heat-shrink tubing. Prior to this work the details of the heat-shrink behaviour were poorly understood. In this work the heat-shrink has been extensively characterised and a model which accurately predicts its behaviour has been implemented into a computational FE code. This is a significant achievement and shows that SMPs can be accurately modelled and implemented into an FE model of a complicated industrial process.

The model of the bonding process provided a number of insights into the process which were not obvious. These insights include, a higher coefficient of friction results in less melt flow but produces higher strain values, the heat-shrink modulus has little impact on the melt flow and that the coefficient of friction has a large effect on the amount of melt flow.

This work will be very useful to Boston Scientific in the future because it will help them develop a better understanding of the bonding process. The effect of changing process parameters can be modelled and this should reduce the amount of trial and error experiments which are time-consuming and expensive. It is hoped that the better understanding of the process can help to reduce the number of defects that occur in the bonding process.

There are a number of aspects about this work which are novel. The heat-shrink tubing has been tested extensively and characterised in more detail than previously available. The pressure test developed to measure the shrink force of the small heat-shrink tube was also novel. The use of a SMP model in real-world FE application is quite novel.

Overall this work provides a significant amount of new knowledge about the laser bonding process and it provides a good foundation for further study.

## **8.4 Future work**

There is a lot of future work which could be done to make this model more useful and to increase understanding of the bonding process. From a modelling point of view more parameter studies could be performed investigating the effect of different parameters such

as temperature, time and geometry on the solution. The accuracy of the heat-shrink model could be further improved by including effects such as viscosity, plasticity and anisotropy.

The laser interaction with assembly could be integrated into the FE model along with the PID control algorithm. This would allow for easily changing the geometry and would make the model much more adaptable and useful.

The PEBA<sup>®</sup> model could be validated. This could involve modelling a number of rheometry tests and comparing the results with experimental data.

From an experimental point of view the coefficient of friction should be quantified, including how it changes with temperature. An experimental study which stopped the welding process at various time points could determine if the melt flow as a function of time predicted by the model is realistic.

The bond modelled in this work was axisymmetric but some catheter bonds are not. The methods used here could be applied to those bonds, although this would be computationally expensive. This would be helpful because the melt flow which occurs in those non-axisymmetric bonds is more complicated and less understood than the melt flow in the axisymmetric bonds.

## References

1. Brown David E., (2008) "Thomas Fogarty." in 'Inventing Modern America: From the Microwave to the Mouse.' The MIT Press.
2. Kilger E: 'Intensive care after minimally invasive and conventional coronary surgery: a prospective comparison', *Intensive care medicine*, **27**, pp 534-539, (2001).
3. [World Health Statistics 2009]. (2009). Retrieved from <http://www.who.int/whosis/whostat/2009/en/index.html>
4. [Coronary Heart Disease]. (n.d.). Retrieved from <http://www.uchospitals.edu/online-library/content=P00207>
5. Dotter C, Judkins M). 'Transluminal treatment of arteriosclerotic obstruction. Description of a new technique and a preliminary report of its applications' **30** (5): 654–70 (1964).
6. [Cardiac & Heart Surgeries]. (n.d). Retrieved from [http://www.medelines.asia/treatment/97/Coronary\\_Angioplasty\\_PTCA\\_.html](http://www.medelines.asia/treatment/97/Coronary_Angioplasty_PTCA_.html)
7. *Cardiac catheters – Global Trends, Estimates and Forecasts, 2012-2018*, Research and Markets, June 2014.
8. [Dilatation Catheter / Balloon]. (n.d.). Retrieved from <http://www.medicalexpo.com/prod/boston-scientific/product-74672-588291.html>
9. Behl M., Lendlein A., 'Shape memory polymers', *Materials Today* **10** 20-28 (2007).
10. Wornyo E. 'Fabrication and Characterization of Shape Memory Polymers at small-scales'
11. Silvers H. J. Jr, Wachtell S.: 'Perforating, welding and cutting plastics film with a continuous CO<sub>2</sub> laser', PA State University. Eng, Proc, pp 88-97, August 1970.
12. Wise R. J: 'Thermal welding of polymers', Woodhead Publishing Ltd., Cambridge, Oct 1999.
13. Russek U. A.: 'Innovative Trends in Laser Beam Welding of Thermoplastics'. Proc of 2 Int conf on Lasers in Manufacturing 105-111 June 2003.
14. Toyota Jidosha, K. K.: 'Laser beam welding of plastic plates' Patent application JP85213304 26 Sept 1985.
15. Kagan U. A., Bray R. G., Kuhn W.P., 'Laser Transmission welding of semicrystalline thermoplastics. Part I Optical characterization of nylon-based plastics', 58<sup>th</sup> Annual Technical Conference of the Society of Plastics Engineers. May 2000, pp 1171-1181.

16. Kagan U. A., Pinho G. P.: 'Laser transmission welding of semi-crystalline thermoplastics. Part II Analysis of mechanical performance of Welded nylon'. 58<sup>th</sup> Annual Technical Conference of the Society of Plastics Engineers. May 2000 pp.1182-1190.
17. Coelho J. P., Abreu M. A., Pires M. C., 'High Speed laser welding of films', *Opt Laser Eng.* **34**, 385-395 (2000).
18. Mayboudi L. S., Birk A. M., Zak G, 'A 2D thermal model for laser transmission welding of thermoplastics'. Laser material processing conference, ICALEO 2005.
19. Mackland A. P., Crafer R. C., 'Thermal modelling of laser welding and related processes: A literature review". *Opt laser tech* **37**, 99-115 (2005).
20. Mayboudi L. S., Birk A. M., Zak G., 'Laser Transmission Welding of a Lap-joint: Thermal Imaging Observations and Three-Dimensional Finite Element Modelling' *Jour of Heat Transfer* **127**, 1177-1186 (2007).
21. Frick T., 2007. 'Computation of temperature fields for laser transmission welding of plastics'. Proceedings of ICALEO 2007 Congress, Orlando, USA, pp. 596-601.
22. Casalino G., Ghorbel E., 'Numerical model of CO<sub>2</sub> laser welding of thermoplastic polymers', *J of Mat. proc. tech.* **207** 63-71 (2008).
23. Van de Ven J. D., Erdman A.G., 'Laser Transmission welding of thermoplastics – Part I: Temperature and Pressure modelling'. *J Manuf. Sci. Eng.* **127** 849-858 (2007).
24. Becker, F., Potente H., 'A step towards understanding the heating phase of laser transmission welding in polymers'. *Polym. Eng. Sci.* **42** (2) (2002).
25. Potente H., Korte J., Becker F, 'Laser transmission welding of thermoplastics analysis of heating phase'. *J Reinf. Plast. Compos.* **18** (10), 914-20 (1999).
26. Ilie, M., Cicola, E., Grevey, D., Mattei, S., Stoica, V, 'Diode laser welding of ABS: Experiments and process modeling' *Opt and Laser Tech* **41**, 608-614 (2004).
27. Coelho, J., Abren M. A., Rodrigues F. C., 'Methodologies for determining thermoplastic films optical parameters at 10.6µm laser wavelength', *Polymer Testing* **23**, 307-312 (2004).
28. Geiger M., Frick T., Schmidt M, 'Optical properties of plastics and their role for the modelling of the laser transmission welding process'. *German Academic Society for Production Engineering* **3** 49-55 (2008).
29. Incropera, F. P. and DeWitt, D. P. 1996, 'Introduction to Heat Transfer', 3<sup>rd</sup> ed., Wiley, New York.

30. Coelho João M.P., Abreu M.A., Rodrigues F.C., 'Thermal modelling CO laser radiation transmission welding of superposed thermoplastic films', *Opt. Eng.* **42** (11), 3365-3373 (2003)
31. Van de Ven J., 2006, 'Laser Transmission Welding of thermoplastics', Thesis, University of Minnesota, Twin Cities, Minneapolis, MN.
32. Potente H., Becker F., Fiegler G., and Korte J., 'Investigations towards applications of a New Technique on Laser Transmission Welding', *Weld World*, **45** (5), pp. 2-7 (2001)
33. Potente H., Wilke L., Ridder H., Mohnken R., Shabon A., 'Simulation of the Residual Stresses in the contour Laser Welding of Thermoplastics', *Polym, Eng, Sci.*, **48** 767-773 (2008)
34. Potente H., Fiegler G., 'An Approach to Model the Melt Displacement and Temperature Profiles During the Laser Through-Transmission Welding of Thermoplastics', *Polym. Eng. Sci.* **46** 1565-1575 (2006)
35. Yakacki C. M., Shandas R., Lanning C., Rech B., Eckstein A., Gall K., 'Unconstrained recovery characterization of shape-memory polymer networks for cardiovascular applications', *Biomaterials*, **28** 2255-2263 (2007)
36. Mather P. T., Luo X., Rousseau I. A., 'Shape memory polymer reasearch', *Annu. Rev. Mater. Res.* **39** 445-471 (2009)
37. Behl M., Razzaq M. Y., Lendlein A., 'Multifunctional Shape-Memory Polymers', *Adv. Mater.* **22**, 3388-3410 (2010)
38. Serrano M. C., Ameer G. A., 'Recent insights into the biomedical applications of shape-memory polymers', *Macromol. Biosci.* **12**, 1156-1171 (2012)
39. Beloshenko V. A., Varyukhin V. N, Voznyak Yu. V., 'The shape memort effect in polymers', *Russian chemical reviews*, **74**(3), 265-283 (2005)
40. Wei, Z. G., Sandstrom R., Miyazaki S., 'Shape-memory materials and hybrid composites for smart systems: Part 1 Shape-memory materials', *Journal of Material ScienceScience*, **33**, 3743-3762 (1998)
41. Lendlein A., Kelch S., 'Shape-memory polymers', *Angew. Chem. Int. Ed.* **41**, 2034-2057 (2002)
42. Xue L., Dai S., Li Z., 'Biodegradable shape-memory block co-polymers for fast self-expandable stents', *Biomaterials*, **31** (32), 8132-8140 (2010)
43. Reese S., Böl M., Christ D., 'Finite element-based multi-phase modelling of shape memory polymer stents', *Comput. Methods Appl. Mech. Engrg.*, **199**, 1276-1286 (2010)

44. Lendlein A., Langer R., 'Biodegradable, elastic shape-memory polymers for potential biomedical applications', *Science*, **296**, 1673-1676 (2002)
45. Ward Small, I. V., Singhal, P., Wilson, T. S., & Maitland, D. J. Biomedical applications of thermally activated shape memory polymers. *Journal of materials chemistry*, **20**(17), 3356-3366 (2010)
46. Sokolowski W, Metcalfe A, Hayashi S, Yahia L, Raymond J., 'Medical applications of shape memory polymers,' *Biomed. Mater*, 2:S23–27, (2007)
47. Sokolowski WM, Tan SC, 'Advanced self-deployable structures for space applications', *J. Spacecr. Rockets*, **44**, 750–54 (2007)
48. Mondal S., Hu J.L., 'Temperature stimulating shape memory polyurethane for smart clothing', *Indian J. Fibre Textile Res.*, **31** 66 (2006)
49. Hussein, H., Harrison, D., 'Investigation into the use of engineering polymers as actuators to produce "automatic disassembly" of electronic products', T. Bhamra, *Design and manufacture for sustainable development 2004*, Wiley-VCH, Weinheim (2004)
50. Yoo H.J., Jung Y.V., Sahoo N.G., Cho J.W., 'Polyurethane-Carbon nanotube nanocomposites prepared by In-Situ polymerization with electroactive shape memory', *J. Macromol. Sci. Phys.*, **45**, 441 (2006)
51. Maitland, D. J., Metzger, M. F., Schumann, D., Lee, A. and Wilson, T. S., 'Photothermal properties of shape memory polymer micro-actuators for treating stroke' *Lasers Surg. Med.*, 30: 1–11 (2002)
52. Meng H., Li G., 'A review of stimuli-responsive shape memory polymer composites', *Polymer*, **54** (9), 2199-2221 (2013)
53. Rousseau I. A., 'Challenges of shape memory polymers: A review of progress toward overcoming SMP's limitations', *Polymer Engineering and Science*, **48** 2075-2089 (2008)
54. Meng H., Li G., 'A review of stimuli-responsive shape memory polymer composites', *Polymer*, **54** (9), 2199-2221 (2013)
55. Liu C., Qin H., Mather P.T., 'Review of progress in shape-memory polymers', *J. Mater. Chem.*, **17** 1543-1558 (2007).
56. Liang, C., C. A. Rogers, and E. Malafeew. "Preliminary investigation of shape memory polymers and their hybrid composites." *Smart structures and materials* 97-105. (1991)

57. Hayashi, S. "Technical Report on Shape Memory Polymers." *Nagoya Research and Development Center, Mitsubishi Heavy Industry, Inc* (1990)
58. Tobushi H., Hashimoto T., Ito T., Hayashi S., Yamada E.,. 'Thermomechanical properties in a thin film of shape memory polymer of polyurethane series.' *J. Intell. Mater. Syst. Struct.*, **9**, 127-36 (1996)
59. Gall, K., Dunn, M. L., Liu, Y., Stefanic, G., & Balzar, D. 'Internal stress storage in shape memory polymer nanocomposites.' *Applied Physics Letters*, **85**(2), 290-292 (2004)
60. Beblo, R., & Weiland, L. M., 'Strain induced anisotropic properties of shape memory polymer.' *Smart Materials and Structures*, **17**(5), 055021. (2008)
61. Diani, J., Frédy, C., Gilormini, P., Merckel, Y., Régnier, G., & Rousseau, I. (2011). 'A torsion test for the study of the large deformation recovery of shape memory polymers.' *Polymer Testing*, **30**(3), 335-341.
62. Ratna, D., & Karger-Kocsis, J., 'Recent advances in shape memory polymers and composites: a review'. *Journal of Materials Science*, **43**(1), 254-269. (2008)
63. Chen, X., & Nguyen, T. D., 'Influence of thermo-viscoelastic properties and loading conditions on the recovery performance of shape memory polymers.' *Mechanics of Materials*, **43**(3), 127-138 (2011)
64. Liu Y., Gall K., Dunn M.L., Greenberg A.R., Diani J., 'Thermomechanics of shape memory polymers: Uniaxial experiments and constitutive modelling'. *Int. J. Plast.* **22** 279-313 (2006).
65. Gall, K., Yakacki, C. M., Liu, Y., Shandas, R., Willett, N., & Anseth, K. S. (2005). Thermomechanics of the shape memory effect in polymers for biomedical applications. *Journal of Biomedical Materials Research Part A*, **73**(3), 339-348.
66. Chung, T., Romo-Uribe, A., & Mather, P. T. (2008). Two-way reversible shape memory in a semi-crystalline network. *Macromolecules*, **41**(1), 184-192.
67. Nguyen, T. D. (2013). Modeling shape-memory behaviour of polymers. *Polymer Reviews*, **53**(1), 130-152.
68. Wornyo E., Gall K., Yang F., King W., 'Nanoindentation of shape memory polymer networks', *Polymer* **48**, 3213-3225 (2007)
69. Tobushi H., Hashimoto T., Hayashi S., Yamada E., 'Thermomechanical constitutive modelling in shape memory polymer of polyurethane'. *J. Intell. Mater. Syst. Struct.* **8** 711-718 (1997)
70. Tobushi H., Okumura K., Hayashi S., Ho N., 'Thermomechanical constitutive model of shape memory polymer', *Mech. Mat.* **33**, 545-554 (2001).

71. Morshedian J., Khonakdar H., Rasouli S., 'Modelling of Shape Memory Induction and Recovery in Heat-Shrinkable Polymers', *Macromol. Theory Simul.* **14** 428-434 (2005).
72. Nguyen, T. D., Jerry Qi, H., Castro, F., & Long, K. N. (2008). 'A thermoviscoelastic model for amorphous shape memory polymers: incorporating structural and stress relaxation', *Journal of the Mechanics and Physics of Solids*, **56**(9), 2792-2814.
73. Ghosh, P., & Srinivasa, A. R. (2011). A two-network thermomechanical model of a shape memory polymer. *International Journal of Engineering Science*, **49**(9), 823-838.
74. Westbrook, K. K., Kao, P. H., Castro, F., Ding, Y., & Jerry Qi, H. (2011). 'A 3D finite deformation constitutive model for amorphous shape memory polymers: a multi-branch modelling approach for non-equilibrium relaxation processes.' *Mechanics of Materials*, **43**(12), 853-869.
75. Castro F., Westbrook K. K., Long K. N., Shandas R., & Qi H. J. (2010). Effects of thermal rates on the thermomechanical behaviours of amorphous shape memory polymers. *Mechanics of Time-Dependent Materials*, **14**(3), 219-241.
76. Chen Y., Lagoudas D., 'A constitutive theory for shape memory polymers. Part 1: Large deformations', *J. Mech. Phys. Solids*, **56** 1752-1765 (2008).
77. Barot G., Rao I.J., Rajagopal K.R., 'Constitutive modelling of the mechanics associated with crystallisable shape memory polymers', *Z.A.M.P.* **57** 652-681 (2006).
78. Rao I.J., Rajagopal K.R., 'A thermodynamic framework for the study of crystallization in polymers', *Z.A.M.P.* **53** 365-406 (2002).
79. Kafka V., 'Shape memory polymers: A mesoscale model of the internal mechanism leading to the S.M. phenomena', *Int. J. Plast.*, **24** 1533-1548 (2008)
80. Kafka V., (2001) 'Mesomechanical Constitutive Modelling', World Scientific, Singapore.
81. Qi H. J., Nguyen T. D., Castro F., Yakacki C. M., & Shandas R. (2008). Finite deformation thermo-mechanical behaviour of thermally induced shape memory polymers. *Journal of the Mechanics and Physics of Solids*, **56**(5), 1730-1751.
82. Crawford R.J., 1998, *Plastics Engineering*, 3rd edn, Elsevier Butterworth-Heinmann, Oxford, p 112.
83. Hsiao B. S., Zuo F., Mao Y., Schick C., (2013) *Handbook of polymer crystallization: Experimental Techniques*, John Wiley & Sons Inc, p. 2.

84. Charlesby A., Hancock N. H., 'The effect of cross-linking on the elastic modulus of polythene', *Proceedings of the Royal Society of London A: Mathematical, Physical and Engineering Sciences* **218** 245-255, (1953).
85. [Campus Database]. (n.d). Retrieved from <http://www.campusplastics.com/>
86. I-Kuan Yang, Ping-Hung Tsai, 'Rheology and structure change of poly(ether-block-amide) segmented block copolymer', *J. Cent. South Univ. Technol.* (2007).
87. Park S. W., and R. A. Schapery. "Methods of interconversion between linear viscoelastic material functions. Part I—A numerical method based on Prony series." *International Journal of Solids and Structures* 36.11 (1999): 1653-1675.
88. Crawford R.J., 1998, *Plastics Engineering*, 3rd edn, Elsevier Butterworth-Heinmann, Oxford, p 116.
89. [Dynamic mechanical analysis]. (n.d). Retrieved from <http://www.pebax.com/en/properties/mechanical-properties/dynamic-mechanical-analysis-dma/index.html>
90. [Snell's Law]. (2015). In Encyclopaedia Britannica. Retrieved from <http://www.britannica.com/EBchecked/topic/550450/Snells-law>
91. G. Woan, 2000, *The Cambridge Handbook of Physics Formulas*, Cambridge University Press, Cambridge, New York.
92. Bothe L., Rehage G., Autohesion of Elastomers. *Rubber Chemistry and Technology*: November 1982, Vol. **55**, No. 5, pp. 1308-1327.
93. Schauer T., 'Development of a Computational Laser Bond Process Model'. Boston Scientific Technical Report (confidential),(n.d.).
94. Schauer T., McGowan R., 'Source Term Determination for the Computational Laser Bond Process Model'. Boston Scientific Technical Report (confidential),(n.d.).
95. Holman J.P., *Heat transfer*, 9<sup>th</sup> ed. McGraw Hill, New York, 2002.
96. [Plastic Materials Selection Guide for Micro Machining and Micro Molding]. (2011). Retrieved from <http://www.mikrotech.com/micro-molding-materials/material-selection-guide.html>
97. [Pebax MED]. (n.d). Retrieved from <http://www.pebax.com/en/pebax-range/product-viewer/Pebax-MED/>
98. [Finite deformation of thick-walled cylinders under internal stress and linear perturbation from a state of finite deformation]. (2013). Retrieved from <http://caigroup.ucsd.edu/pdf/>

99. Mattson S, 'Laser welding RNF 100 (or MT-LWA) shrink tubing'. Boston Scientific Technical Report, Document number 30729-00, (confidential),(2001).